The Rockefeller University 1901

Direct Photon Differential Cross Section

in $\bar{p}p$ Collisions at $\sqrt{s} = 1.8$ TeV.

A thesis presented to the faculty of

The Rockefeller University

in partial fulfillment of the requirements for

the degree of Doctor of Philosophy

by

Arthur G. Maghakian

1996

UMI Number: 9711362

Copyright 1996 by
Maghakian, Arthur George

UMI
300 North Zeeb Road
Ann Arbor, MI 48103

Inclusive Photon Differential Cross Section

in $\bar{p}p$ Collisions at $\sqrt{s} = 1.8$ TeV.

by

Arthur G. Maghakian

Abstract

Data taken from the Collider Detector at Fermilab (CDF) during the 1992-1993 run are used to measure the cross section for production of isolated prompt photons in $\bar{p}p$ collisions at $\sqrt{s} = 1.8$ TeV. Prompt photon production in $\bar{p}p$ collisions is sensitive to the gluon structure function of the proton and therefore can provide a test of QCD. This measurement is a significant improvement over the 1989 measurement due to the addition of the Central Preradiator Chambers, the neural network hardware trigger upgrades, and the six times increase in integrated luminosity. Two different methods, *conversion method* and *profile method*, were used to separate prompt photons from photons produced by decay of hadrons. The profile method was used from 10-16 GeV P_T and the conversion method at $P_T > 16$ GeV. The cross section, measured as a function of transverse momentum, is in general agreement with next-to-leading order QCD predictions over five orders of magnitude but has a steeper slope at low P_T.

ii

Acknowledgements

I would like to use this opportunity to express my gratitude to my thesis advisor Professor Konstantin Goulianos, for his interest and support of my work during all these years, for many useful discussions of this analysis and comments on my thesis. I have been working on direct photon analysis with Steve Kuhlmann (Argonne National Laboratory) and I gratefully acknowledge his guidance and assistance. Additional thanks are due to Phil Melese for many valuable comments and suggestions on my thesis and Roger Rusack for suggesting this analysis topic. I thank people from QCD group of CDF collaboration, for their help, particularly Anwar Bhatti, Rob Harris, Bob Blair and Carol Hawk. This thesis would not have been possible without the efforts of entire CDF collaboration. I am very grateful to the Rockefeller University for all these years of graduate study devoted completely to the research and for the University's democratic atmosphere, not to mention the Manhattan Experience.

Finally, my special acknowledgment is for the love, support and encouragement of my family - my parents, wife and daughter.

CDF COLLABORATION

F. Abe,[13] M. Albrow,[7] D. Amidei,[16] C. Anway-Wiese,[4] G. Apollinari,[26]

H. Areti,[7] P. Auchincloss,[25] F. Azfar,[21] P. Azzi,[20] N. Bacchetta,[18]

W. Badgett,[16] M. W. Bailey,[24] J. Bao,[33] P. de Barbaro,[25] A. Barbaro-Galtieri,[14] V. E. Barnes,[24] B. A. Barnett,[12] P. Bartalini,[23] G. Bauer,[15]

T. Baumann,[9] F. Bedeschi,[23] S. Behrends,[2] S. Belforte,[23] G. Bellettini,[23]

J. Bellinger,[32] D. Benjamin,[31] J. Benlloch,[15] D. Benton,[21] A. Beretvas,[7]

J. P. Berge,[7] A. Bhatti,[26] K. Biery,[11] M. Binkley,[7] F. Bird,[28] D. Bisello,[20]

R. E. Blair,[1] C. Blocker,[28] A. Bodek,[25] V. Bolognesi,[23] D. Bortoletto,[24]

C. Boswell,[12] T. Boulos,[14] G. Brandenburg,[9] E. Buckley-Geer,[7] H. S. Budd,[25]

K. Burkett,[16] G. Busetto,[20] A. Byon-Wagner,[7] K. L. Byrum,[1] C. Campagnari,[7]

M. Campbell,[16] A. Caner,[7] W. Carithers,[14] D. Carlsmith,[32] A. Castro,[20]

Y. Cen,[21] F. Cervelli,[23] J. Chapman,[16] G. Chiarelli,[8] T. Chikamatsu,[30]

S. Cihangir,[7] A. G. Clark,[23] M. Cobal,[23] M. Contreras,[5] J. Cooper,[7]

M. Cordelli,[8] D. P. Coupal,[28] D. Crane,[7] J. D. Cunningham,[2] T. Daniels,[15]

F. DeJongh,[7] S. Dell'Agnello,[23] M. Dell'Orso,[23] L. Demortier,[26] B. Denby,[7]

M. Deninno,[3] P. F. Derwent,[16] T. Devlin,[27] M. Dickson,[25] S. Donati,[23]

J. P. Done,[29] R. B. Drucker,[14] A. Dunn,[16] K. Einsweiler,[14] J. E. Elias,[7]

R. Ely,[14] E. Engels, Jr.,[22] S. Eno,[5] D. Errede,[10] S. Errede,[10] A. Etchegoyen,[7a]

Q. Fan,[25] B. Farhat,[15] I. Fiori,[3] B. Flaugher,[7] G. W. Foster,[7] M. Franklin,[9]

M. Frautschi,[18] J. Freeman,[7] J. Friedman,[15] H. Frisch,[5] A. Fry,[28] T. A. Fuess,[28]

Y. Fukui,[13] S. Funaki,[30] A. F. Garfinkel,[24] S. Geer,[7] D. W. Gerdes,[16]

P. Giannetti,[23] N. Giokaris,[26] P. Giromini,[8] L. Gladney,[21] D. Glenzinski,[12]

M. Gold,[18] J. Gonzalez,[21] A. Gordon,[9] A. T. Goshaw,[6] K. Goulianos,[26]

iv

H. Grassmann,[28] A. Grewal,[21] G. Grieco,[23] L. Groer,[27] C. Grosso-Pilcher,[5]

C. Haber,[14] S. R. Hahn,[7] R. Hamilton,[9] R. Handler,[32] R. M. Hans,[33]

K. Hara,[30] B. Harral,[21] R. M. Harris,[7] S. A. Hauger,[6] J. Hauser,[4] C. Hawk,[27]

J. Heinrich,[21] D. Hennessy,[6] R. Hollebeek,[21] L. Holloway,[10] A. Hölscher,[11]

S. Hong,[16] G. Houk,[21] P. Hu,[22] B. T. Huffman,[22] R. Hughes,[25] P. Hurst,[9]

J. Huston,[17] J. Huth,[7] J. Hylen,[7] M. Incagli,[23] J. Incandela,[7] H. Iso,[30]

H. Jensen,[7] C. P. Jessop,[9] U. Joshi,[7] R. W. Kadel,[14] E. Kajfasz,[7] T. Kamon,[29]

T. Kaneko,[30] D. A. Kardelis,[10] H. Kasha,[33] Y. Kato,[19] L. Keeble,[29]

R. D. Kennedy,[27] R. Kephart,[7] P. Kesten,[14] D. Kestenbaum,[9] R. M. Keup,[10]

H. Keutelian,[7] F. Keyvan,[4] D. H. Kim,[7] S. B. Kim,[16] S. H. Kim,[30]

Y. K. Kim,[14] L. Kirsch,[2] P. Koehn,[25] K. Kondo,[30] J. Konigsberg,[9] S. Kopp,[5]

K. Kordas,[11] W. Koska,[7] E. Kovacs,[7a] M. Krasberg,[16] S. E. Kuhlmann,[1]

E. Kuns,[27] A. T. Laasanen,[24] S. Lammel,[4] J. I. Lamoureux,[32] T. LeCompte,[10]

S. Leone,[23] J. D. Lewis,[7] P. Limon,[7] M. Lindgren,[4] T. M. Liss,[10] N. Lockyer,[21]

O. Long,[21] M. Loreti,[20] E. H. Low,[21] D. Lucchesi,[23] C. B. Luchini,[10]

P. Lukens,[7] P. Maas,[32] K. Maeshima,[7] A. Maghakian,[26] M. Mangano,[23]

J. Mansour,[17] M. Mariotti,[23] J. P. Marriner,[7] A. Martin,[10] J. A. J. Matthews,[18]

R. Mattingly,[2] P. McIntyre,[29] P. Melese,[26] A. Menzione,[23] E. Meschi,[23]

S. Mikamo,[13] M. Miller,[5] T. Mimashi,[30] S. Miscetti,[8] M. Mishina,[13]

H. Mitsushio,[30] S. Miyashita,[30] Y. Morita,[13] S. Moulding,[26] J. Mueller,[27]

A. Mukherjee,[7] T. Muller,[4] L. F. Nakae,[28] I. Nakano,[30] C. Nelson,[7]

D. Neuberger,[4] C. Newman-Holmes,[7] L. Nodulman,[1] S. Ogawa,[30] K. E. Ohl,[33]

R. Oishi,[30] T. Okusawa,[19] C. Pagliarone,[23] R. Paoletti,[23] V. Papadimitriou,[7]

S. Park,[7] J. Patrick,[7] G. Pauletta,[23] L. Pescara,[20] M. D. Peters,[14]

T. J. Phillips,[6] G. Piacentino,[3] M. Pillai,[25] R. Plunkett,[7] L. Pondrom,[32]

v

N. Produit,[14] J. Proudfoot,[1] F. Ptohos,[9] G. Punzi,[23] K. Ragan,[11] F. Rimondi,[3]

L. Ristori,[23] M. Roach-Bellino,[31] W. J. Robertson,[6] T. Rodrigo,[7] J. Romano,[5]

L. Rosenson,[15] W. K. Sakumoto,[25] D. Saltzberg,[5] A. Sansoni,[8] V. Scarpine,[29]

A. Schindler,[14] P. Schlabach,[9] E. E. Schmidt,[7] M. P. Schmidt,[33] O. Schneider,[14]

G. F. Sciacca,[23] A. Scribano,[23] S. Segler,[7] S. Seidel,[18] Y. Seiya,[30]

G. Sganos,[11] M. Shapiro,[14] N. M. Shaw,[24] Q. Shen,[24] P. F. Shepard,[22]

M. Shimojima,[30] M. Shochet,[5] J. Siegrist,[28] A. Sill,[7a] P. Sinervo,[11] P. Singh,[22]

J. Skarha,[12] K. Sliwa,[31] D. A. Smith,[23] F. D. Snider,[12] L. Song,[7] T. Song,[16]

J. Spalding,[7] P. Sphicas,[15] A. Spies,[12] L. Stanco,[20] J. Steele,[32] A. Stefanini,[23]

J. Strait,[7] G. Sullivan,[5] K. Sumorok,[15] R. L. Swartz, Jr.,[10] T. Takahashi,[19]

K. Takikawa,[30] F. Tartarelli,[23] Y. Teramoto,[19] S. Tether,[15] D. Theriot,[7]

J. Thomas,[28] R. Thun,[16] M. Timko,[31] P. Tipton,[25] A. Titov,[26] S. Tkaczyk,[7]

A. Tollestrup,[7] J. Tonnison,[24] J. Tseng,[12] M. Turcotte,[28] N. Turini,[3]

N. Uemura,[30] F. Ukegawa,[21] G. Unal,[21] S. Vejcik, III,[16] R. Vidal,[7]

M. Vondracek,[10] R. G. Wagner,[1] R. L. Wagner,[7] N. Wainer,[7] R. C. Walker,[25]

J. Wang,[5] Q. F. Wang,[26] A. Warburton,[11] G. Watts,[25] T. Watts,[27]

R. Webb,[29] C. Wendt,[32] H. Wenzel,[7a] W. C. Wester, III,[14] T. Westhusing,[10]

A. B. Wicklund,[1] E. Wicklund,[7] R. Wilkinson,[21] H. H. Williams,[21]

B. L. Winer,[25] J. Wolinski,[29] D. Y. Wu,[16] X. Wu,[23] J. Wyss,[20] A. Yagil,[7]

W. Yao,[14] K. Yasuoka,[30] Y. Ye,[11] G. P. Yeh,[7] M. Yin,[6] J. Yoh,[7] T. Yoshida,[19]

D. Yovanovitch,[7] I. Yu,[33] J. C. Yun,[7] A. Zanetti,[23] F. Zetti,[23] S. Zhang,[15]

W. Zhang,[21] G. C. Zucchelli,[23] and S. Zucchelli[3]

(CDF Collaboration)

[1] *Argonne National Laboratory, Argonne, Illinois 60439*

vi

(2) Brandeis University, Waltham, Massachusetts 02254

(3) Istituto Nazionale di Fisica Nucleare, University of Bologna, I-40126 Bologna, Italy

(4) University of California at Los Angeles, Los Angeles, California 90024

(5) University of Chicago, Chicago, Illinois 60637

(6) Duke University, Durham, North Carolina 27708

(7) Fermi National Accelerator Laboratory, Batavia, Illinois 60510

(8) Laboratori Nazionali di Frascati, Istituto Nazionale di Fisica Nucleare, I-00044 Frascati, Italy

(9) Harvard University, Cambridge, Massachusetts 02138

(10) University of Illinois, Urbana, Illinois 61801

(11) Institute of Particle Physics, McGill University, Montreal H3A 2T8, and University of Toronto,

Toronto M5S 1A7, Canada

(12) The Johns Hopkins University, Baltimore, Maryland 21218

(13) National Laboratory for High Energy Physics (KEK), Tsukuba, Ibaraki 305, Japan

(14) Lawrence Berkeley Laboratory, Berkeley, California 94720

(15) Massachusetts Institute of Technology, Cambridge, Massachusetts 02139

(16) University of Michigan, Ann Arbor, Michigan 48109

(17) Michigan State University, East Lansing, Michigan 48824

(18) University of New Mexico, Albuquerque, New Mexico 87131

(19) Osaka City University, Osaka 588, Japan

(20) Universita di Padova, Instituto Nazionale di Fisica Nucleare, Sezione di Padova, I-35131 Padova, Italy

(21) University of Pennsylvania, Philadelphia, Pennsylvania 19104

(22) University of Pittsburgh, Pittsburgh, Pennsylvania 15260

(23) Istituto Nazionale di Fisica Nucleare, University and Scuola Normale Superiore of Pisa, I-56100 Pisa, Italy

(24) Purdue University, West Lafayette, Indiana 47907

(25) University of Rochester, Rochester, New York 14627

vii

(26) *Rockefeller University, New York, New York 10021*

(27) *Rutgers University, Piscataway, New Jersey 08854*

(28) *Superconducting Super Collider Laboratory, Dallas, Texas 75237*

(29) *Texas A&M University, College Station, Texas 77843*

(30) *University of Tsukuba, Tsukuba, Ibaraki 305, Japan*

(31) *Tufts University, Medford, Massachusetts 02155*

(32) *University of Wisconsin, Madison, Wisconsin 53706*

(33) *Yale University, New Haven, Connecticut 06511*

(a) *Visitor*

viii

Contents

List of Figures

xi

List of Tables

Chapter 1

Introduction

In the framework of the Standard Model (SM), Quantum Chromodynamics (QCD) has been our most successful theoretical attempt to describe the physics of the strong interactions. QCD is a theory of interacting quarks and gluons, which are the basic constituents of hadrons. One of the key features of the theory is the property of asymptotic freedom [1] - the weakening of the effective quark-gluon coupling at short distances. This feature allows the application of well-developed perturbative techniques to the processes with large momentum transfer between quarks and gluons. However, the strong processes observed experimentally involve only hadrons, and the description of hadron-hadron interactions is rather complicated in terms of constituent quarks and gluons. The real challenge for QCD is to describe the quark-gluon dynamics within the hadron, which is not possible using perturbative techniques. In order to make meaningful comparisons between theory and experiment, we need a formalism which relates calculable quantities to measurable ones. For high energy processes, QCD provides this framework through *factorization theorems* [2]: physical cross sections are factorized into a "hard cross section" between elemen-

1

tary partons (i.e., quarks and gluons) and a "soft part" consisting of universal (i.e., process-independent) distribution functions of partons inside hadrons. The universal parton distribution functions play a central role in the Standard Model phenomenology. Many precise measurements and quantitative tests of the SM depend on our knowledge of the parton distribution functions of hadrons. In addition, these functions are very important tools in our attempt to unfold the underlying quark-gluon dynamics and hadron structure.

The parton distributions can, in principle, be determined from analyzing a set of experiments - deep inelastic scattering, lepton pair production, direct photon production, W- and Z-production, high P_T jet production, etc. One of these processes - direct photon production, is the subject of this thesis.

In contrast to photons produced by decay of hadrons, direct photons are produced in the primary collision. The importance of measuring the cross section of direct single photons at large P_T arises from the well understood electromagnetic coupling of a photon to a quark. In QCD, at lowest order, prompt photon production in $\bar{p}p$ collisions is dominated by the Compton process ($qg \rightarrow q\gamma$), which is sensitive to the gluon distribution function of the proton. This is the reason why direct photons can be used to probe the gluon distribution within the proton. An advantage of using direct photons is that their momentum vector can be easily reconstructed experimentally. However, the measurement of direct photoproduction is complicated by the large background of photons produced by decays of single isolated π^0 end η mesons. In this experiment, we have used two different methods to separate direct photons from background. In one method (*profile method*) we analyse the shape of the showers produced by photons in the electromagnetic calorimeter. In the second method (*conversion method*),we measure the conversion rate of photon candidates in

2

a layer of material. This rate is different for a single direct photon than for two or more photons produced in the decay of a neutral meson.

We have measured the direct isolated photon cross section using the data collected by the Collider Detector at Fermilab (CDF) during the 1992-93 run at the Tevatron collider. At the high proton-antiproton center of mass energies available at the Tevatron, we can measure the direct photon cross section in a wide P_T range and probe the parton distributions of the proton antiproton in the fractional momentum range $0.013 < x < 0.13$. The current measurement represents a significant improvement over the previous CDF measurement of the direct isolated photon cross section [4], which is due to the addition of the Central Preconverter chambers, trigger upgrades, new background separation method and six times increased integrated luminosity. The resulting small statistical and systematical uncertainties allow precise quantitative tests of QCD. An article reporting the results of this measurement has been published in Physical Review Letters [3].

In chapter 2, we begin with a brief overview of perturbative QCD and the factorization technique, which in leading order (LO) reduces to the naive parton model of the earlier years. Then, the theoretical framework for describing the production of direct photons in hadronic collisions is reviewed and various sources of theoretical uncertainties are discussed. Chapter 3 describes the components of the Collider Detector at Fermilab (CDF), which are relevant for this measurement, particularly the central electromagnetic calorimeter, the central electromagnetic strip chambers and the central preshower chambers. In chapter 4 we explain how the data were collected and which triggers were used. Then, we discuss the cuts used to select photon candidates, the efficiencies of these cuts and our estimate of the total acceptance for prompt photons. Chapter 5 explains how the single isolated π^0 background was re-

3

jected using the *profile* and *conversion* methods, and the advantages of each method. The direct isolated photon cross section is presented in chapter 6 and compared with the previous direct photon cross section measurement of CDF [4]. In chapter 7 we discuss the systematic uncertainties of the measurement. Reconstructed neutral meson peaks are used to make a precise measurement of the profile method's systematic error. Finally, in chapter 8 we give a detailed comparison between measured data and theoretical predictions. Although the measurement and theory are in general agreement, there is a distinct shape difference between them. In order to understand this discrepancy, some possible sources of disagreement are discussed.

4

Reproduced with permission of the copyright owner. Further reproduction prohibited without permission.

Chapter 2

Discussion of Theory

2.1 Naive Parton Model

We will start the description of hard scattering processes using the *naive parton model* [5] . The parton model is applicable, with varying degrees of success, to any hadronic cross section involving a large momentum transfer. The basic ideas of the parton model are the following. The colliding proton and antiproton are composed of many massless pointlike particles called *partons*. A $\bar{p}p$ collision in this model is a collision between a single parton in the proton and a single parton in the antiproton producing large transverse momentum particles. The remaining partons in the proton and antiproton, called *spectator* partons, *fragment* to less-energetic particles. This framework is illustrated schematically in Fig. 2.1.

The parton model assumes that one can factorize the process which involves large momentum transfer into two parts, a "hard" part corresponding to the colliding partons, and a "soft" part, which determines the probability densities for partons inside hadrons. The probability of obtaining a parton a in a hadron A with a momen-

5
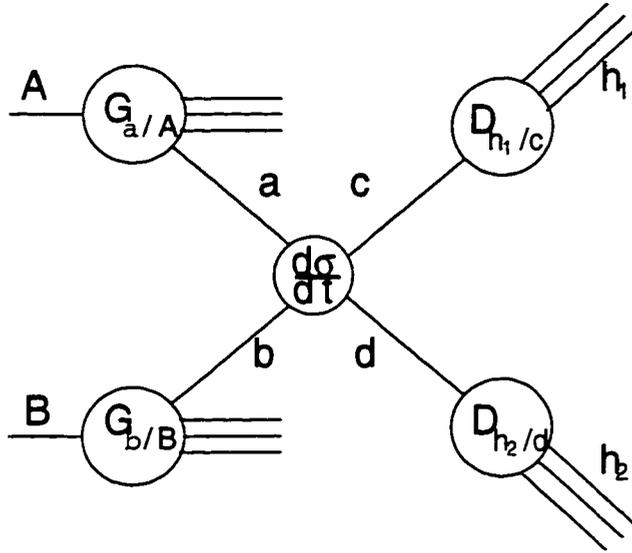
Figure 2.1: Schematic representation of a high-p_t reaction factorized into parton distribution functions (G), parton fragmentation functions (D), and a hard-scattering.

tum fraction between x and $x + dx$ is denoted by the *distribution function* $G_{a/A}(x)$. The probability of obtaining a hadron C with a momentum fraction between z and $z + dz$ from a parton c is denoted by the *fragmentation function* $D_{C/c}(z)$. These functions are purely nonperturbative and must, therefore, be obtained from data for various types of hard-scattering processes. The cross section for parton-parton hard scattering is calculated in the lowest order of perturbation theory. The expression for the invariant cross section is given by:

$$E_C \frac{d\sigma}{d^3 p_C}(AB \rightarrow C + X) =$$

$$\sum_{abcd} \int dx_a dx_b dz_C \, G_{a/A}(x_a) G_{b/B}(x_b) D_{C/c}(z_C) \frac{\hat{s}}{z_C^2 \pi} \frac{d\sigma}{d\hat{t}}(ab \rightarrow cd) \delta(\hat{s} + \hat{t} + \hat{u}) \quad (2.1)$$

The δ function appearing in Eq. 2.1 follows simply from two-body phase space kinematics for massless particles. Furthermore, the initial and final partons have been assumed to be collinear with the corresponding initial and final hadrons, i.e., no

6

parton transverse-momentum smearing has been included.

The power of the parton model is that it is not necessary to solve the problem of hadron binding completely. Instead, this information can be obtained from experiment. After measuring parton distribution and fragmentation functions in one experiment, they can be used to predict the results of other measurements.

2.2   QCD Formalism for Hard Processes

With the advent of QCD [6] , the fundamental ideas underlying the parton model received theoretical support through the introduction of quarks and gluons and the understanding of asymptotic freedom for short distances. Formally, the basic QCD equations are a non-abelian generalization of QED equations. Therefore, Feynman rules for QCD can be defined using prototype QED diagramatic with some additions like gluon-gluon interaction. When the lowest order QCD calculations are used, one reproduces the simple parton model. However, in QCD perturbation theory we have to consider the contribution from more complicated scattering processes. When higher order terms are included, one encounters divergences which must be *regularized* (rendered finite) and *renormalized* (properly subtracted) in order to yield meaningful finite results. After the process of renormalization is implemented, it is necessary to specify a momentum transfer scale at which a coupling of the theory will be defined. The renormalization scale will be denoted by a momentum transfer μ. Different choices of μ will result in different values for the "strong coupling" α_s. Since α_s is dimensionless, the dependence on the renormalization scale in regions of large momentum transfers Q^2 must be through dimensionless ratios of the form Q^2/μ^2.

7

The dependence of α_s on Q^2 is given by:

$$\frac{d\alpha_s(t)}{dt} = \beta[\alpha_s(t)] \qquad (2.2)$$

where $t = ln(Q^2/\mu^2)$ and the function β determines the sensitivity of the coupling constant to the choice of the renormalization scale μ. The parameter β can be calculated using next-to-leading order perturbation theory [7] :

$$\beta(\alpha_s) = -b\alpha_s{}^2 - c\alpha_s{}^3 \qquad (2.3)$$

where

$$b = \frac{33 - 2N_f}{12\pi} \qquad and \qquad c = \frac{153 - 19N_f}{24\pi^2} \qquad (2.4)$$

with N_f denoting the number of quark flavors. Integrating Eq.(2.2) yields the explicit $\alpha_s(Q^2)$ dependence :

$$\alpha_s(Q^2) = \frac{12\pi}{(33 - 2N_f)ln(Q^2/\Lambda^2)} \qquad (2.5)$$

where

$$\Lambda^2 = \mu^2 exp[-1/(\alpha_s(0)b)] \qquad (2.6)$$

sets the scale for the "running" coupling constant. Eq. 2.5 shows that $\alpha_s(Q^2)$ decreases as Q^2 increases. This property of the running coupling in QCD is the famous *asymptotic freedom* at small distances.

After determining the $\alpha_s(Q^2)$ dependence we have all the necessary tools to calculate the "hard" (i.e., perturbative) part of the cross section, and all we need to define for a complete description of a hard scattering processes are the non-perturbative distribution and fragmentation functions.

8

2.3 Parton Distribution Functions

In order to use the factorization technique, we must have the relevant distribution and fragmentation functions at the appropriate factorization scales. They are typically obtained by fitting some parameterization to data from various hard-scattering experiments at a scale $Q_0{}^2$. The evolution from one scale to another can be calculated using the Altarelli-Parisi equations [8]:

$$\frac{dG_{q_i}(x, Q^2)}{dt} = \frac{\alpha_s(Q^2)}{2\pi} \int_x^1 \frac{dy}{y} [P_{qq}(x/y) G_{q_i}(y, Q^2) + P_{qg}(x/y) G_g(y, Q^2)]$$

and

$$\frac{dG_g(x, Q^2)}{dt} = \frac{\alpha_s(Q^2)}{2\pi} \int_x^1 \frac{dy}{y} [\sum_i P_{qg}(x/y) G_{q_i}(y, Q^2) + P_{gg}(x/y) G_g(y, Q^2)] \qquad (2.7)$$

Here t is defined as $ln(Q^2/\Lambda^2)$ and the P functions are the inverse Mellin transforms of the appropriate anomalous dimensions specified by the theory [8].

The main source of information on parton distributions is the deep inelastic scattering (DIS) of leptons on nucleon and nuclear targets. However, as is well-known, inclusive DIS is mostly sensitive to certain combinations of quark distributions. Vector boson production - including the production of lepton pairs, direct photons and W's and Z's - provides important complementary information on parton distributions. Lepton pair production, for example, is sensitive to the anti-quark distributions. Direct photon production is particularly sensitive to the gluon distribution. Additional sensitivity to the gluon distribution can be obtained by using data for the photon plus jet cross section. For these reasons, it has become very popular to use a *global analysis*, where all available data sets are used to obtain parton distribution functions. Distribution functions produced by this global fit are characterized by the χ^2 per degree of freedom in the fit.

9

As a default set of distribution functions we will use the set abbreviated by "CTEQ" [9]. This set is the result of a global fit over more than 900 experimental points with 35 parameters. The total χ^2 for different versions of CTEQ is in the range of 860-948 [9].

2.4 Isolated Prompt Photon Cross Section

Now, after the above brief overview of the perturbative QCD formalism and hard-scattering phenomenology, we can apply the described methods to calculate the direct photon cross section.

At lowest order, $\mathcal{O}(\alpha\alpha_s)$, two-body subprocesses dominate the hadroproduction of direct photons, namely the QCD-Compton process ($qg \to q\gamma$) (Fig 2.2 a), and quark-antiquark annihilation ($q\bar{q} \to g\gamma$) (Fig 2.2 b). For the Compton diagram the elementary cross section can be written as

$$\frac{d\sigma}{dt}(qg \to q\gamma) = -\frac{\pi\alpha\alpha_s}{3s^2}e_q^2\frac{u^2 + s^2}{su} \tag{2.8}$$

and for the annihilation diagram

$$\frac{d\sigma}{dt}(q\bar{q} \to g\gamma) = \frac{8\pi\alpha\alpha_s}{9s^2}e_q^2\frac{u^2 + t^2}{ut} \tag{2.9}$$

where e_q is the charge of the interacting quarks in units of the electron charge, and s, u, t are the Mandelstam variables.

For low and intermediate energy photon production , the contribution from the $q\bar{q}$ subprocess is small, leaving as the dominant term Compton scattering. Based on the lowest order contribution alone (Eqs. 2.8, 2.9), one finds that at $\sqrt{s} = 1.8$ TeV and $P_T = 100$ GeV/c the annihilation process contributes only half as much as the Compton process. The latter is directly proportional to the gluon structure function,

10
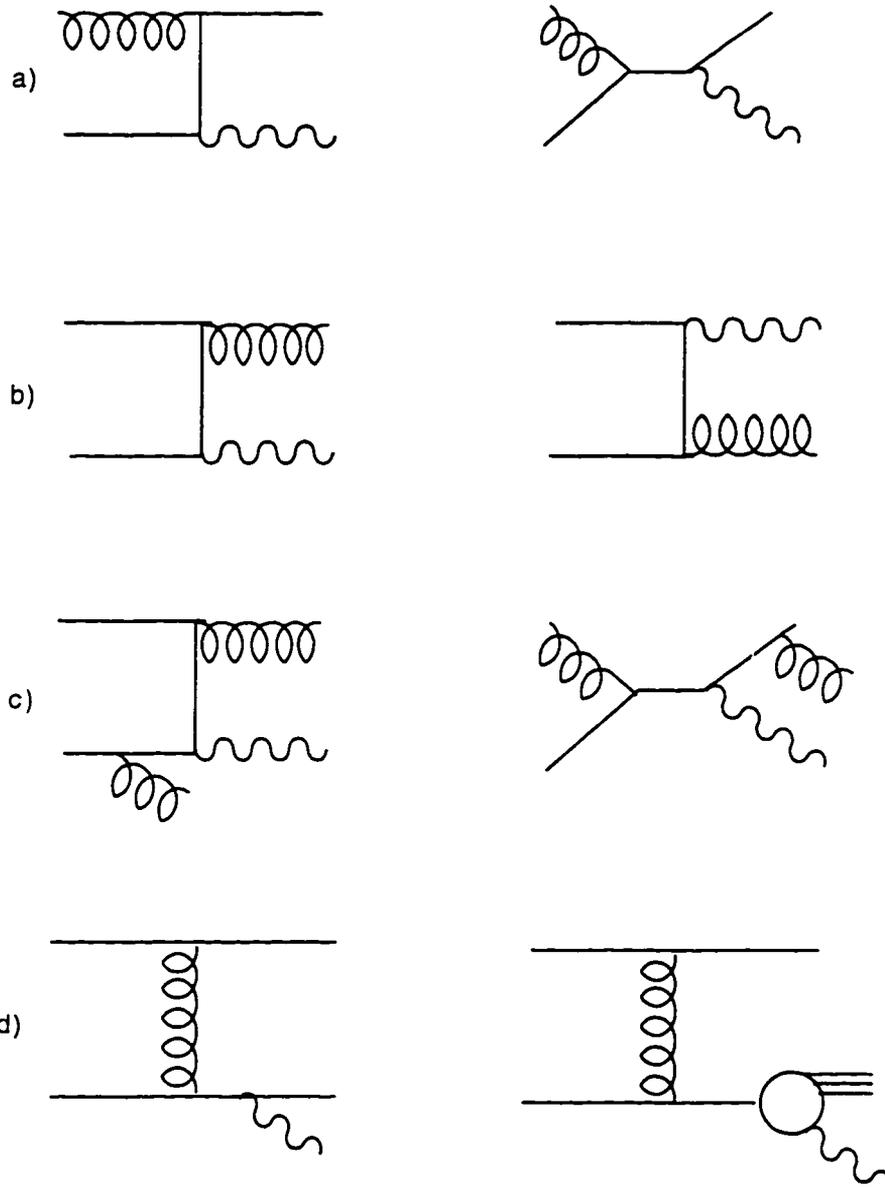
Figure 2.2: a) Leading order Compton QCD diagrams for prompt photon production, b) leading order annihilation diagrams, c) two examples of next-to-leading order diagrams, and d) two examples of photon bremsstrahlung, a perturbative QCD part (left) and a part using a photon fragmentation function (right).

11

and therefore provides the sensitivity of the direct photon cross section to the gluon content of the proton.

At next-to-leading order, i.e. at order $\mathcal{O}(\alpha\alpha_s^2)$, more complicated scattering processes appear (Fig 2.2 c), either due to an additional gluon attached to the Born diagrams, or due to photon bremsstrahlung of quark-quark scattering. The calculation of such diagrams is quite complicated, but the results are less sensitive to the choice of the renormalization scale.

Direct photons are not distinguishable from radiative photons (i.e. *bremsstrahlung*) accompanying high-p_t jets produced in regular hadron hard scattering. Therefore, the corresponding diagrams have to be included in calculations. Examples of bremsstrahlung diagrams (perturbative and non-perturbative) are presented in Fig 2.2 d. Although such terms appear only when calculating the higher order diagrams, they become prevalent at low P_T. For photons with pseudorapidity $\eta = 0$ and $P_T = 15$ GeV/c, bremsstrahlung contributes as much as (60-70)% of the total cross section. Such photons will, however, tend to be nearly collinear with the parent parton. Therefore, at collider energies, we are interested in *isolated* photons, i.e. photons that pass an isolation cut. An isolation cut positions a cone of opening angle δ in the photon direction (Fig. 2.3) and rejects events with total hadronic energy in the cone higher than E_{cut}. This definition can be converted into the isolation parameter $R = \sqrt{(\Delta\eta)^2 + (\Delta\Phi)^2}$ used in experiments, where η is the pseudorapidity and Φ is the azimuthal angle of the photon.

An additional reason for applying an isolation cut is that the inclusive photon cross section depends heavily on our knowledge of non-perturbative functions, particularly the fragmentation functions. At high energies or small x_T's, such knowledge becomes crucial due to the dominance of the fragmentation process. The isolation cut

12
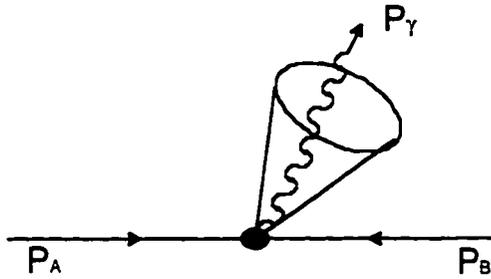
Figure 2.3: Diagram illustrating the isolation cone whose axis is the momentum direction of the photon.

reduces the contribution of photons produced through the fragmentation of a quark or a gluon, and makes theoretical predictions less sensitive to the nonperturbative fragmentation functions.

The isolated photon cross section can be considered to be the photon inclusive cross section minus the cross section of photons accompanied by hadronic energy greater than E_{cut} in the isolation cone. Because of the nonperturbative nature of the fragmentation function, theory cannot predict the energy distribution within the fragmentation region, and therefore we do not know how much hadronic energy from jet fragmentation will fall into or outside the isolation cone. However, we can use the fragmentation scale μ_F to control the transverse size of the jet. Different choices of μ_F are equivalent to changing the relative contributions to the cross section from perturbative and non-perturbative parts. Larger μ_F means more is included in the jet. Therefore, μ_F can be chosen small enough to make the whole jet small transversely so that it will fall either inside or outside the isolation cone. If the fragmentation jet fits within the isolation cone, the subtraction term for photons that fail the isolation cut should have the same form as the photon inclusive cross section, given by Eq. 2.1, except that the integration limits over the phase space are defined by E_{cut} and δ.

13
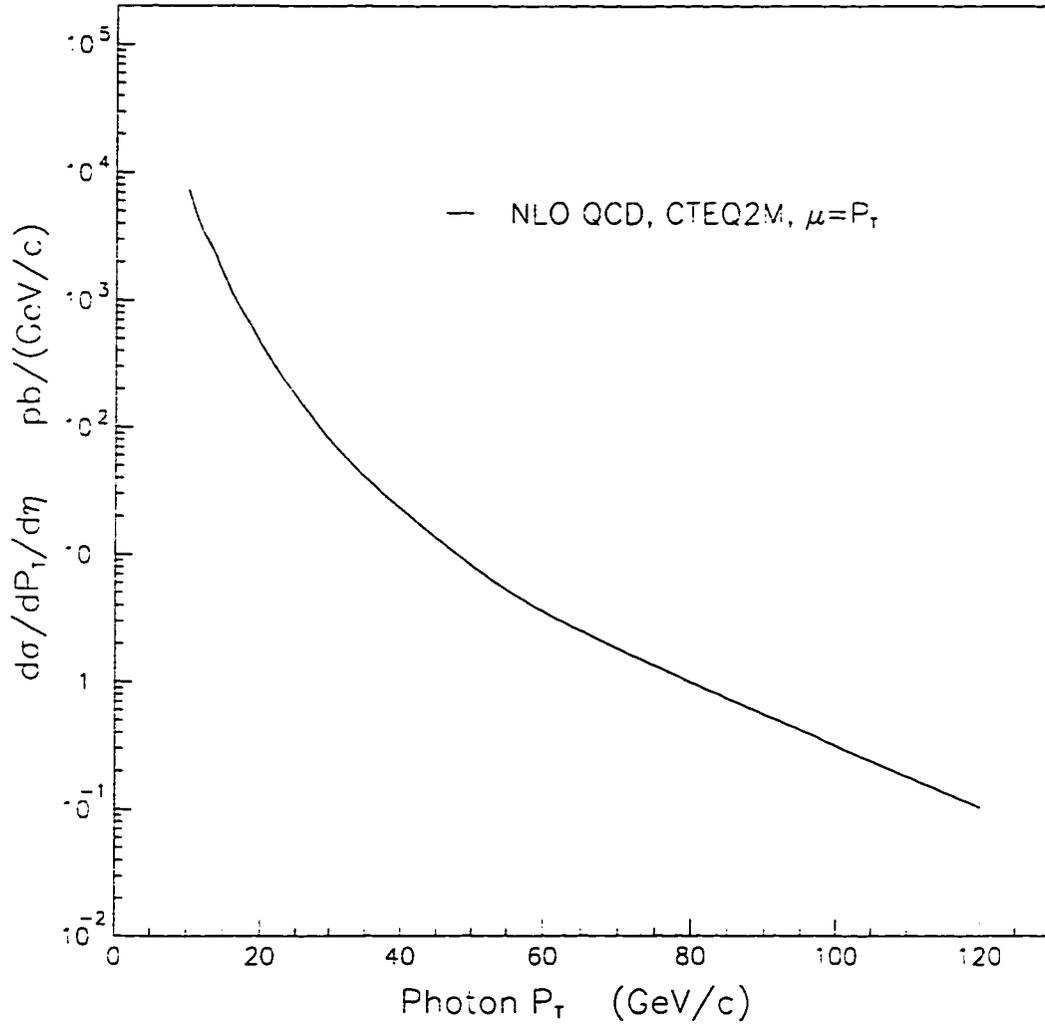
Figure 2.4: NLO QCD predictions for isolated prompt photon cross section in $\bar{p}p$

Collisions at $\sqrt{s} = 1.8$ TeV using CTEQ2M parton distribution functions.

14

Hadronic energy may enter the isolation cone not only from the fragmentation process but also from the non-fragmenting final state partons produced in the short-distance hard scattering. In the simplest case of the $2 \to \gamma + 2$ process, this means that one of the two final state partons can fall into the isolation cone of the photon. The phase space for a parton of momentum k in the cone is

$$\frac{d^3 k}{(2\pi)^3 2\omega} = \frac{1}{(2\pi)^3} \int_\delta d\Omega \int_{E_{cut}}^{\omega_{max}} \frac{\omega d\omega}{2} \tag{2.10}$$

where ω is the parton's energy and ω_{max} is fixed by kinematics. This subtraction term is perturbatively finite for fixed values of δ and E_{cut} and vanishes as $\delta \to 0$.

All these calculations have been performed [10] using a combination of analytic and Monte Carlo integration methods. A program for this calculation is available and has been applied with an isolation cut used in our measurement. Fig. 2.4 presents the result of a NLO QCD calculation for the direct photon cross section produced by this program. This calculation uses the CTEQ2M structure function and $\mu = P_T$. This curve will be used as the default theoretical prediction for comparison with experimental results.

2.5 Ambiguities in the theoretical predictions

We would like to conclude this chapter with a discussion of several uncertainties and ambiguities which exist in the described theoretical framework for direct photoproduction.

First, we examine the general question of the proper definition of Q^2 in the estimation of the scaling violations and of $\alpha_s(Q^2)$. Commonly, Q^2 is chosen to be in the range from $\frac{1}{2}P_T^2$ to $2P_T^2$. This uncertainty can cause the predictions to vary by a factor of two or more. A related problem is that the quark masses are not equal to

15

zero. For massless quarks, the number of flavors N_f is fixed and the running coupling α_s is determined by the single parameter Λ_{QCD}. In the presence of massive quarks, the situation is quite different [11]. Each heavy quark i with mass m_i is effectively decoupled from physical cross-sections at energy scales μ below a certain threshold Q_i which is of the order of m_i. Thus, the number of effective quark flavors N_f^{eff} is an increasing step function of the scale μ. Under these circumstances, the specification of the running coupling α_s is not as simple as for massless quark. As a result, the definitions of α_s and Λ_{QCD} in the presence of mass thresholds are not unique and the theoretical calculations depend on the renormalization scheme.

Another ambiguity arises from the fact that the partons do not necessarily collide collinearly, but they generally have a finite initial P_T because of their transverse Fermi motion within the hadron. This "intrinsic k_T", is usually introduced in the form of a Gaussian smearing of the parton's transverse momentum. Such smearing is unimportant at large P_T values, but cannot be ignored in the (5-10) GeV/c range. The parton model predicts a $< k_T >$ value of about 300 MeV, estimated from the size of the hadron using the uncertainty principle. QCD estimates a $< k_T >$ value in the order of 860 MeV (LO) and 600 MeV (NLO) from the study of high-mass lepton pair production in $q\bar{q} \rightarrow l^+ l^-$. In general, as more calculable QCD terms are included, the size of the deduced intrinsic term is decreased. All these calculations, however, are model-dependent, and the resulting uncertainty in the $< k_T >$ value can produce the largest ambiguity in the theoretical predictions for low-P_T direct photon production.

One of the most serious deficiencies of the theory is that higher-order contributions to the yield of direct photons are neglected. As we mentioned above, this is especially serious for the bremsstrahlung contribution. Additional sources of ambiguity are "higher-twist" effects in which one of the incident particles interacts directly

16

with a constituent from the other particle. However, because of hadronic form factors, such processes have very small cross sections.

Finally, there is the question of how well the theoretical isolation cut matches the experimental cut.

We will return to these questions again in the final chapter, when we will compare the theoretical predictions with the results of our measurement.

17

Chapter 3

Collider Detector at Fermilab

3.1 Tevatron Collider

The Tevatron at the Fermi National Accelerator Laboratory is currently the world's highest energy particle collider. It is a superconducting synchrocylclotron, two kilometers in diameter, which accelerates protons and anti-protons in opposite directions and brings them into head-on collisions. The Tevatron is the final stage of an acceleration process involving several individual accelerators. Figure 3.1 shows an overview of the various machines used to accelerate, store, and collide beams of protons and antiprotons at Fermilab.

The acceleration chain begins with doubly charged negative ions of hydrogen, which are accelerated by a Cockcroft-Walton electrostatic accelerator to 750 KeV. The electrons are then stripped from the hydrogen ions and the protons transferred to a 500 ft linear accelerator (LINAC) where they acquire 200 MeV energy and are sent on to the Booster Ring. This ring is a synchrotron of diameter 500 feet which boosts the protons to 8 GeV. At this point a pulse of roughly 10^{11} protons is injected into

18

Linac

Booster

CDF Detector

p

p̄

Tevatron

D0 Detector

Main Ring

Debuncher

Accumulator

Target
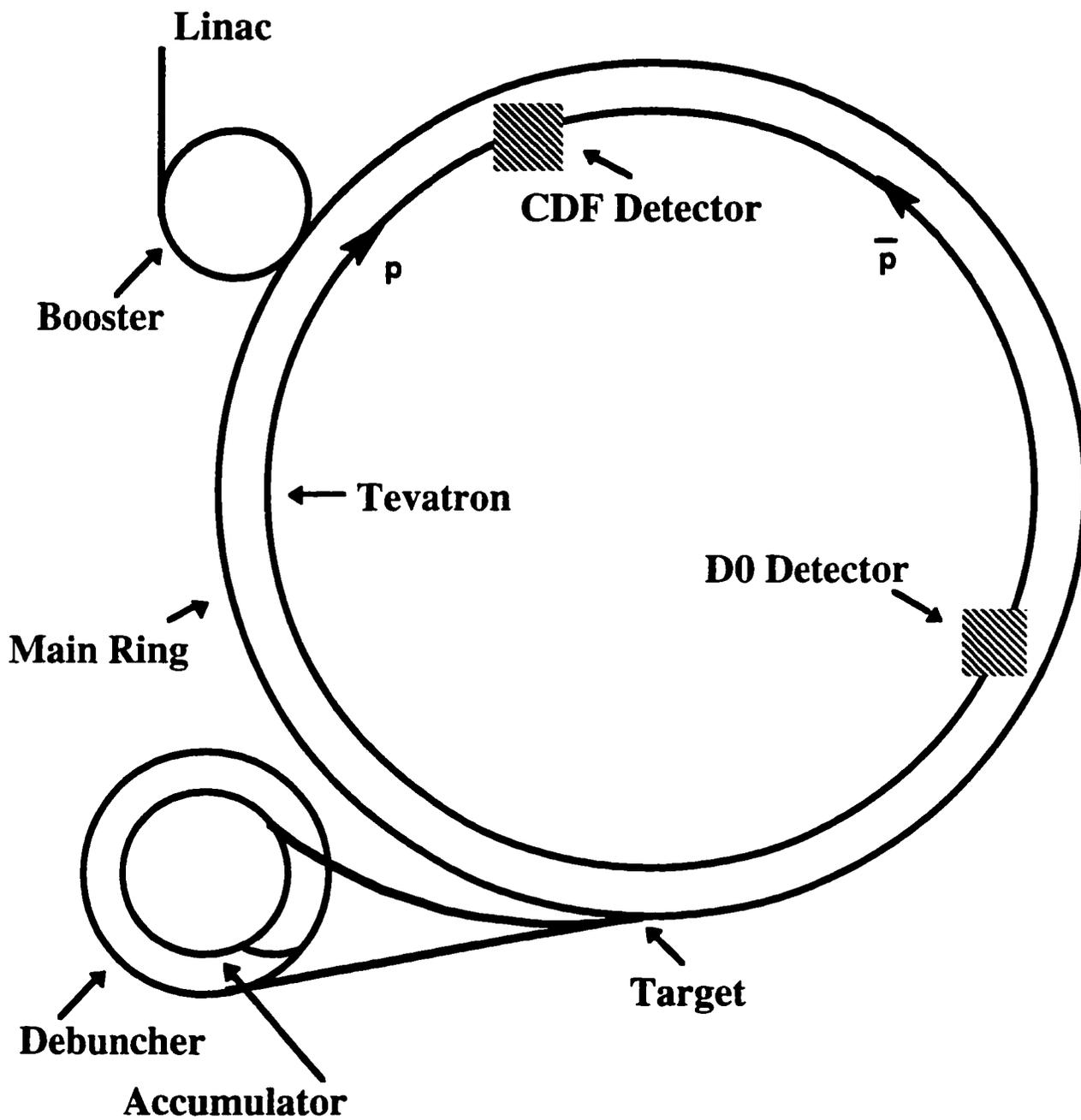
Figure 3.1: Layout of the Tevatron Collider at Fermilab.

19

the two kilometer diameter synchrotron, called the Main Ring. The Main Ring uses conventional, rather than superconducting, magnets, and can achieve a maximum energy of 400 GeV per beam. It is currently used to boost protons for the Tevatron, and to provide primary protons to the anti-proton source.

To produce antiprotons, the protons are accelerated to 120 GeV in the Main ring, and then extracted onto a Berylium fixed target, producing roughly 10^7 anti-protons. The anti-protons are collected in the Debuncher Ring where they are stochastically cooled before being stored in the Accumulator. This process is repeated until about 10^{10} anti-protons have been accumulated. Then, the $\bar{p}$ beam is transferred to the Main Ring where it is accelerated to 150 GeV before it is injected into the Tevatron. A proton beam is also injected into the Tevatron in the opposite direction. In the Tevatron, both proton and anti-proton beams are accelerated to 900 GeV and circulate in the same magnetic and RF fields in helical orbits. The beams intersect at four points, but the large transverse size of the beam minimizes collisions. Quadrapole magnets are then used to focus the beams at the B0 and D0 collision halls and electrostatic separators prevent collisions at the remaining collision points during normal running. The beams in the center of the CDF detector (B0 point) are roughly circular in cross section with a radius of 45 μm at 1 σ . Longitudinally, the beam bunches are approximately Gaussian with a width of 30 cm.

One of the most important characteristics of colliding beams in an accelerator is the luminosity L, which is defined by

$$N = L\sigma \qquad (3.1)$$

where σ is the cross section of the colliding particles and N is the number of collisions

20

per second. The luminosity is given by

$$L = \frac{N_p N_{\bar{p}} f}{4\sigma_x \sigma_y} \tag{3.2}$$

where N_p and $N_{\bar{p}}$ are the numbers of p and $\bar{p}$ per bunch, f is the bunch "collision" frequency, and σ_x and σ_y are the major and minor axes of the elliptical cross section of the beam profile at the interaction point. Focusing the beams using quadrapole magnets causes $\sigma_x \sigma_y$ to decrease, therefore L to increase.

As the beams circle around, N_p and $N_{\bar{p}}$ decrease from collisions with each other and with the gas in the beam pipe. The beam also undergoes emittance growth, that is, an increase in width. The luminosity decreases with time, with a lifetime which is typically 20 hours.

3.2 CDF Detector

The CDF detector (Figs. 3.2-3.3) is a general-purpose detector designed to study the physics of $p\bar{p}$ collisions at the Fermi National Accelerator Laboratory's Tevatron collider. The detector features near 4-π coverage with both azimuthal and front-back symmetry. Event analysis is based on the particle's charge, position, and momentum measurements and energy deposition in a calorimeter. The CDF detector is described in detail elsewhere [12]. In this chapter we briefly describe the detector, and in more detail, the detector subsystems which are particularly relevant to this analysis.

Tracking

CDF is equipped with several charged particle tracking systems which are positioned in a 1.4116 T axial magnetic field. The magnetic field is provided by a 4.8

21
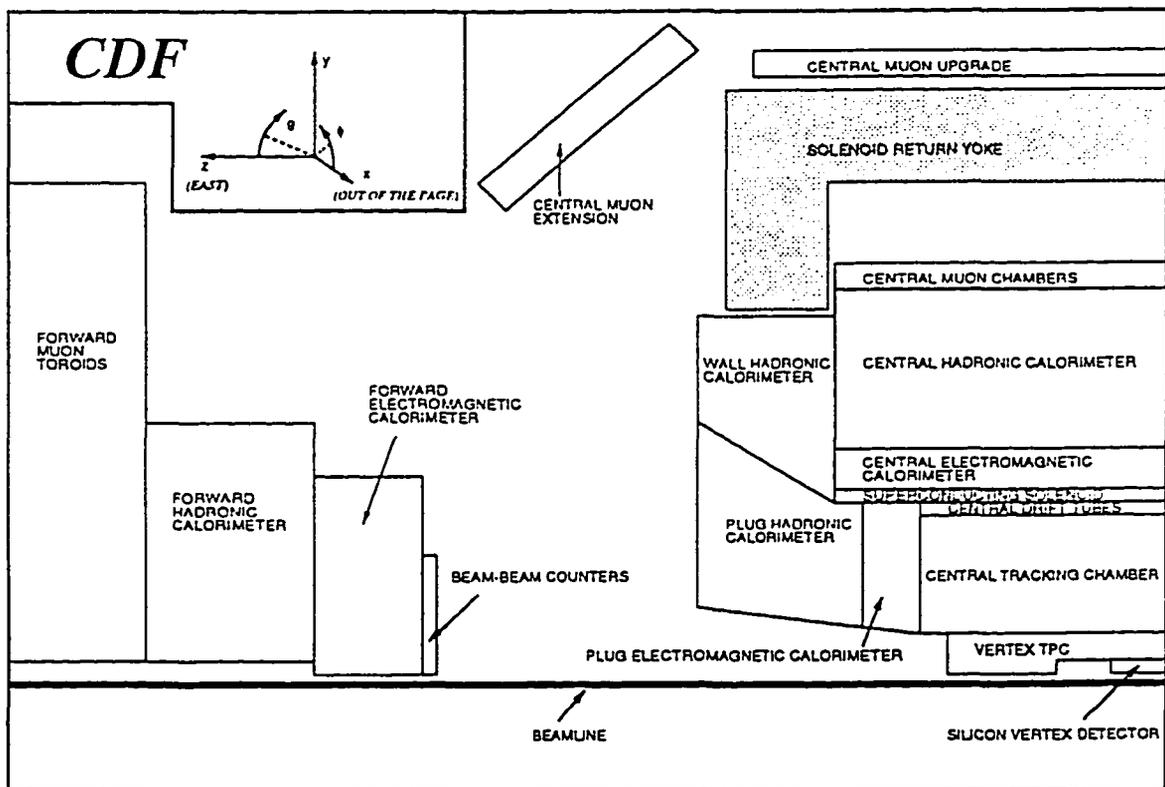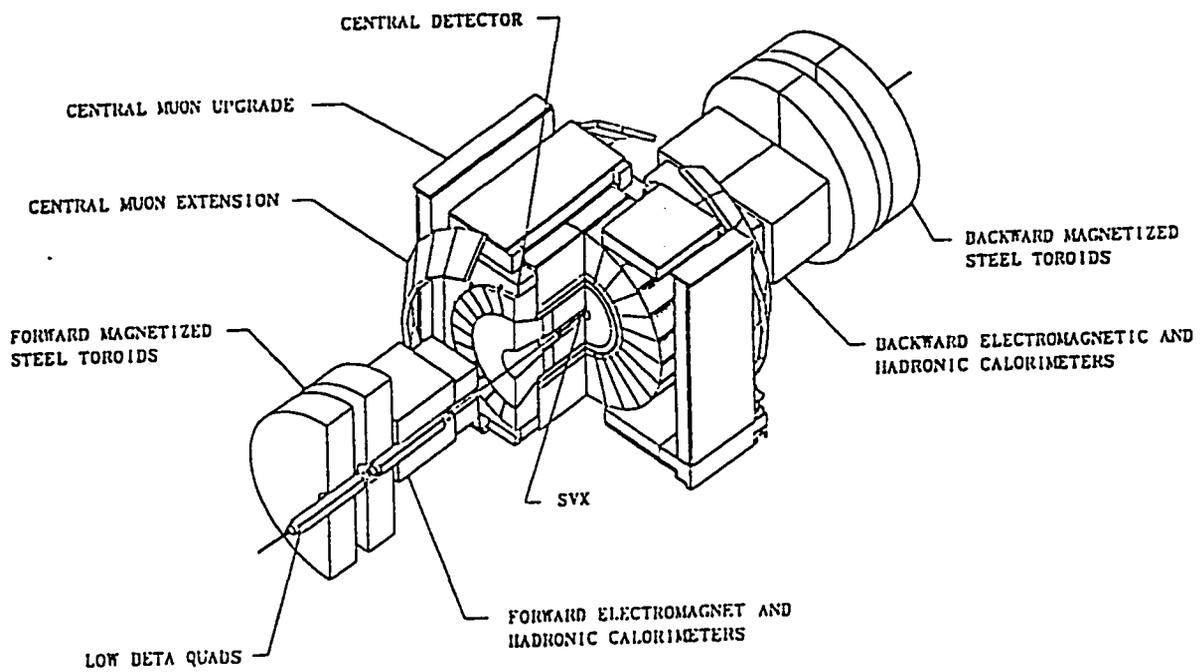
Figure 3.2: a) A perspective view of the CDF detector showing the central, forward, and backward detector components. b) A side-view cross section of 1/4 of the CDF detector. The detector is forward-backward and azimuthaly symmetric about the interaction region, which is at the lower-right corner of the figure.

22
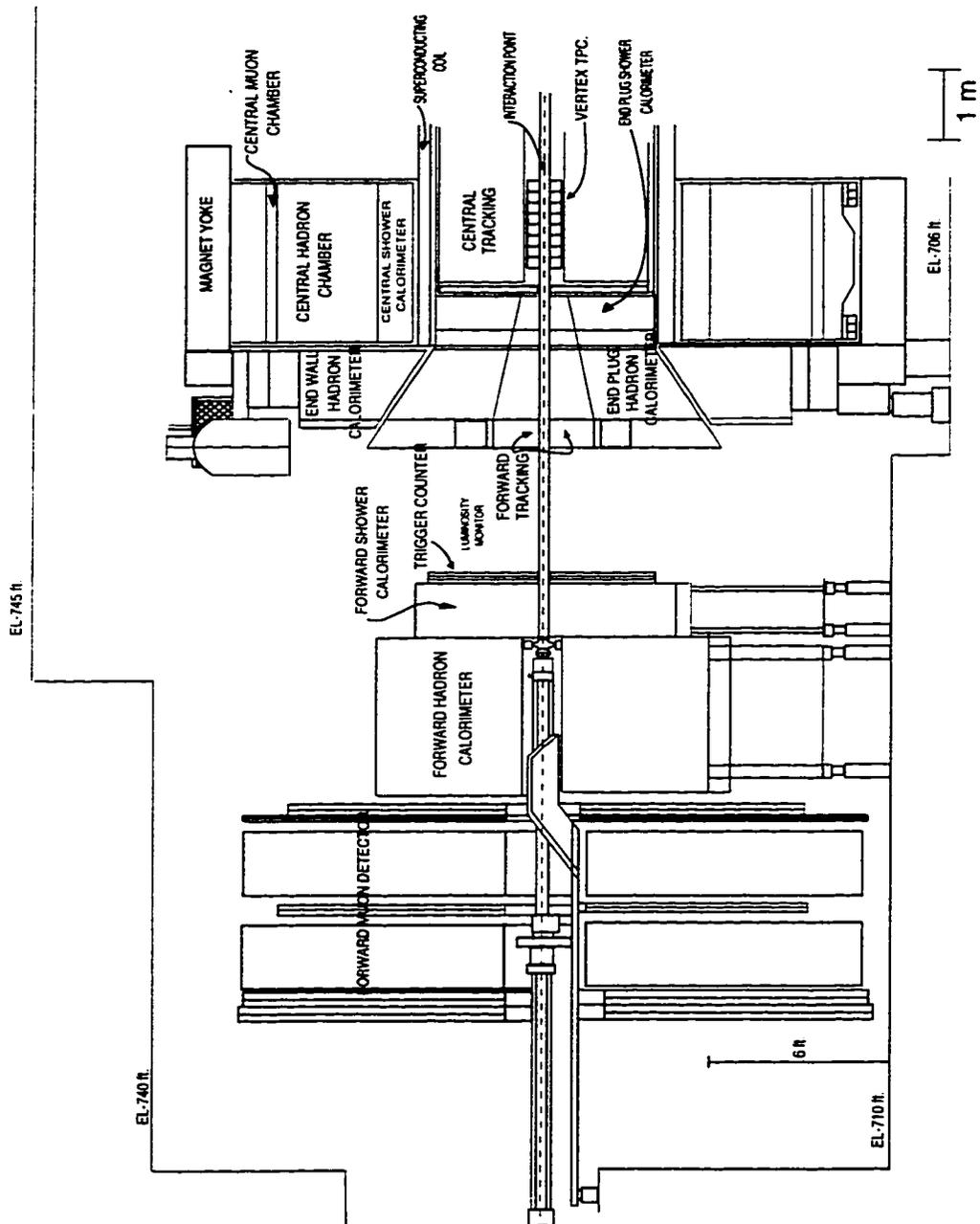
Figure 3.3: A cut-away view through the forward half of the CDF. The detector is forward-backward symmetric about the interaction point.

23

m long NbTi/Cu superconducting solenoid of radius 1.5 m and returned through a steel yoke which supports the detector.

The tracking system is used to provide position, momentum and charge information for charged particles along their helical trajectory in the solenoidal magnetic field. In addition, the absence of a track matched to an electromagnetic calorimeter cluster aids in the identification of photons. The primary components of the tracking system include the Silicon Vertex Detector (SVX), the Vertex Time Projection Chamber (VTX), and the Central Tracking Chamber (CTC) (see Figs. 3.2-3.3).

The SVX is positioned between the 1.9 cm radius berylium beampipe and the VTX. It consists of four layers of silicon strip detectors extending ± 25 cm in z at a radius of 2.9 to 7.9 cm inside the VTX. The SVX is segmented into two halves called barrels, which meet at $z = 0$. Each barrel is composed of 12 wedges and each wedge covers 30 degrees in azimuth.

The VTX is made up of eight octagonal modules with sense wires running perpendicular to the beamline. Each module is divided in two by a central high voltage grid, creating ~ 15 cm long drift regions. The inner section of the VTX has a cavity built into it which contains the Silicon Vertex Detector. The VTX is used to measure the $p\bar{p}$ interaction vertex along the z axis with a resolution of 1 mm. However, the ϕ resolution of the VTX is limited to knowing which octant the track traversed, so it cannot be used for a charge determination.

In our analysis we use the CTC to select electromagnetic clusters in the central electromagnetic calorimeter which do not have tracks matching them. This selection provides the neutral particle sample which is the source of photon candidates. We will discuss the CTC in detail below.

24

Calorimetry

CDF is equipped with electromagnetic and hadronic calorimeters, which provide full coverage in ϕ out to $|\eta|$ of 4.2 (see Figs. 3.2-3.3). The calorimeters utilize lead as an absorber for the EM and iron for the hadronic sections. The active sampling medium is scintillator in the central region, and gas proportional chambers in the plug and forward regions. All the calorimeters at CDF have been designed with projective towers, which point towards the nominal interaction region. Table 3.1 summarizes the properties of the various detectors comprising the CDF calorimetry.

The central calorimeter is made up of a series of wedges, each covering $15°$ in ϕ and containing an electromagnetic (CEM) section followed by a hadronic section (CHA). Each wedge is divided into ten projective towers, with each tower covering approximately 0.1 units in η. The Central Electromagnetic Calorimeter is the most important device in the measurement of direct photon characteristics. We will discuss the CEM in detail below.

To fill the gap between the hadronic sections of the central and plug , the "End Wall" hadronic calorimeter (WHA) covers the region $0.7 < |\eta| < 1.3$. Like the central calorimetry, these detectors use scintillator as the active medium and are divided into towers of $15° \times 0.1$ unit of η.

The plug EM calorimeter (PEM) is disk shaped with a diameter of 2.8 m and a depth of 50 cm. It is located 1.73 m in z from the nominal interaction point and covers the region $1.1 < |\eta| < 2.4$. It consists of 34 layers of proportional chambers sandwiched between lead plates. Each layer has a set of pads and anodes read out, and ten of the 34 layers have finely grained (0.01 units in $\Delta\eta$ and $1°$ in $\Delta\phi$) strips etched into the back of the pad G10 boards for position and shower shape determination. These plug electromagnetic strip chambers (PES) extend out

25

Calorimeter	η Coverage	Energy Resolution	Depth
CEM	$|\eta| < 1.1$	$13.7\%/\sqrt{E_T} \oplus 2\%$	$18\ X_0$
PEM	$1.1 < |\eta| < 2.4$	$28\%/\sqrt{E} \oplus 2\%$	$18\text{-}21\ X_0$
FEM	$2.2 < |\eta| < 4.2$	$25\%/\sqrt{E} \oplus 2\%$	$25\ X_0$
CHA	$|\eta| < 0.9$	$50\%/\sqrt{E_T} \oplus 3\%$	$4.5\ \lambda_0$
WHA	$0.7 < |\eta| < 1.3$	$75\%/\sqrt{E} \oplus 4\%$	$4.5\ \lambda_0$
PHA	$1.3 < |\eta| < 2.4$	$90\%/\sqrt{E} \oplus 4\%$	$5.7\ \lambda_0$
FHA	$2.4 < |\eta| < 4.2$	$130\%/\sqrt{E} \oplus 4\%$	$7.7\ \lambda_0$

Table 3.1: The CDF calorimetry. The detectors are divided into EM (xEM) and hadronic (xHA), which together cover all ϕ and $|\eta| < 4.2$. The symbol $\oplus$ signifies that the constant term is added in quadrature in the resolution. The shown energy resolutions were determined at a test beam using electrons for the electromagnetic calorimeters and isolated pions for the hadronic calorimeters. The "Depths" are given in radiation lengths for the electromagnetic and interaction lengths for the hadronic calorimeters.

to $|\eta| = 1.8$ and are located at shower maximum depth. The PEM is followed by the plug hadronic calorimeter (PHA).

Like the Plug, the forward calorimeters are based on gas proportional chambers with cathode pad readout. These chambers cover the region $2.2 < |\eta| < 4.2$.

Muon Detection

The CDF detector is equipped with a number of muon detecting devices located in the central and forward regions (see Figs. 3.2-3.3).

There are two sets of muons chambers in the central, $|\eta| < 0.6$, region of the CDF detector. Each set consists of four layers of drift chambers which have

26

their sense wires offset to allow resolution of the track ambiguity and determination of drift velocities. The Central Muon System(CMU) is located beyond the tracking chambers, solenoid and central calorimetry at a distance of of 3.487 meters from the beam axis. There are approximately 5 interaction lengths of material between the beam axis and the CMU detector. The central muon upgrade chambers (CMUP) are located behind ~ 8 absorbtion lengths of steel. The CMU and CMUP cover 85% and 80% in ϕ respectively. The CMU system is split into 48 identical subsystems each contained within one of the calorimeter wedges described earlier. Each subsystem is made of 3 smaller chambers to allow installation inside the wedge. Each chamber has 16 cells arranged in 4 layers and 4 towers wide.

In the region $0.6 < |\eta| < 1.0$ two pairs of free standing conical arches support the central extension muon chambers (CMX). These chambers provide coverage of 67% in ϕ and are located behind the central and wall calorimeters and the return yoke of the solenoid (~ 6 absorbtion lengths of steel).

In the forward region CDF has a forward muon system (FMU) which covers the region $2 < |\eta| < 3.6$ and consists of a pair of magnetized iron toroids.The drift chambers and scintillator counters instrumenting the toroids are used for muon momentum and charge determination.

Beam-Beam Counters

To measure the cross sections of various processes between elementary particles we need accurate measurement of the luminosity L. For these purposes CDF uses beam-beam counters (BBC) which provide the detector with the simplest $p\bar{p}$ - collision trigger, called the "minimum bias trigger", and measure the integrated luminosity. The Beam-Beam Counters (BBC) [13] are two planes of scintillator counters,

located near the beam pipes, at a distance of 5.8 meters (between the plug and the forward calorimeters) from the nominal interaction point on either side. The position of the BBC's is shown in Figs. 3.2-3.3.

Each plane consists of sixteen one inch thick scintillator counters. These counters are arranged in a criss-cross grid, which forms four concentric squares, and covers an angular range $4.5° > \theta > 0.32°$ ($3.2 < \eta < 5.9$). The planes on each side of the interaction point are used in coincidence (within a fifteen nanosecond gate) to signal an inelastic collision for the trigger. This minimum bias trigger rejects unwanted collisions between the beam and residual gas in the beam pipe, beam halo, and cosmic rays. The integrated luminosity can be measured by the beam-beam counters as the number of BBC east-west coincidences divided by the fraction of the $p\bar{p}$ total cross-section accepted by the BBC's. The acceptance of the BBC's was measured in a special run in which the elastic, single-diffractive and total cross-sections were determined.

Data Acquisition

The data acquisition system used at CDF consists of several parts, including the readout electronics, which convert the individual detector component analog signals into digital values, the triggers, which determine which events are written to tape, and the event management system, which gathers all the components of a single event together. The readout electronics are divided into two types of readouts, the RABBIT(Redundant Analog Bus Based Information Transfer) [14] system and FASTBUS [15].

The Rabbit system was designed by the Fermilab Particle Instrumentation Group. The CDF calorimetry and central muon systems are read out using the

28

RABBIT system. FASTBUS is a commercially available data acquisition system used at CDF to read out the tracking chambers and the trigger logic. Management of the data taking is handled by the FASTBUS system in combination with a DEC VAX cluster. The FASTBUS components of the data taking system are the trigger supervisor, the buffer manager, and the event builder. The trigger supervisor assignes an event number to each event and signals the other components in the system when all the detector components are digitized. The event builder takes all the digitized signals for one event and gathers them up into individual detector banks. The buffer manager checks the format of the event and controls its storage until it reaches final output on tape.

The Trigger System

The CDF trigger is a three level system. The lowest level requires that there be a tower in the calorimeter over a modest threshold (or hits in the muon chambers) and, that there be hits in the BBC counters. As the luminosity of the collider increased and the probability of an interaction per crossing exceeded one the BBC requirement was dropped. At typical luminosities this trigger had an accept rate of about two kHz.

The level two trigger is a FASTBUS based hardware trigger system. It is responsible for the identification of photons, leptons, and jets, and therefore the largest number of events are rejected at this level. Since the cross sections for physical processes are usually falling functions of E_T, the low-energy triggers are *prescaled*, i.e. only a fraction of these events is accepted.

The level three trigger is a Silicon Graphics CPU "farm" with 1000 MIPs of computing power. It consists of 48 CPU's, running in parallel, each with the ability

29

to have an event being read in or written out of its buffer space while a second event is being processed. The associated software is essentially the complete offline reconstruction code. The majority of the time is taken up by the track reconstruction. The primary difference between level 3 and offline analysis is that: E_T is calculated using $z = 0$ and final database constants for tracking and calorimetry are not available. The output from level three is written to 8 mm tapes at a rate of about 6 Hz. A fraction of the events, satisfying tight cuts, is flagged for immediate offline processing. These so called "Express Stream" events are used in this analysis after reprocessing with the final database constants.

3.3   Central Electromagnetic Calorimeter

The Central Electromagnetic Calorimeter [16] is the most important component of the CDF detector for the direct photon analysis.

The CEM is made up of a series of physically separate modules, called wedges, covering 15° in ϕ. The total number of wedges in the CEM is 48 (24 wedges at positive z and 24 wedges at negative z). In the η direction all wedges are divided into 10 towers (approximately 0.11 units of pseudorapidity). The basic layout of each module is shown in Fig 3.4. The CEM contains 30 3.2 mm thick lead layers interleaved with 31 5 mm thick layers of plastic scintillator. This lead-polystyrene sandwich has a thickness of eighteen radiation lengths. In order to maintain a constant radiation length for large θ, some lead layers are substituted by acrylic. Inside the CEM at the position of electromagnetic shower maximum are embedded the Central Electromagnetic Strip chambers, which improve position resolution for electrons and photons (see next section).

30
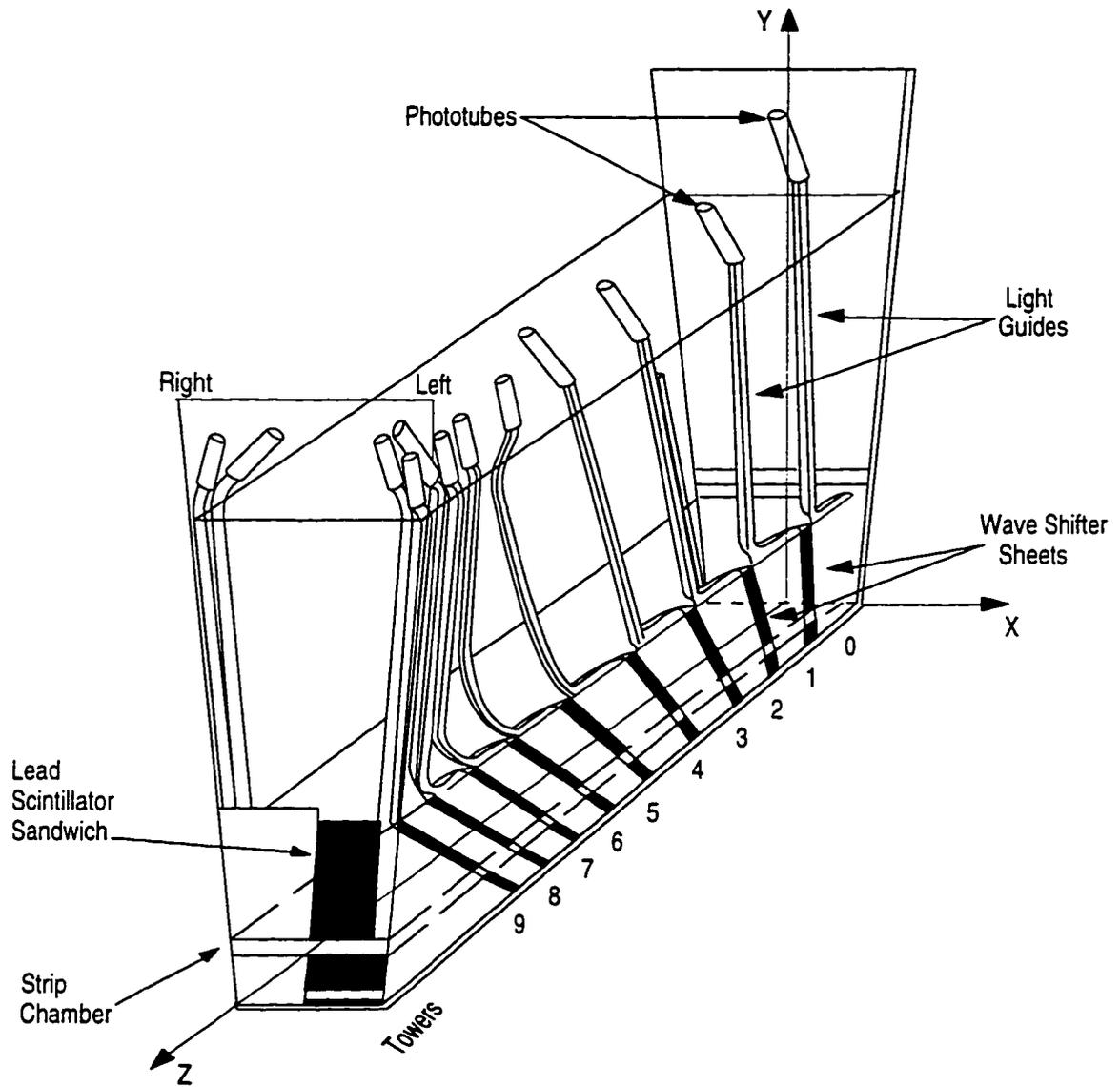
Figure 3.4: Layout of the CEM and CHA calorimeters with light gathering system in a single wedge.

31

All towers of each module of the CEM use the same signal collection method. The light from the scintillator is captured by wavelength shifters and transmitted by rectangular light guides, which run radially out of the calorimeter to photomultiplier tubes. The Photomultiplier tubes, which are positioned on both sides of each tower (see Fig. 3.4), also receive light signals from the calibration system.

There are three independent systems which provide the calibration of the CEM:

1. Cs^{137} **Source System.** Cs^{137} γ point-sources are moved by a computer controlled system across the tower of each module. The resulting phototube current profiles give information about the combined response of all signal collection components: scintillator, wavelength shifters, light guides, and phototubes for each tower.

2. **Xenon Flasher System.** This calibration system measures the light from the scintillator rod illuminated by xenon bulb flashes.

3. **LED Flasher System.** For each module three LED's flash green light into quartz fibers and calibrate the transition pieces between the light guides and photomultiplier tubes. This system maintains the initial calibration of the CEM, which was done with a beam of 50 GeV electrons at the NWest test beam at Fermilab.

3.4 Central Preradiator and Electromagnetic Strip Chambers

The Central Preradiator Chambers (CPR) and the Central Electromagnetic Strip Chambers (CES) [17] are proportional chambers located in the front of and within the Central Electromagnetic Calorimeter, respectively. In our analysis, we use these chambers to determine the electromagnetic shower position and to separate

32

direct photons from the neutral meson background.

The Central Preradiator Chambers are a set of multiwire proportional chambers, sampling the early development of electromagnetic showers that begin in the solenoid magnet material. The CPR is positioned at a radius of 168 cm from the beamline, between the Central Electromagnetic Calorimeter and the solenoid (1.075 X0). The chambers have 2.22 cm cells segmented in $r - \phi$, providing $r - \phi$ view from wire readout. There are 4 chamber divisions spanning ± 1 unit of pseudorapidity. The addition of the CPR in 1990 greatly improved the systematic uncertainties of our analysis and expanded the measured photon P_T range.

The CES consists of multiwire proportional chambers with strip and wire readout, located at a depth of 6 radiation lengths within the CEM calorimeter. This depth approximately corresponds to the shower maximum for electromagnetic showers. The chambers provide the photon position measurement as well as the transverse profile of the electromagnetic shower in both the z and $r - \phi$ views. The CES anode wires measure ϕ and the cathode strips measure η. Both views have a channel separation of roughly 8 mrad for measuring the transverse profile of electromagnetic showers.

3.5 Central Tracking Chamber

The Central Tracking Chamber [18] is one of the primary components of the CDF detector for our analysis. It provides precise momentum and position measurements of tracks for $|\eta| \leq 1.1$. In this region the CTC is highly efficient at finding tracks. In our analysis we use the CTC to reject all electromagnetic clusters in the central electromagnetic calorimeter associated with tracks in the CTC.

33

Strip Spacing =   1.67 cm in Towers 0-4
                  2.01 cm in Towers 5-9
Wire Spacing =   1.45 cm Throughout

Cathode
Strips →

z

x   Anode Wires (ganged in pairs)
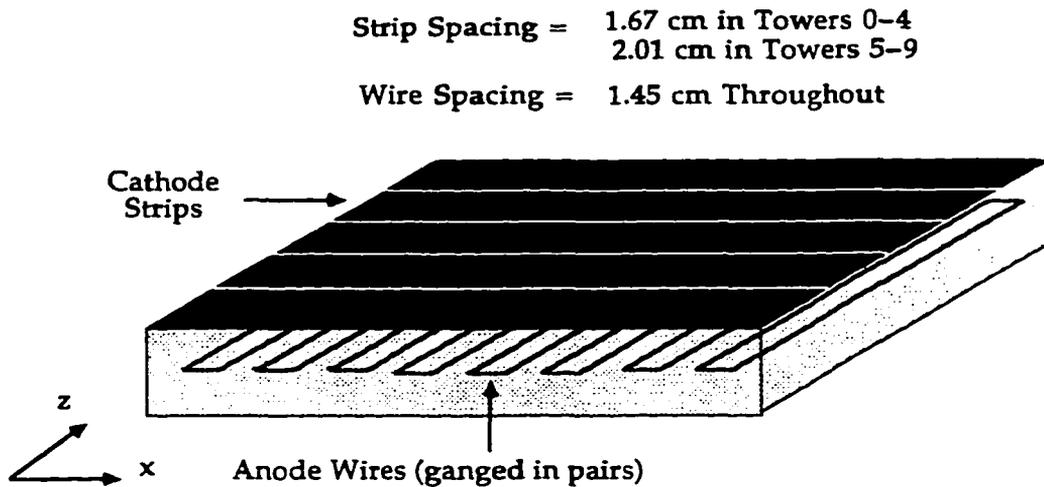
Figure 3.5: Two layers of the Central Electromagnetic Strip chambers

Physically the CTC is a cylindrical tracking chamber that envelopes the VTX in a 1.4 Tesla magnetic field, has a 0.3 meter inner radius and a 1.3 meter outer radius, and is 3.2 meters long. The CTC consists of 84 layers of sense wires, grouped into alternating layers of axial and stereo superlayers. The axial layers contain 12 wires and the stereo layers have 6 wires per layer. The outermost superlayer covers the area $40° \leq \theta \leq 166°$. In total, there are 6156 sense wires spaced 7 mm apart in the radial direction with a maximum drift distance of 35 mm.

The stereo wires are titled at 3 deg to the beam direction to obtain information on the polar angle of the track. The Lorentz angle of the electron drifting in the magnetic field is compensated for by tilting the cells of wires 45° relative to the radial direction. Thus the actual drift is perpendicular to the trajectory of high momentum particles. The efficiency of finding tracks and the resolution of tracks found falls off as the polar angle increases and fewer than 84 wires are traversed by the track.

The resolution for single hits is measured to be 300 μm. The r.m.s. momen-

34

tum resolution for tracks passing through every superlayer is $\delta p_t/p_t \leq (0.003\pm0.002)p_t$ in GeV/c. By requiring that the track come from the beam interaction point, the momentum resolution is reduced to $\delta p_t/p_t \leq 0.0011\ p_t$. This increase in resolution is effectively the result of increasing the track length from 1 meter to 1.3 meters.

Chapter 4

Trigger and Event Selection

4.1 Data Samples

For this measurement we have used the entire 1992-1993 Tevatron collider run data sample, which came from a set of three CDF triggers.

Each of the triggers consisted of three levels. The first level required that the total transverse energy of the event in any trigger tower be greater than 6 GeV with at least 4 GeV deposited in the electromagnetic section of the tower. Trigger towers subtend 0.2 units in rapidity and 15^0 in ϕ. Previously [4], in the second trigger level the only requirement was that 89% of the photon transverse energy be in the electromagnetic compartment of the calorimeter. A neural network ("NNet") hardware board was added at this level to require that the transverse energy in the 5×5 grid of trigger towers surrounding the photon candidate (equivalent to a cone with radius $R = \sqrt{(\Delta\eta)^2 + (\Delta\phi)^2} = 0.65$) be less than 5 GeV, thereby requiring the photon to be isolated. In the third level, software algorithms applied fiducial cuts to the photon and stiffened the isolation cut to 4 GeV in a cone of radius $R = 0.7$.

36

With the upgraded trigger no prescaling was necessary for the main photon trigger with threshold 16 GeV/c. Without the upgrade, a prescaling factor of approximately 100 would have been needed for the 16-30 GeV/c P_T range, due to trigger rate limitations. In addition to the main trigger, a $P_T > 6$ GeV/c prescaled trigger with the same isolation requirement was used, and a $P_T > 50$ GeV/c trigger without the isolation cut.

The 16 GeV trigger was not prescaled until the final stages of the run when it was prescaled by a factor of 2 at high luminosities. With this prescaling the effective integrated luminosity was 19.74 pb^{-1}. In addition, there were runs that had to be discarded due to the neural net not working, which reduced the luminosity to 18.14 pb^{-1}. The luminosity for the 6 GeV trigger without prescaling was 21.70 pb^{-1}. This value was reduced to 20.84 for bad runs, reduced further to 18.44 due to additional prescaling at the end of the run, and finally reduced to 16.85 pb^{-1} due to bad NNet runs. After taking into account the prescaling factor of 300, the total luminosity for the 6 GeV trigger was 56.15 nb^{-1}. An integrated luminosity of 21.85 pb^{-1} was acquired with the 50 GeV trigger. After excluding bad runs the luminosity went down to 20.97 pb^{-1}.

There were several sources of trigger inefficiencies: Level 1 failing to make a 6 GeV seed for the photon, Level 2 not making a cluster due to (HAD/EM) failing, or Level 2 cluster E_T being below the Level 2 E_T threshold. It was found [19] that for 9 GeV electrons all these effects are less than 1%. Since we are only using photons above 10 GeV, these effects were ignored.

In addition, there were two effects that sometimes caused the rejection of true direct photons by the isolation cut of the Level 2 NNet. First, true isolated photons might fail to pass the isolation cut due to resolution. The second effect is
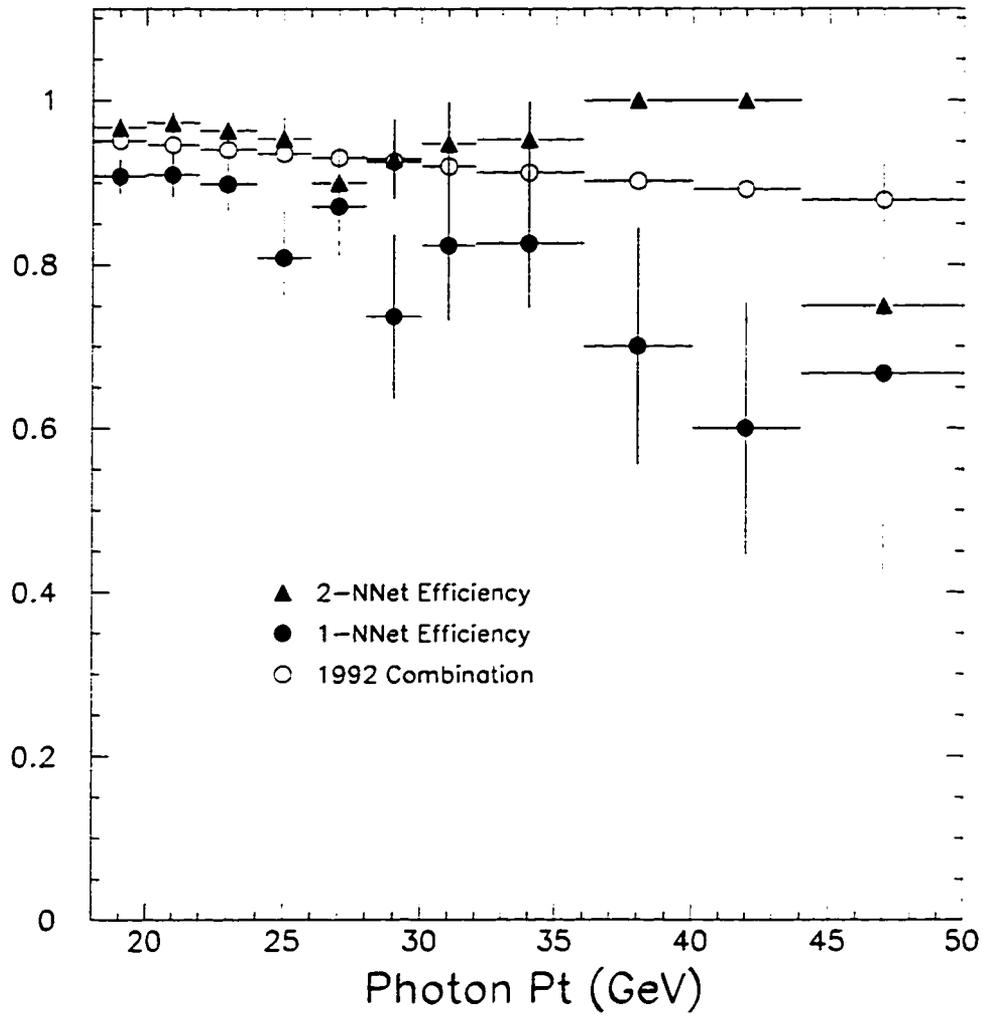
Figure 4.1: The efficiency of the photon neural network triggers

38
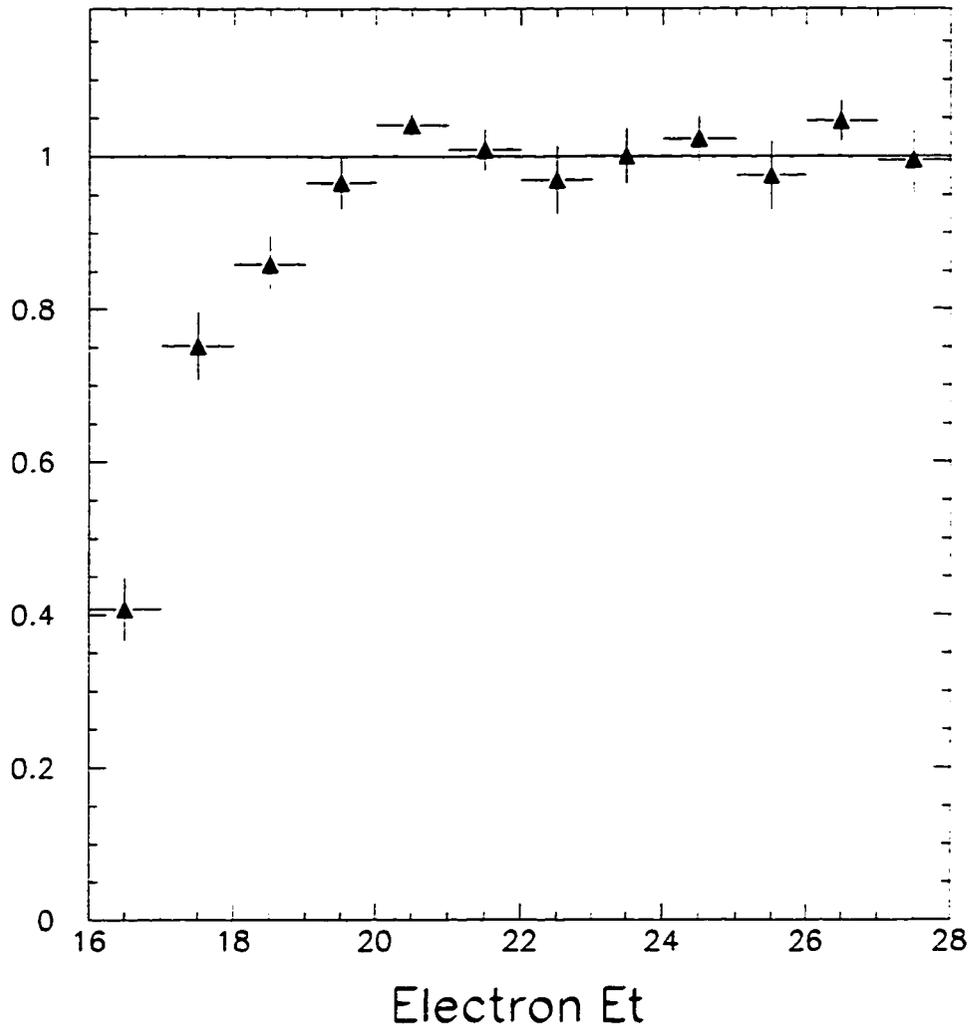
Figure 4.2: The E_T turn-on of the 16 GeV trigger

39

more complicated. Early in the run, the NNet was fed a seed cluster simply based on the smallest η position. If the jet opposite the photon was at a smaller η and made a 6 GeV seed, it would cause the event to fail due to the isolation cut. This effect was remedied by using a second NNET board and feed in the first two seeds. The second board was added for the last 73% of the data. These inefficiencies were measured by comparison of the data with the backup non-NNet triggers. Fig. 4.1 shows the efficiency of both triggers based on the 1-NNet running and the 2-NNet running and their combination using 27% 1-NNet and 73% 2-NNet.

Finally, we discuss the effect of the E_T turn-on of the 16 GeV trigger. The turn-on was measured by using good electron candidates from the 9 GeV electron trigger, and asking how often the 16 GeV NNet trigger fired versus the electron E_T. The plot of the efficiency vs photon P_T is shown in Fig. 4.2. This efficiency was corrected for the NNet efficiencies shown in Fig. 4.1, so the E_T turn-on and the NNet efficiency are not double counted. This is the reason why some of the points for $P_T > 20$ GeV are above 100%.

4.2 The Fiducial Cut

The fiducial cut was imposed to avoid uninstrumented regions at the edges of the CES. It requires the position of the shower with the highest E_T to be within 17.5 cm of the chamber center in the azimuthal direction (perpendicular to the wires) and to have 14 $cm < |Z| < 217$ cm (i.e. to be within the active region of the strip chamber). The region remaining after this cut is 64% of the solid angle for $|\eta| < 0.9$.

In order to avoid events with complex projective detector geometry, events with a Z_{vertex} more than 60 cm away from the nominal vertex position were rejected.

40

This cut is slightly different than the cut used in the 1989 analysis [4], which required $|Z_{vertex}| < 50cm$. The efficiency of the Z_{vertex} cut is 95% [20].

4.3 The Isolation Cut

As we mentioned in chapter 2, at collider energies experiments detect *isolated* photons in order to avoid photons from fragmentation processes at high energies and small x_T. The isolation cut requires that the extra transverse energy inside a cone of radius $R = \sqrt{\Delta\eta^2 + \Delta\phi^2}$ centered on the photon has to be lower than some threshold. To avoid trigger prescaling, the isolation cut was applied on the hardware level, selecting only events with extra energy below 4 GeV in a cone with $R = 0.7$. Then, the isolation cut was tightened to 2 GeV in a cone with the same radius, which improved the signal/background ratio.

To estimate the isolation cut efficiency, the following approximation was used [22]. We measured the transverse energy sum E_T within randomly placed cones of radius 0.7 in minimum bias events and assumed that it represents the approximate underlying sum E_T in direct photon events. As an additional condition we selected only those random cones in minimum bias events which do not have tracks near their centroids (the efficiency of the no-track cut is discussed in the section 4.4). Fig. 4.3 shows how good this approximation is by comparing the sum E_T distributions in a cone of $R = 0.7$ for direct photon underlying and minimum bias events. The difference of the efficiencies corresponding to the two distributions is 6% for a 2 GeV cut, 4.5% for a 3 GeV cut and 3% for 4 GeV cut.

The distribution of extra energy in the cone does not depend on the photon P_T, but depends strongly on the number of interactions in the underlying event. This

41
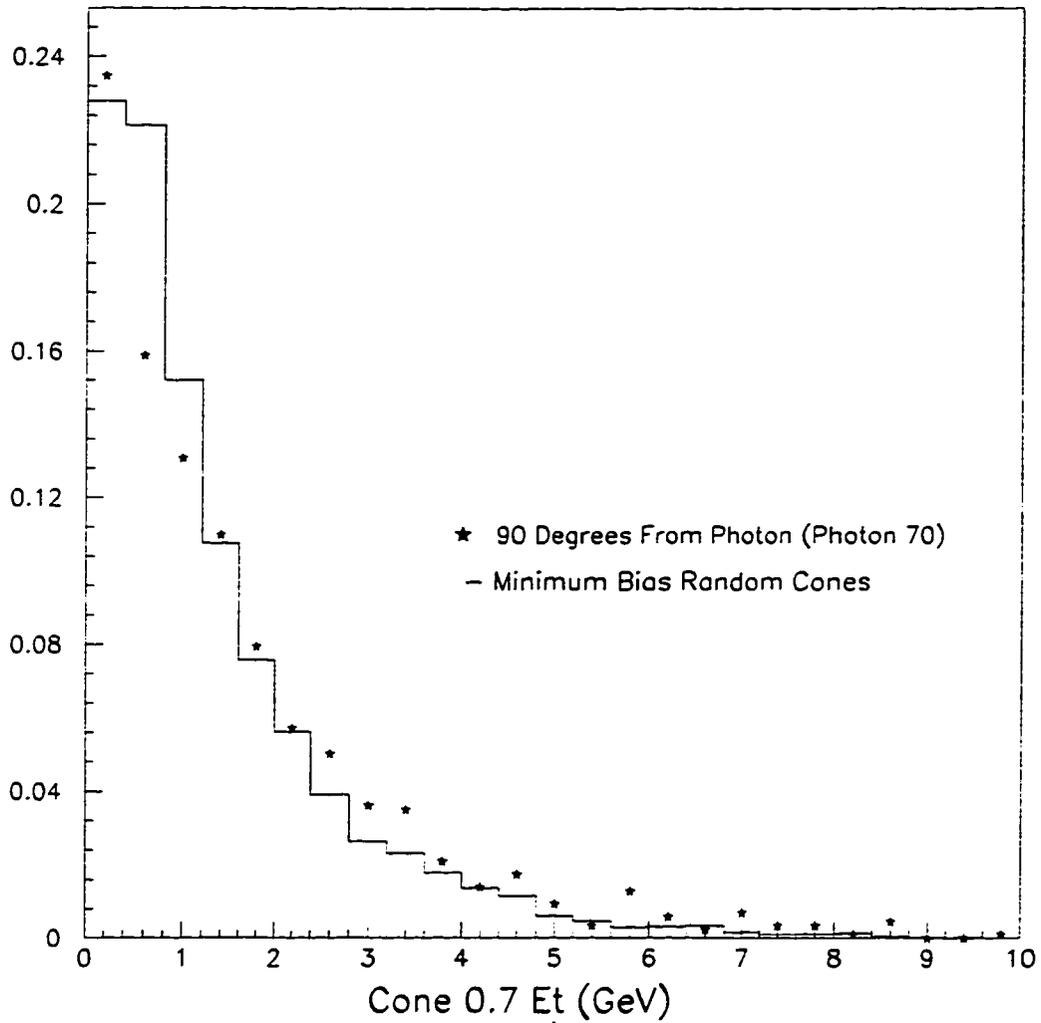
Figure 4.3: Comparison of the sum E_T distributions within a cone of radius 0.7 for direct photon underlying events (stars) and for minimum bias events (solid line).

42
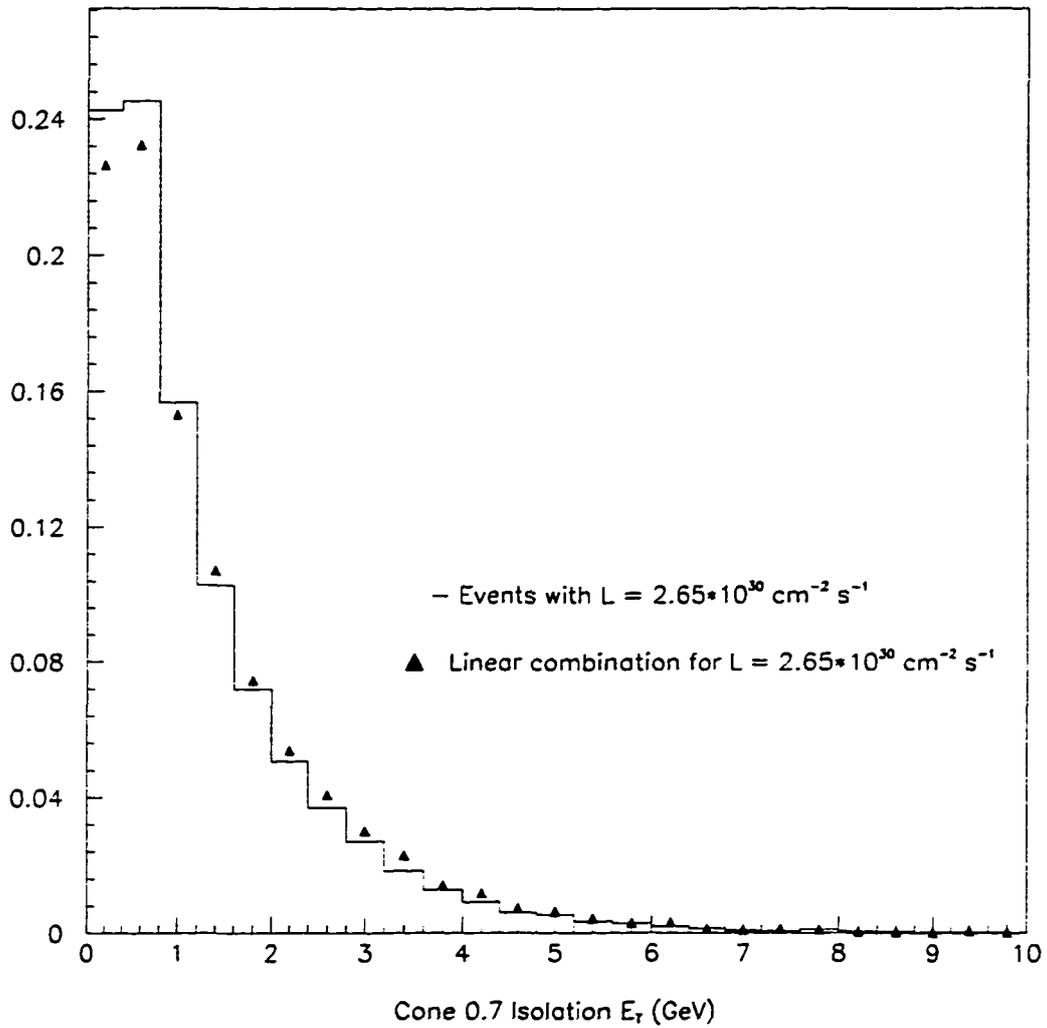
Figure 4.4: E_T distribution for events with average luminosity $2.65 * 10^{30}cm^{-2}s^{-1}$ (solid line), compared to the linear combination of distributions with different numbers of interactions corresponding to the same luminosity. The distributions are normalized to unit area.

43

number can be estimated from the luminosity [21] :

$$< n >= L \frac{46.8\,mb}{286.28\,kHz}$$

(4.1)

where L is the instantaneous luminosity, $46.8\,mb$ is the beam-beam counter cross section, and $286.28\,kHz$ is the rate of beam crossings[21].

Using Poisson statistics

$$P(n) =< n >^n \frac{e^{-<n>}}{n!}$$

(4.2)

we can calculate the contribution to the data sample of events with different number of interactions for a given instantaneous luminosity (Tab. 4.1).

	$L = 1.0$	$L = 2.5$	$L = 5.0$	$L = 7.5$	$L = 10.$
1 Interaction	92.1%	80.9%	64.6%	50.9%	39.6%
2 Interactions	7.52%	16.5%	26.4%	31.2%	32.4%
3 Interactions	0.41%	2.25%	7.20%	12.8%	17.6%
4 Interactions	0.02%	0.23%	1.47%	3.91%	7.21%
5 Interactions	10^{-3}%	0.02%	0.24%	0.96%	2.36%

Table 4.1: The weights of different number of interactions for given luminosities.The luminosity is in units of $10^{30}cm^{-2}s^{-1}$ and events without interactions are excluded.

44

Fig. 4.4 shows the distribution of energy in a cone $R = 0.7$ for events with average instantaneous luminosity $2.65 * 10^{30} cm^{-2} s^{-1}$ and the linear combination of distributions for events with different numbers of interactions corresponding to the same luminosity. The integral of the two distributions differs only by 3% above 2 GeV, 2% above 3 GeV , and less than 1% above 4 GeV. This result allows us to use linear combinations to reconstruct the E_T distribution for any given average luminosity and use it to calculate the isolation cut efficiency. Fig. 4.5 shows the efficiency of the isolation cut vs. energy E_T in a cone 0.7 of minimum bias events for data with different luminosities. The average E_T's for combinations of luminosities and energy cuts are presented in Tab. 4.2.

An important question is how to handle the fact that the luminosity changes within a run. If the cut efficiency is not linear with luminosity, then just using an average luminosity for each run would not be quite correct. Fig. 4.6 shows the isolation cut efficiency vs. instantaneous luminosity. The curves are almost linear, which means that we can use the average luminosity to calculate the isolation cut efficiency.

Using the described technique it is possible to calculate the isolation cut efficiency for a given average luminosity, cone size and energy cut. We assume that possible systematic errors will be due to the difference between the E_T distributions of underlying events, the choice of cone size and the use of the linear combination for 1-5 interaction events. The average instantaneous luminosity for our data set (complete data sample) is $3.16 * 10^{30} cm^{-2} s^{-1}$ and the corresponding isolation cut efficiency for cone of radius 0.7 and a 2 GeV E_T cut is 0.78 ± 0.0234.

45

	$\overline{E}_T(E_T < 2 \text{ GeV})$	$\overline{E}_T(E_T < 3 \text{ GeV})$	$\overline{E}_T(E_T < 4 \text{ GeV})$	$\overline{E}_T(E_T < 10 \text{ GeV})$
1 Int.	0.78 GeV	0.93 GeV	1.01 GeV	1.12 GeV
L = 2.5	0.83 GeV	1.04 GeV	1.17 GeV	1.35 GeV
L = 5.0	0.88 GeV	1.13 GeV	1.30 GeV	1.59 GeV
L = 7.5	0.93 GeV	1.22 GeV	1.44 GeV	1.85 GeV
L = 10.0	0.97 GeV	1.31 GeV	1.58 GeV	2.12 GeV
70 GeV smp.	0.89 GeV	1.09 GeV	1.23 GeV	1.45 GeV

Table 4.2: The average E_T in a cone $R = 0.7$ for combinations of luminosities and energy cuts.

46
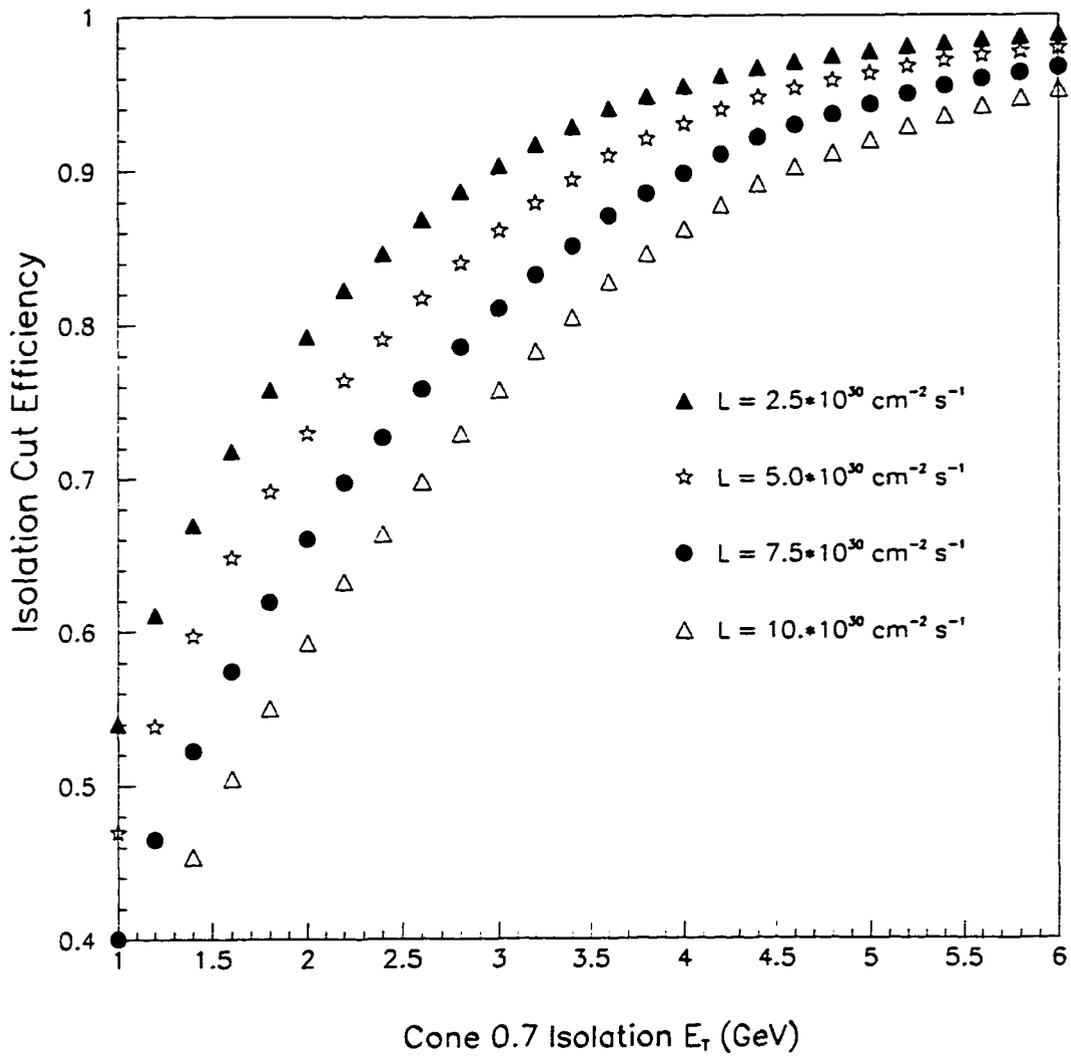
Figure 4.5: Isolation cut efficiency vs. energy in the cone.

47
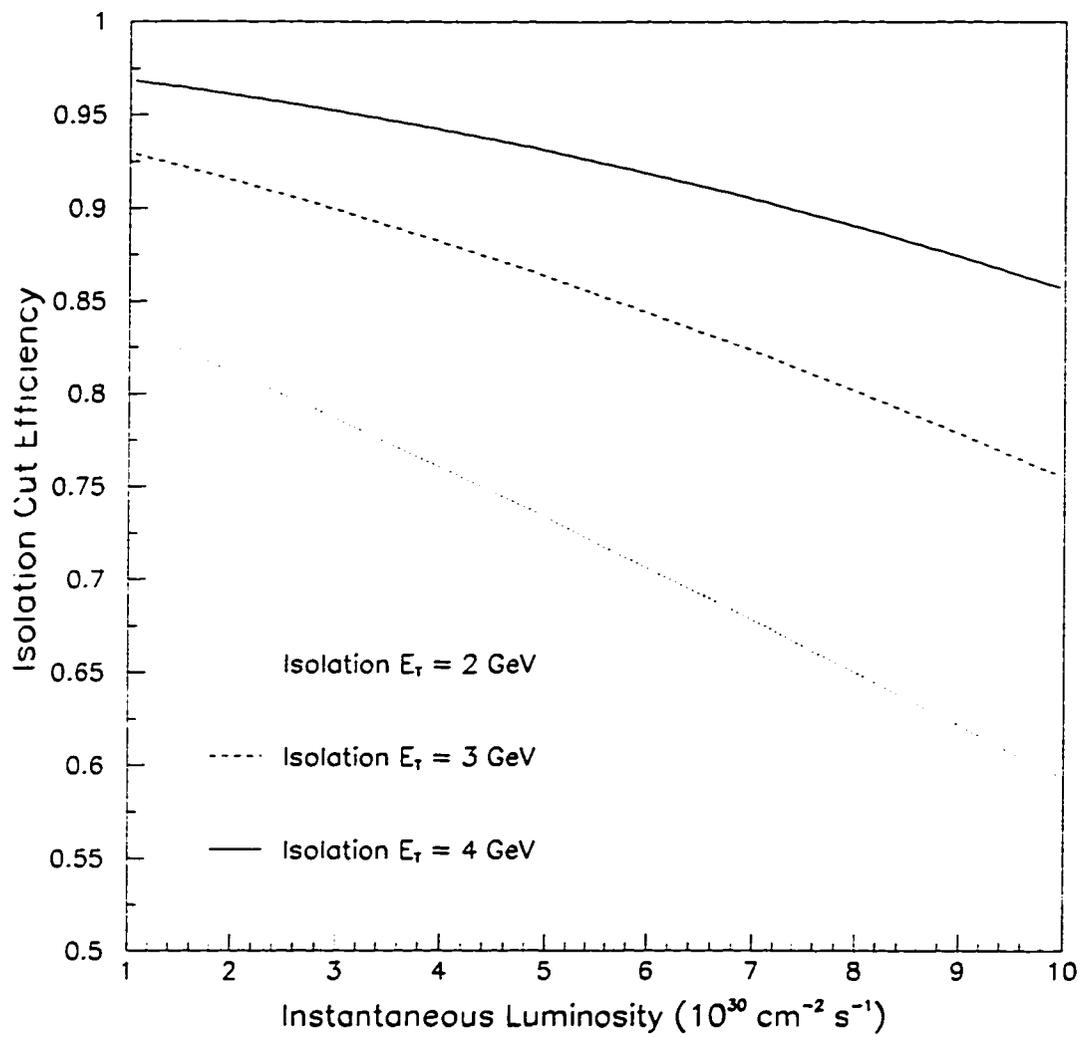
Figure 4.6: Isolation cut efficiency vs. luminosity for 2, 3, and 4 GeV cuts.

48

4.4 The No-Track Cut

The no-track cut requires that there be no track pointing at the CPR chamber where the photon candidate is. This is a minor additional requirement to the 1989 analysis, which eliminated events with 3 dimensional tracks in the tower of the candidate [4]. It was added due to sensitivity of the conversion method (chapter 5) to additional particles in the calorimeter wedge.

Direct photons can fail the no-track cut in two ways. First, they may convert in the material in front of the CTC. Using a calibration by the CDF W mass group, this material amounts to 7.51% X_0 with a 7% uncertainty, leading to a 6% correction to the photon cross section with a 0.4% uncertainty.

The second way direct photons can fail the no-track cut is when they combine with a track from the underlying event. Using minimum bias data we measured the efficiency of this cut (we used the same assumptions as in the isolation cut case) [22] to be 95% for the data sample with luminosity $L = 1*10^{30} cm^{-2}s^{-1}$ and 93% for $L = 3.16*10^{30} cm^{-2}s^{-1}$. Therefore, we use a 7% correction with 1% uncertainty for charged tracks from the underlying events .

4.5 The Extra Strip/Wire Cut

The single and multiple meson backgrounds are all reduced by requiring that there be no other photon candidates above 1 GeV in the CES. The efficiency of this cut depends on the energy of the photon candidate. Fig. 4.7 shows the efficiency of the cut for electrons measured in the 1985 test beam [23] and for electrons from W boson decay (both simulated and measured). The efficiency of electrons from W decay is lower than the extrapolation from the test beam electrons due to the radiation of

49
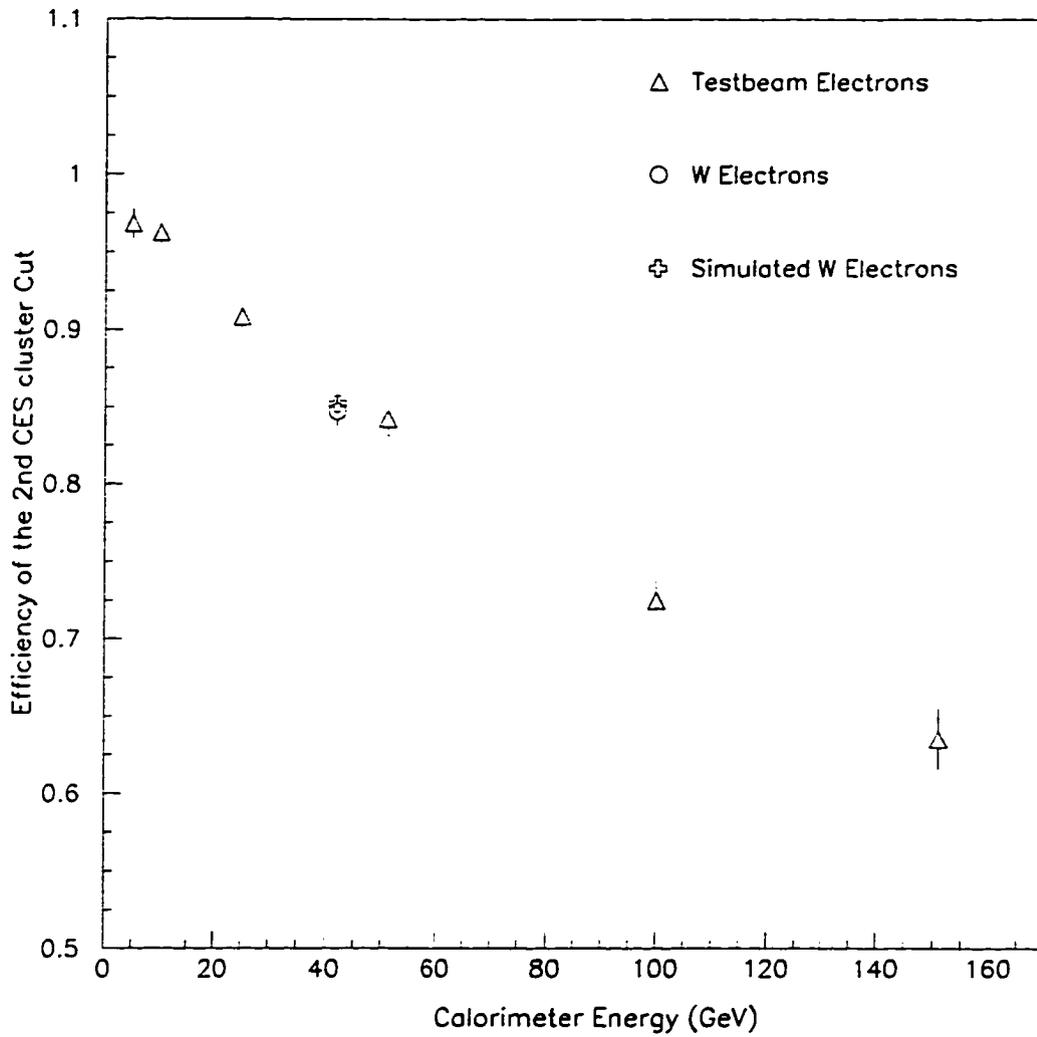
Figure 4.7: The efficiency of the 2nd CES cluster cut as a function of electron energy for test beam electrons, and for electrons from W decay.

50

an extra photon in this physics process. The efficiency of the extra strip/wire cut changes from 94% to 87% as the photon P_T increases from 16 GeV/c to 40 GeV/c [4].

4.6 $\chi^2 < 20$ Cut

Events were also eliminated if the single shower fit to the standard test beam electron profile [23] had a χ^2 larger than 20. The details of this fit, which is the main tool of the *profile method*, are described in chapter 5. The $\chi^2 < 20$ cut provides significant rejection against multiple photon backgrounds (particularly photons from η decay) and is almost 100% efficient for direct photons.

4.7 The Missing E_T Cut

Cosmic ray muons can radiate a photon in the CEM and fake a photon signal. The characteristic signature for this process is that there is no jet on the other side of the event. The cosmic ray background was eliminated in the 1989 analysis [4] by a missing-E_T significance cut (missing E_T divided by the square root of total E_T). The cut was rejecting all events with missing E_T significance above 3. This is very efficient for lower P_T photons, but we have discovered that at higher P_T, when jets hit calorimeter cracks, the significance can be larger than 3.

This is demonstrated in Fig. 4.8, which shows the significance for photons above 70 GeV. Thus, we would either have to vary this cut with photon E_T or modify it. We chose to use a variable used by the dijet and excited quark analyses: the missing E_T divided by the cluster E_T (or photon E_T in this case). Fig. 4.9 shows this variable for photons above 70 GeV, there is a clean separation with a cut at 0.8.

51
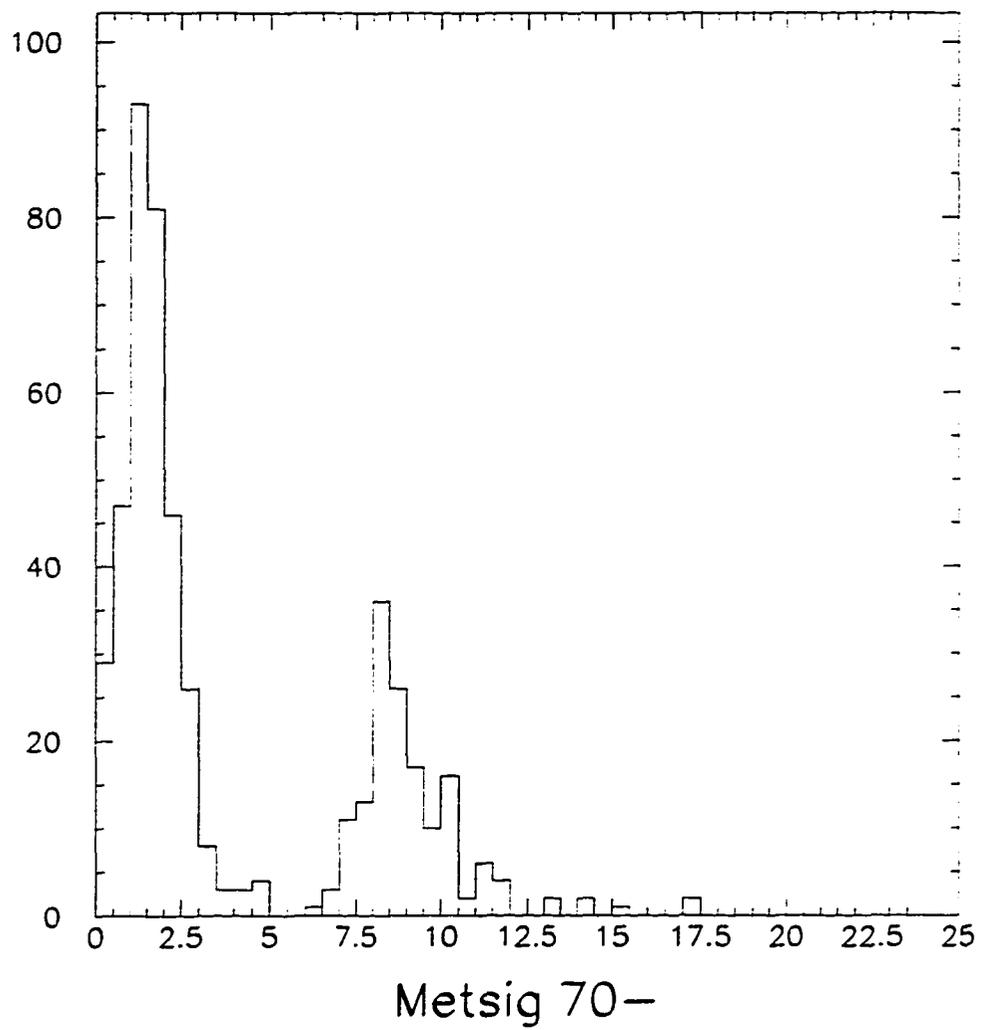
Figure 4.8: The missing E_T significance for photons above 70 GeV.

52
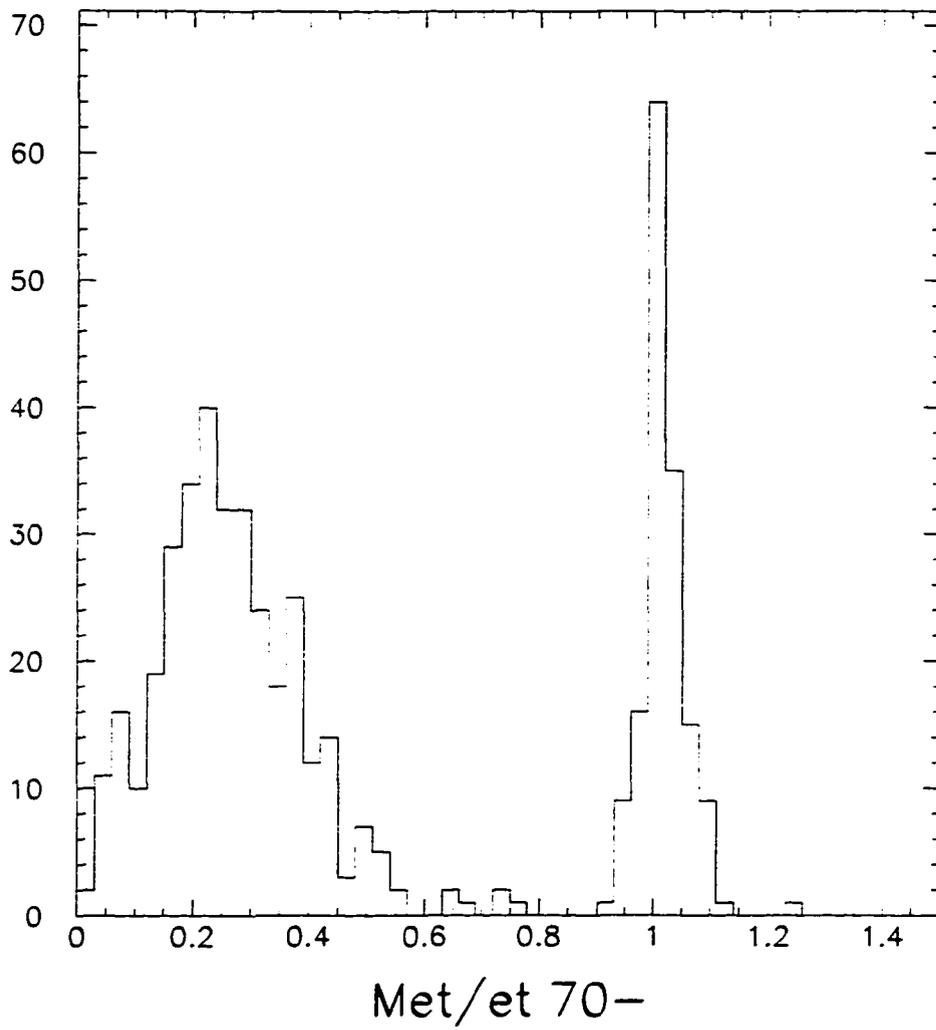
Figure 4.9: The missing E_T divided by photon E_T for photons above 70 GeV.
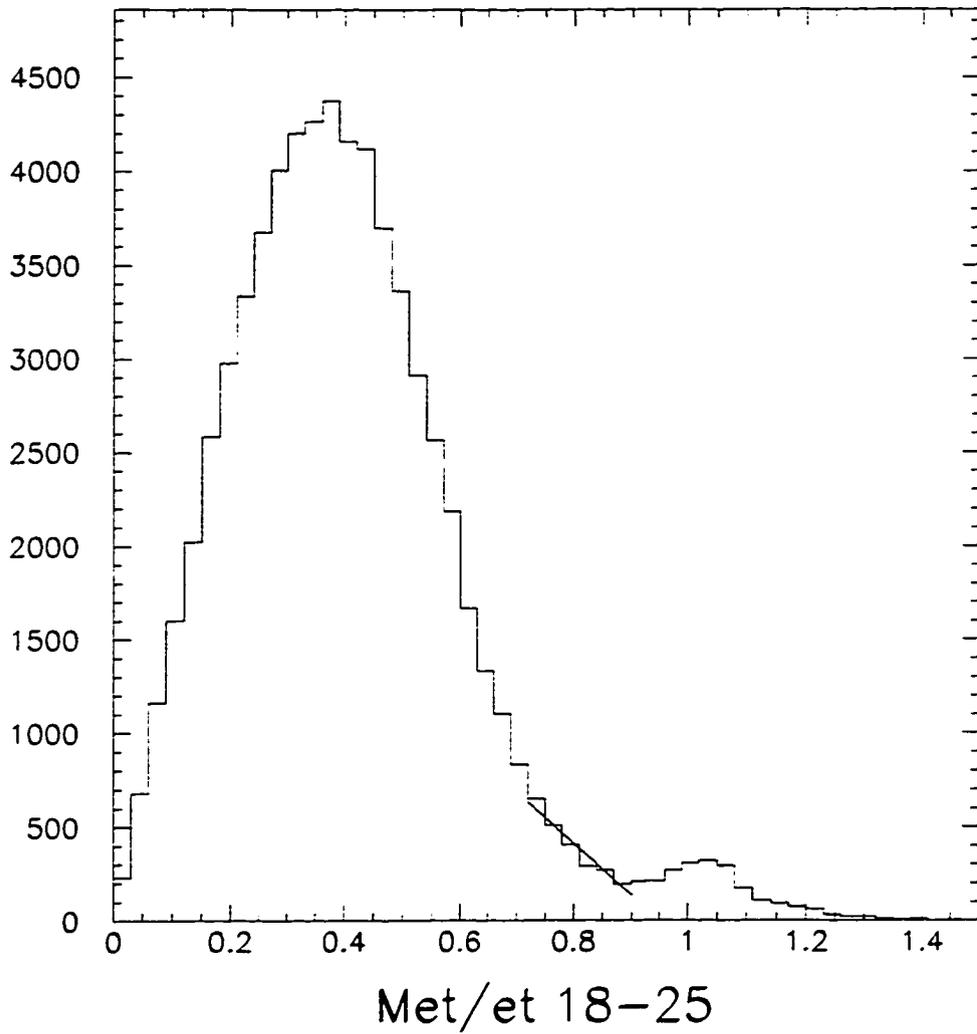
Figure 4.10: The missing E_T divided by photon E_T for photons from 18-25 GeV.

54
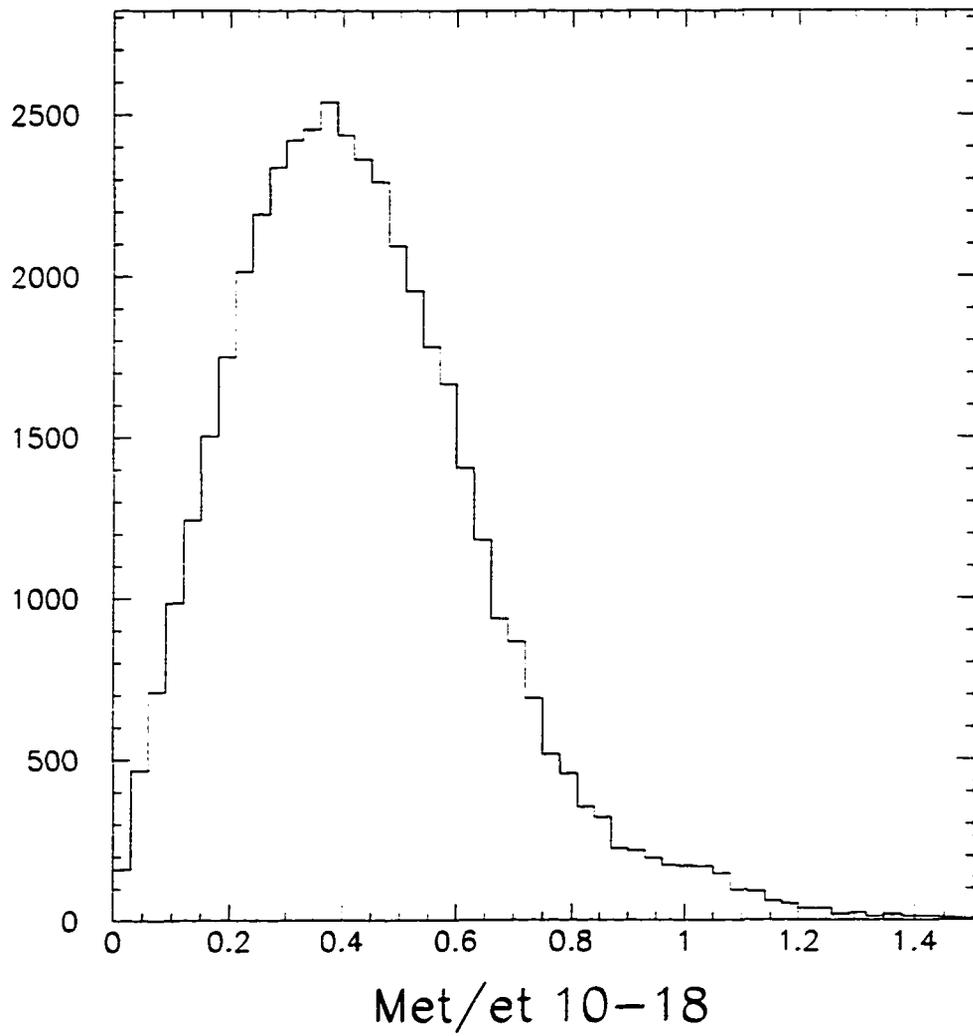
Figure 4.11: The missing E_T divided by photon E_T for photons from 10-18 GeV.

55
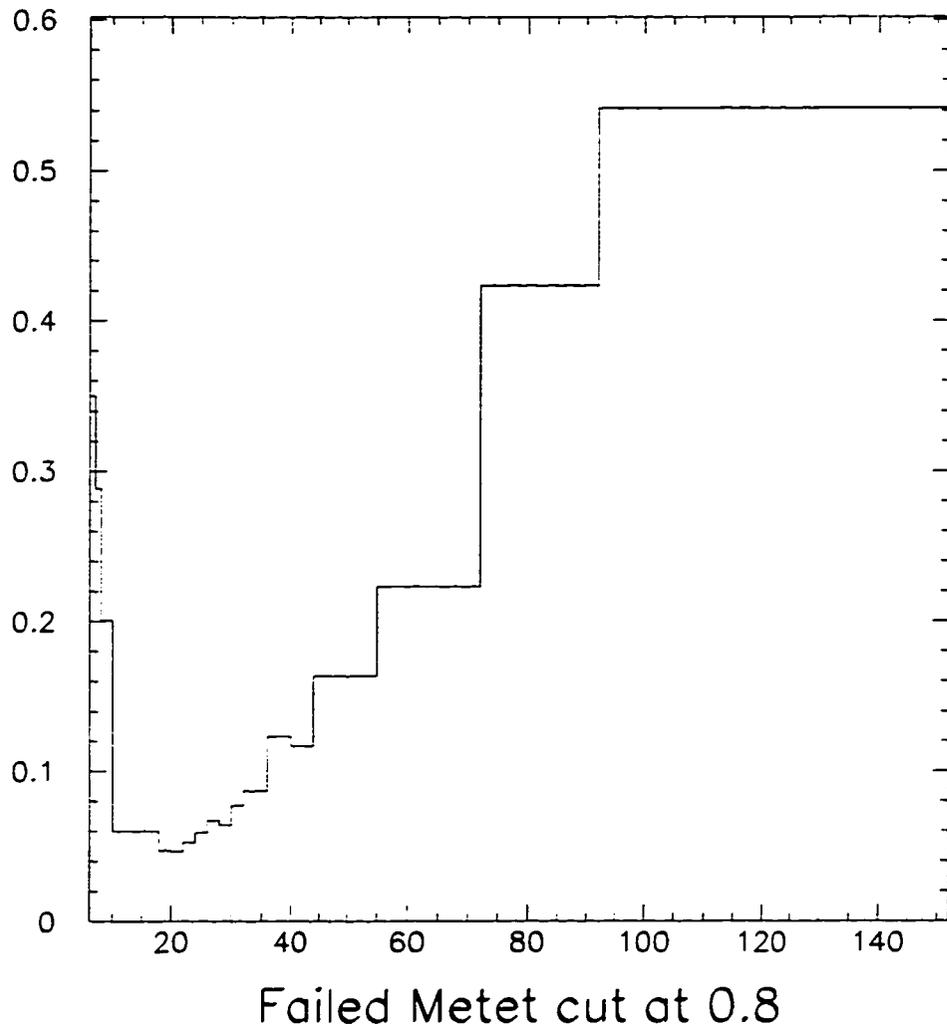
Figure 4.12: The fraction of events failing the missing E_T divided by photon E_T cut versus photon E_T.

56

The separation gets worse steadily for lower P_T photons, since the jet fluctuations increase, as shown in Fig. 4.10 for photons from 18 to 25 GeV. Clearly there is a tail of real photon events being lost above 0.8, and the figure shows our fitted extrapolation for this loss, which we use to correct the data. Below 18 GeV there is no longer clear separation between signal and background (Fig. 4.11), but the fraction of cosmic ray events is getting very small, since the spectrum of cosmic rays is not as steep as that of the direct photons (Fig. 4.12). The fraction of cosmic rays is dropping rapidly with decreasing energy into the few percent level at 10-15 GeV, and then it increases sharply because real direct photons start to be lost at an alarming rate due to jet fluctuations. Therefore, we only apply the cut above 18 GeV, and estimate from Fig. 4.12 that there is a 2.6% contamination of cosmic rays in the bin from 10-18 GeV, for which we correct the photon cross section downward.

We take as a systematic uncertainty 1/2 of the corrections mentioned above, which ranges from 0 at high P_T to 1.3% at 10-18 GeV.

4.8 Total acceptance

Finally, the total acceptance of prompt photons, including efficiencies for all applied cuts, is approximately 38% with a small P_T dependence. This is slightly smaller than the acceptance of prompt photons in the 1989 measurement [4] (46%) due to the effect of multiple collisions at the higher luminosities of the 1992-93 run.

Chapter 5

Statistical Background

Substraction

5.1 Background Separation Techniques

After applying standard photon cuts, the main background in the measurement of isolated direct photons is single isolated π^0 and η mesons, with smaller contributions from other multi-π^0 states.The dimensions of the detector and the shower sizes do not allow a particle by particle identification. To separate the prompt signal from background statistically, two independent techniques were used: *the profile method* and *the conversion method.*

In the profile method, we use the transverse profile of the electromagnetic shower in the CES and fit it to a standard electron profile, obtained from the test beam [23]. The χ^2, which is a measure of the goodness of the fit, is usually larger for a neutral meson (poor fit) than for a single photon (good fit), because a neutral meson produces on average wider electromagnetic showers.

58

In the conversion method we count electron-positron pairs from photon conversions which produce hits in the CPR. This method is based on the fact that the single photon conversion rate is lower than the conversion rate of two photons from π^0 or η decay.

Both methods rely on a cut, which has different efficiency for signal and background (given by ϵ_γ and ϵ_b). The efficiency of this cut (ϵ) is then measured in the data, and the number of signal events (N_γ) is determined from the formula

$$N_\gamma = \frac{(\epsilon - \epsilon_b)}{(\epsilon_\gamma - \epsilon_b)} N_{total} \tag{5.1}$$

where N_{total} is the total number of photon candidates in the sample.
Equation 5.1 comes from

$$\epsilon N_{total} = \epsilon_\gamma N_\gamma + \epsilon_b N_b \tag{5.2}$$

with $N_b = N_{total} - N_\gamma$.

The statistical uncertainty on N_γ is given by:

$$\sigma_{stat} = \sqrt{A^2((1 - \epsilon_\gamma)N_\gamma + (1 - \epsilon_b)N_b) + B^2(\epsilon_\gamma N_\gamma + \epsilon_b N_b)} \tag{5.3}$$

where

$$A = \frac{\epsilon_b}{(\epsilon_\gamma - \epsilon_b)}$$

and

$$B = \frac{(1 - \epsilon_b)}{(\epsilon_\gamma - \epsilon_b)}$$

5.2 The Profile Method

The prompt-photon events have a single isolated photon shower in the calorimeter. The background is composed of multiple photon showers with some

59
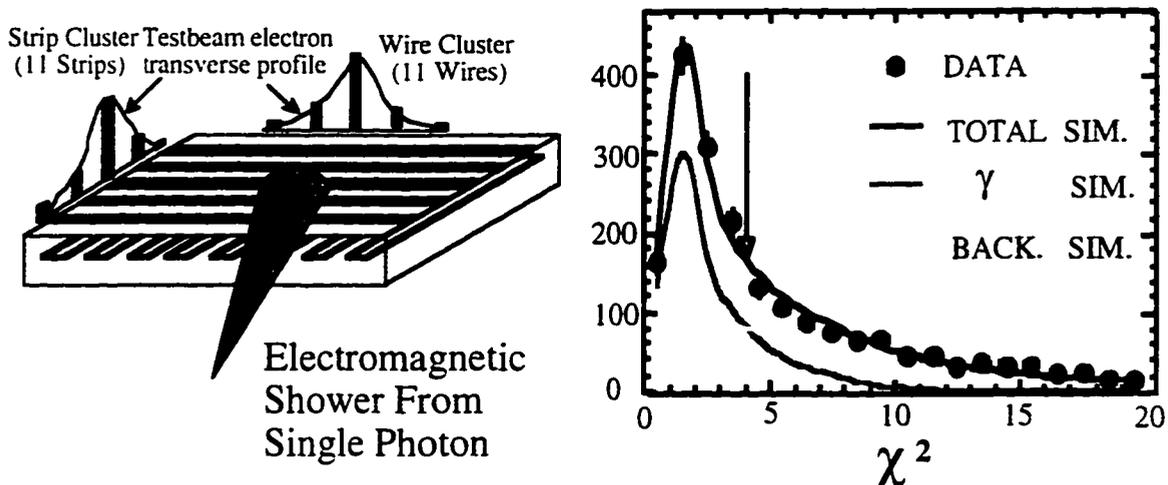
Figure 5.1: Schematical representation of the profile method.

spatial separation. The essence of the transverse shower profile method is to identify a class of the events whose measured profiles are unlikely to be produced by a single shower. For P_T values above 15 GeV/c it is not usually possible to resolve the individual showers from the two photons from π^0 decay. Therefore we use a statistical subtraction of the neutral meson background. For a large enough sample of events consisting of both single showers and π^0 induced showers we evaluate the fraction of π^0 events from the number of showers that are "too broad" to be consistent with a single electromagnetic shower. The number of π^0 showers that are indistinguishable from single photons can be inferred from the measured number of the "broad" showers using the characteristics of the π^0 decay and of the detector.

To measure the transverse profile of electromagnetic showers we use the central electromagnetic strip detector (chapter 3), which is positioned in the CEM at shower maximum ($\approx$ 6 radiation lengths). Fig. 5.1 illustrates the profile method. At first , a simple algorithm selects *seed* channels which have energy above 0.5 GeV and sums up the energy of a cluster around them containing 11 channels in both strip

60

and wire planes.We use an effective threshold of 40 ADC counts (57.2 MeV) for the inclusion of a channel energy in the energy sum of the cluster. Channels with energy below this threshold are set to zero. The transverse energy distribution in the cluster vs channel number is the transverse profile of the electromagnetic shower.

The expected electron transverse profile, which we use as a parent distribution for all fits, was obtained from the 1985 test beam data for 50 GeV electrons [23]. The strip and wire views of the standard profile depend differently on the position of the shower. The wire profile is independent of the X position of the shower and is symmetric about the shower center. Unlike the wire-view, the strip view has Z position dependence and, therefore, is not symmetric. This dependence has pure geometrical origin and comes from the "widening" of the shower by a factor $1/sin(\theta)$, when the electron is at angle θ. This "widening" can be removed by a change of coordinates

$$Z \rightarrow Z' = Z \sin(\theta)$$ (5.4)

Now, after determining the standard profile, we fit the transverse profile of the electromagnetic shower by the standard profile and calculate the χ^2 :

$$\chi^2 = \frac{1}{4} \sum_{i=1}^{11} \frac{[y_i - y(x_i)]^2}{\sigma_i^2}$$ (5.5)

where i is the cluster channel index, y_i is the measured profile (either strip or or wire) normalized to unity, $y(x_i)$ is the standard electron profile, and σ_i^2 is the estimated variance of the electron profile. After calculating the χ^2 for each CES plane, the final χ^2 of the fit is defined as the average:

$$\chi^2 = (\chi^2_{wire} + \chi^2_{strip})/2$$ (5.6)

Fig. 5.1 shows the χ^2 distributions for simulated signal and background showers. The

61

signal χ^2 distribution is significantly narrower.

The efficiency ϵ of the profile method is defined as the fraction of photon candidates with $\chi^2 < 4$. This efficiency can be measured for data and determined from simulation for direct photons and background. As we mentioned before, the multiple photon background contains mostly single isolated π^0 and η mesons with a small fraction of other multipion states. To simulate the background correctly, we need to know it's composition. The η/π^0 ratio was measured [24] by selecting two-photon events and reconstructing their invariant mass. The production rate after relative acceptance corrections was estimated to be $\eta/\pi^0 = 1.02$.

Fig. 5.2 presents the profile method efficiencies vs. photon P_T. The circles on the plot represent the 1992 data along with statistical errors; the squares represent the 1989 measurement. The curves are the efficiencies of the simulated signal and background. The data, which is a mixture of signal and background, has efficiencies lying between the simulated curves. Three points on the plot at $P_T < 10$ GeV are very close to the background curve because of very high background contribution at low P_T. These points are not used in our cross section measurement. Using the efficiencies in each bin for data simulated signal and background, we can calculate the fraction of prompt photon events from Eq. 5.1. As we will see in chapter 7, the systematic errors associated with the profile method are very large and therefore we use the profile method only for $10 < P_T < 16$ GeV. For $P_T > 16$ GeV we use the conversion method, which is discussed below.

62
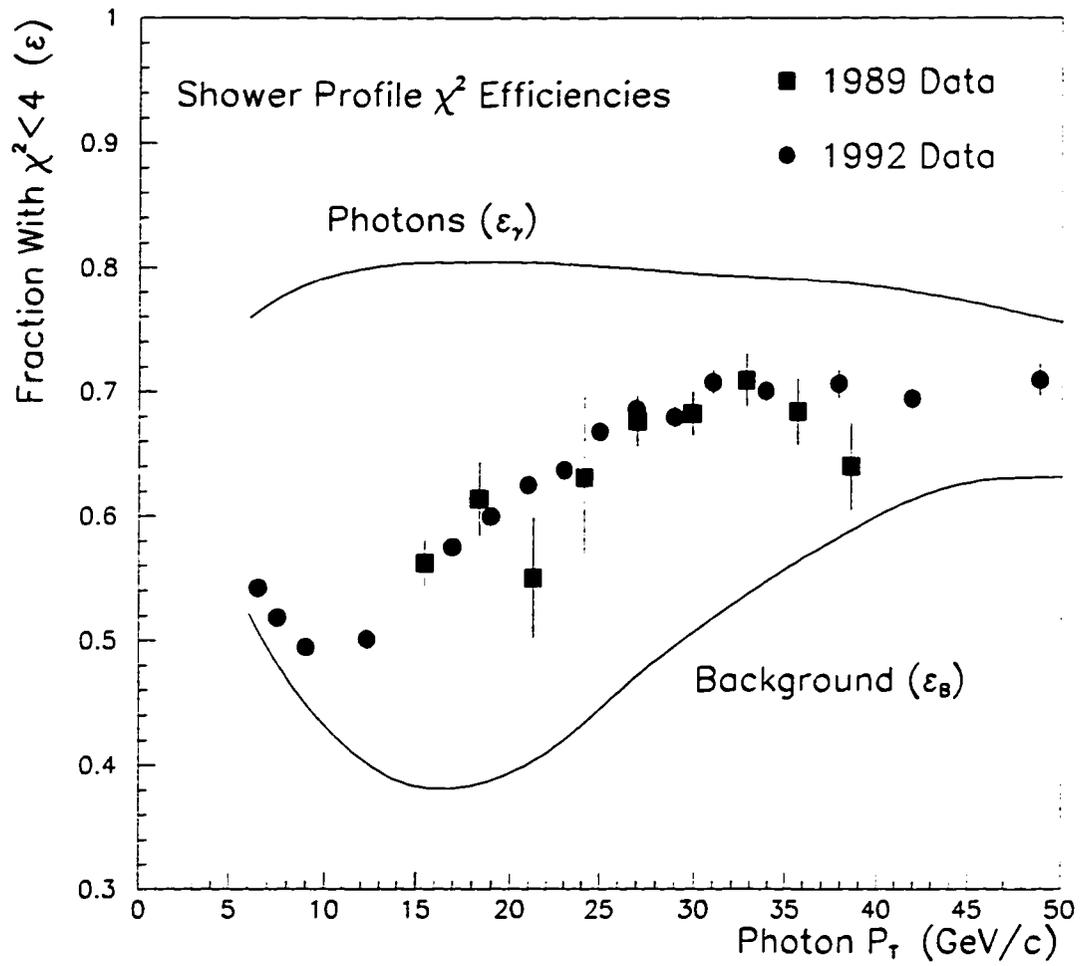
Figure 5.2: $\chi^2 < 4$ efficiency vs. P_T for data and for simulated signal and background.
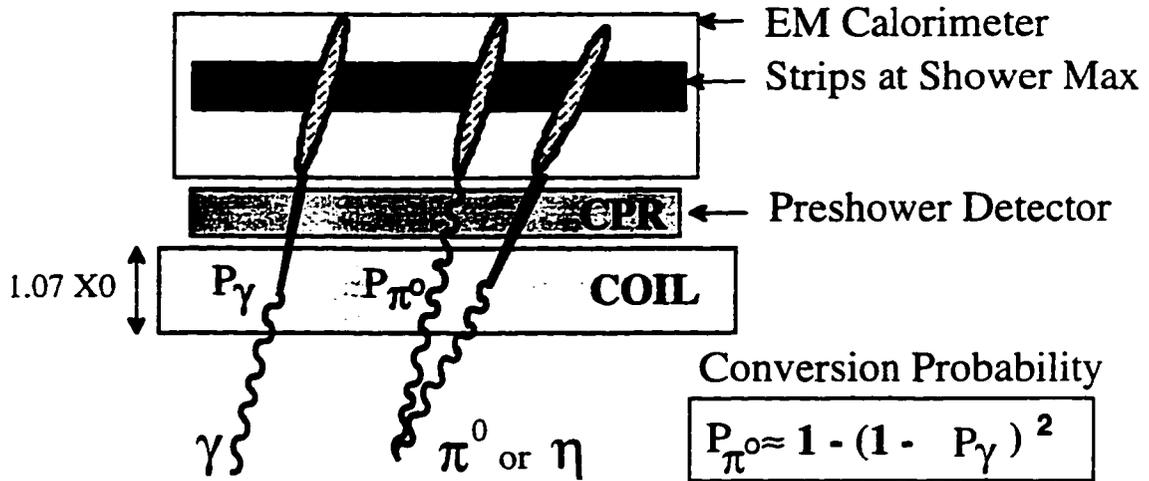
Figure 5.3: Schematical representation of the conversion method

5.3 The Conversion Method

The conversion method uses the fact that one of the two photons from a π^0 will convert in the coil material with higher probability than a single photon. The data (a combination of signal and background), will thus have a hit rate somewhere between these two values, and the algebra to determine the fraction of single photons from the data is given by Eq. 5.1. This is represented schematically in Fig. 5.3: direct and secondary photons pass the coil material, which has 1.07 radiation lengths, and some of them are detected in the CPR. Generally, the conversion probability for direct and secondary photons can be obtained from:

$$P_\gamma = 1 - e^{-\frac{7}{9}X_0}$$ (5.7)

and

$$P_{\pi^0} = 1 - (1 - P_\gamma)^2$$ (5.8)

but there is a number of corrections which have to be made and are discussed below.

For the conversion method, ϵ is the fraction of photon candidates which

64

produce a pulse height greater than that of a 1 minimum ionizing particle in the CPR within a 66 mrad "window" (5 CPR channels) around the photon direction. (For reference, the minimum separation of the photons from a 25 GeV/c π^0 is 11 mrad). The expected values of ϵ are derived from the equation:

$$\epsilon = 1 - EXP(-\frac{7}{9}X_0N_\gamma(P_T)\mathcal{P})$$ (5.9)

where X_0 is the amount of material in the solenoid coil, $\mathcal{P}$ is the photon pair production cross section, which has a slight energy dependence, and the term $N_\gamma(P_T)$ is the effective number of photons detected within the CPR "window". Clearly, for a single direct photon $N_\gamma(P_T) = 1$. For low energy π^0's and η's the separation between the two photons is large enough that only one photon is in the "window". We also consider the other multiphoton decays of the η and K_s. These are all displayed in Fig. 5.4, which shows the average number of detected photons in the "window" versus particle P_T. All decay modes come to a plateau at high P_T, which corresponds to the situation when all photons are within the window all the time.

To estimate the true photon pair production cross section $\mathcal{P}$, we reviewed theoretical calculations [25], GEANT [26], and EGS [27]. We have found that neither GEANT nor EGS reproduces the pair production cross section predicted by the review article [25] (reference in the particle data book). The EGS manual says that the cross section in [25] is more accurate, and the GEANT manual states that its cross sections are only good to 5% or so. Given this situation, we have modified the CDF simulation program, QFL, to use the exact cross section given by [25]. The difference between GEANT and [25] is shown in Fig. 5.5.

We also have done a careful accounting of the material in the solenoid magnet and find that it is 1.07 radiation length thick at 90^0, including the outer wall of the

65
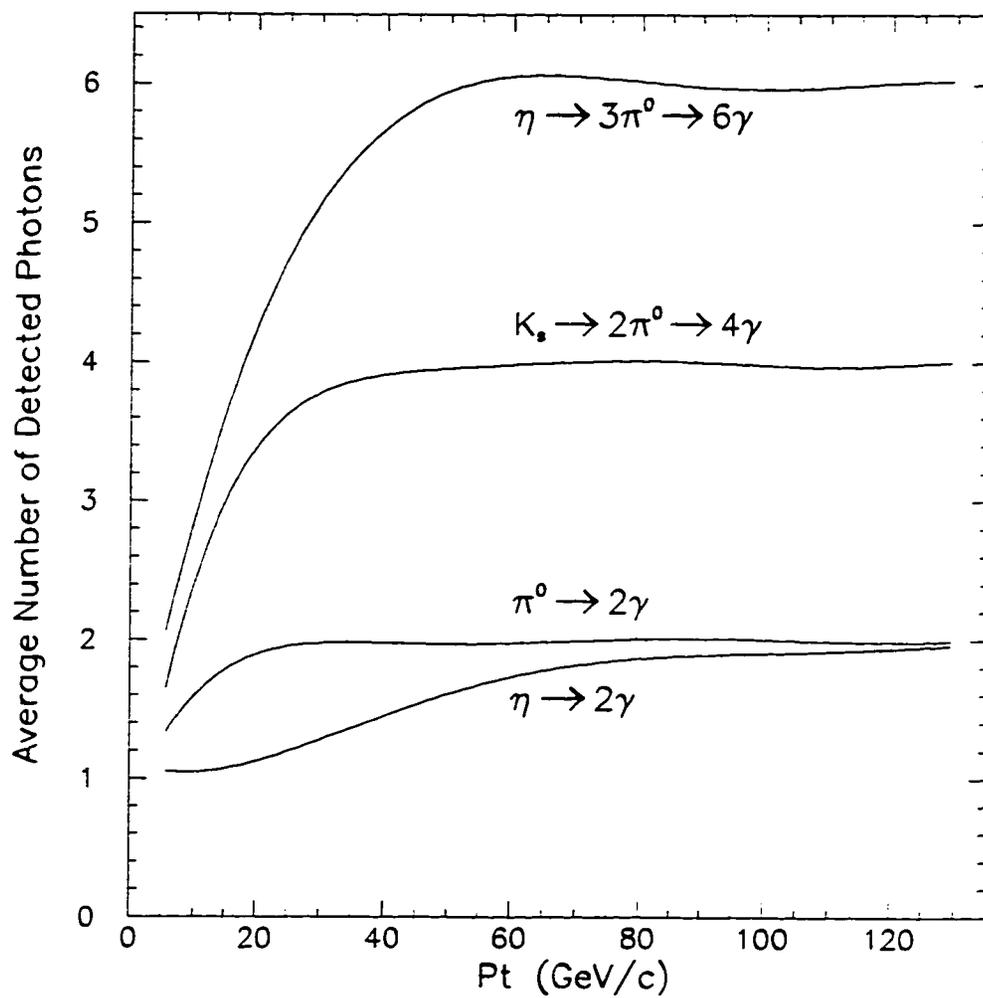
Figure 5.4: The average number of detected photons in the CPR for the different decay modes.

66
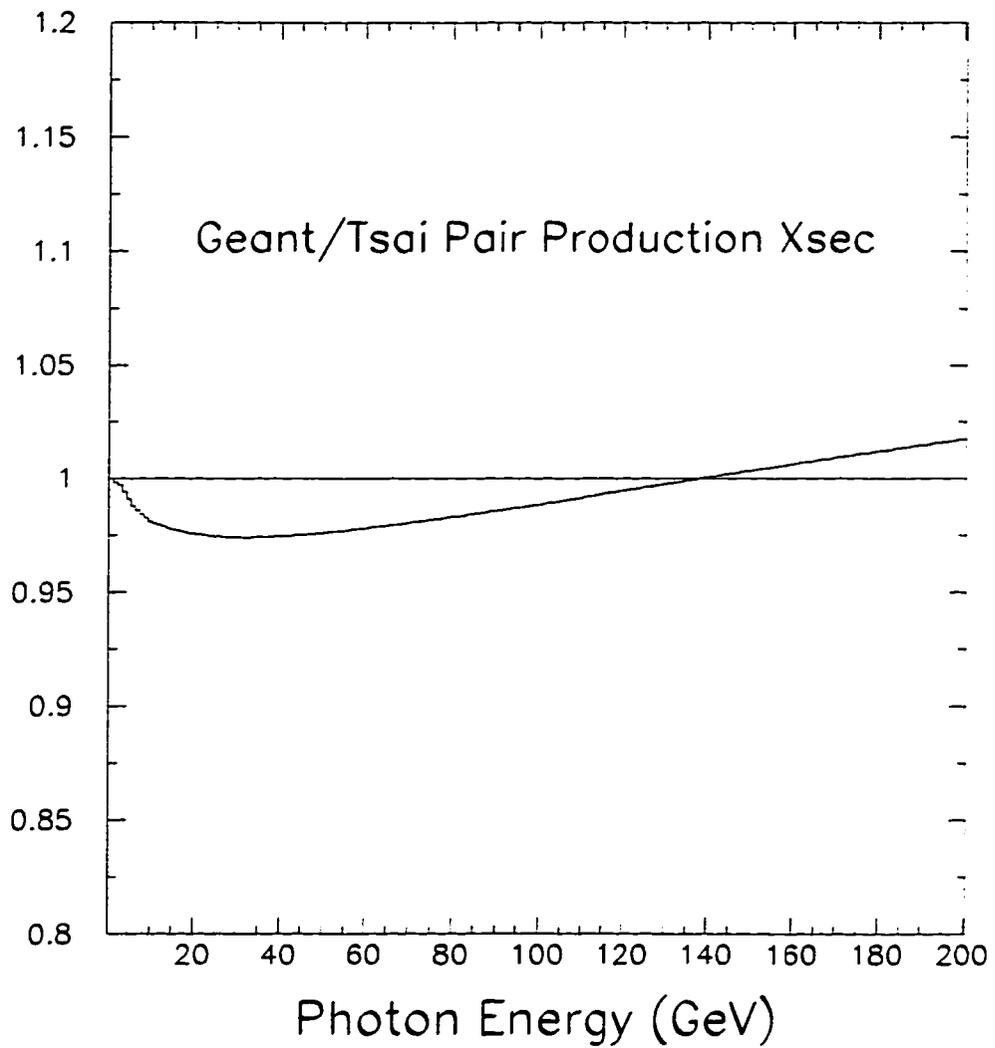
Figure 5.5: The Geant pair production cross section divided by the same from the theoretical calculations [25].

CTC and the CDT tubes. The complete chart of the material available for photon conversions at 90° is given in Tab. 7.1. We also made corrections for the angular increase of the amount of material at smaller angles.The angular dependence is shown in Fig. 5.6.

For low energy photons it is possible for part of the electromagnetic shower to travel at very large angles, almost backwards, with respect to the incoming photon. These photons can convert or Compton scatter and give a hit in the CPR. This effect is not included when considering the normal photon conversion in the solenoid material. Therefore we used GEANT to make an additional correction. Fig. 5.7 shows an example of a GEANT generated event in which a backscattered photon is producing a hit in the CPR.

Finally, we have to apply additional corrections due to CPR hits coming from underlying events and for dead CPR channels. We have measured the number of conversions in minimum bias events and find that there is a 3.75% chance of hit in a 5 channel window. From scanning these events it appears that hits come from soft (10-200 MeV) photons. The dead region in CPR amounts to 1.63%.

Figure 5.8 shows the measured efficiencies for the 1992 data along with efficiencies for signal and background which are obtained from simulation. Both simulated curves include all discussed corrections . The simulated photon curve does not have a P_T dependence, while the P_T dependence for background is weak for high P_T, when all secondary photons are within the CPR "window" and the approximation given by Eq. 5.7 is valid. For low P_T the ratio of signal to background in the data is less than 1/10.The first three data points are actually crossed by the background curve (Fig. 5.8). Therefore the conversion method cannot be used in the low P_T range (see chapter 6). At high P_T, by applying equation 5.1 we can calculate the number

68
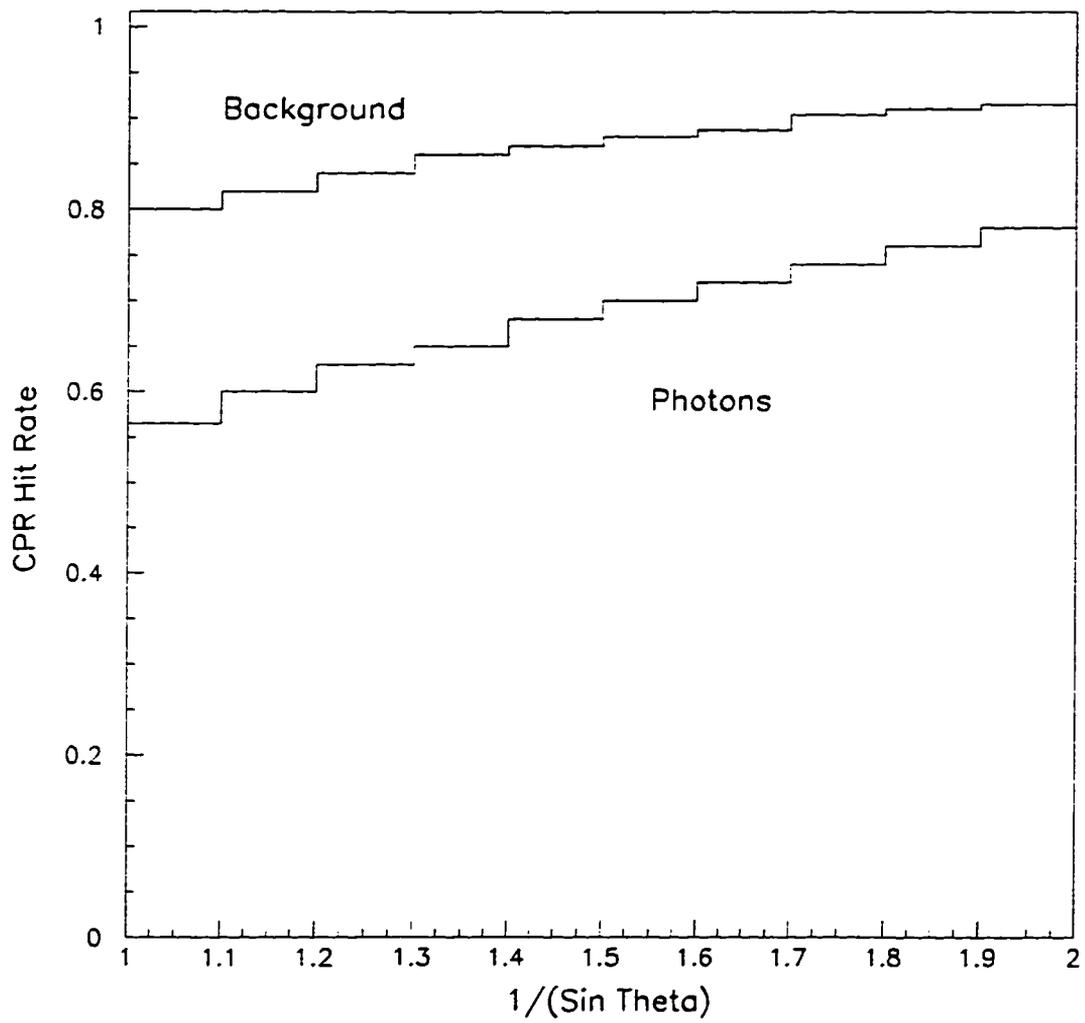
Figure 5.6: Hit rate efficiency angular dependence.

69
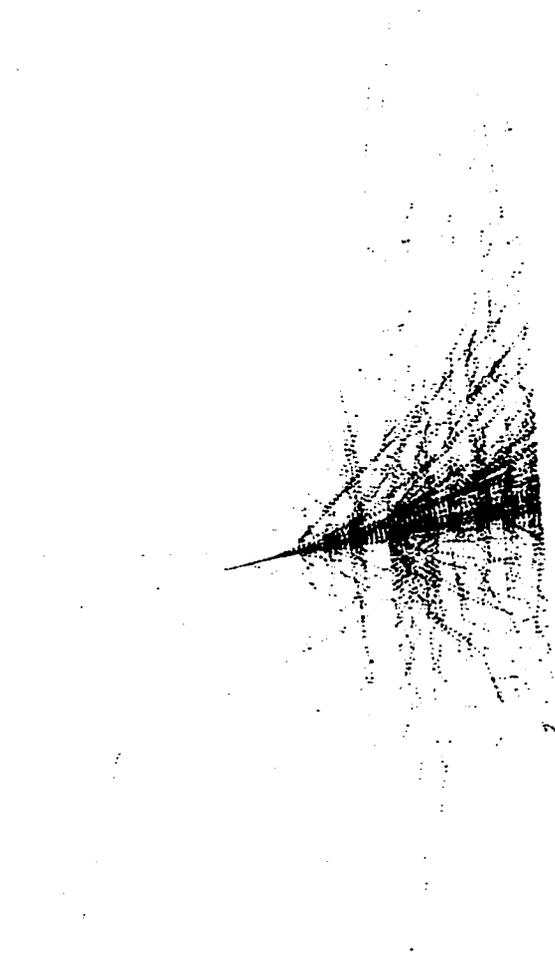
Figure 5.7: A single photon shower in Geant, with a backscattered photon giving a CPR hit. The photons are dashed and the electrons are solid.

70

of direct photons in each P_T bin.
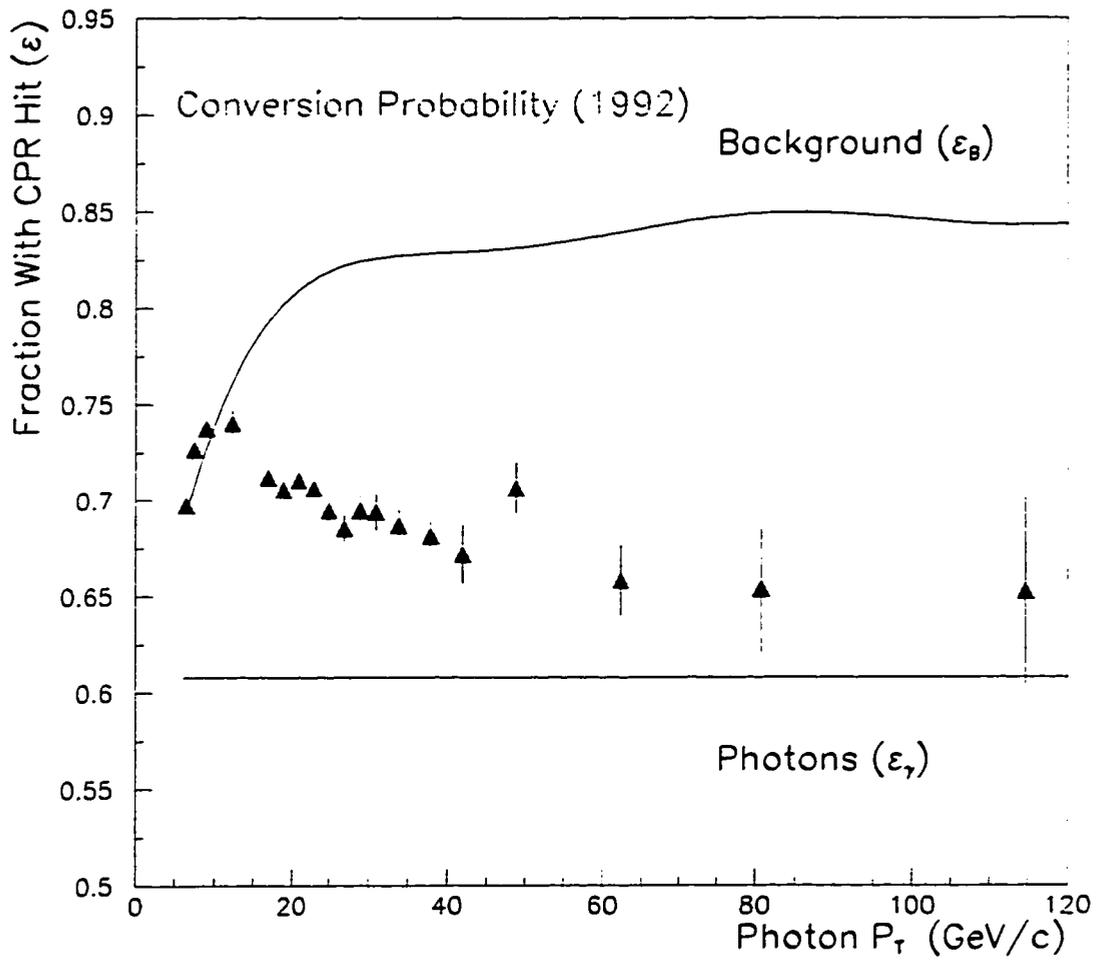
Figure 5.8: CPR hit rate efficiency vs. P_T for measured data and simulated signal and background.

Chapter 6

Direct Photon Cross Section

At this point, from the number of prompt photons (N_γ) in a bin of transverse momentum (ΔP_T) and a range of pseudorapidity $(\Delta \eta)$, along with the acceptance (a) for that bin and the integrated luminosity $(\mathcal{L})$, we can obtain the isolated prompt photon cross section:

$$\frac{d^2\sigma}{dP_T d\eta} = \frac{N_\gamma}{\Delta P_T \Delta \eta a \mathcal{L}} \tag{6.1}$$

The cross section is averaged over the pseudorapidity interval $|\eta| < 0.9$ ($\Delta \eta = 1.8$). As mentioned in chapter 4, the integrated luminosities for the 3 trigger thresholds of 50, 16, and 6 GeV are 19.74, 18.14, and 0.056 pb^{-1}, respectively, including the effect of prescales, and the total acceptance is approximately 38% with a small P_T dependence. The bin sizes were chosen to maintain sufficient statistics to perform background subtraction.

Direct photon cross sections, evaluated from Eq. 6.1 using the profile and conversion methods, are compared in Fig. 6.1. The plot shows that the agreement between the cross sections produced by the two background subtraction methods is

73

good to about 5%. The final direct photon cross section is a combination of the cross section obtained from the profile and conversion methods.

The conversion method has the advantage of a much smaller systematic uncertainties (chapter 7) and an unlimited P_T range. The profile method has the advantage of a better separation of signal and background than the conversion method in the low P_T region. The conversion method cannot be used in the low P_T region, because the ratio of the signal to background is 1/10 and the method becomes statistically weak. Thus, we use the profile method below $P_T = 16$ GeV and the conversion method above it. The final combined cross sections along with the number of events, number of photons after background subtraction, and statistical uncertainties are tabulated in table 6.1.

Figure 6.2 compares the final direct photon cross section with the published 1989 direct photon cross section measurement at CDF [4]. The agreement is good, although it is apparent that the first bin of the 1989 data is somewhat high.

Figure 6.3 shows the comparison between the data and the NLO QCD prediction [10] derived using CTEQ2M parton distributions [9] and the renormalization scale $\mu = P_T$. There is good qualitative agreement over many orders of magnitude between data and theory, although the data have a steeper slope than the calculations at low P_T. We will discuss this problem in chapter 8 after reviewing of the systematic uncertainties of the measurement.
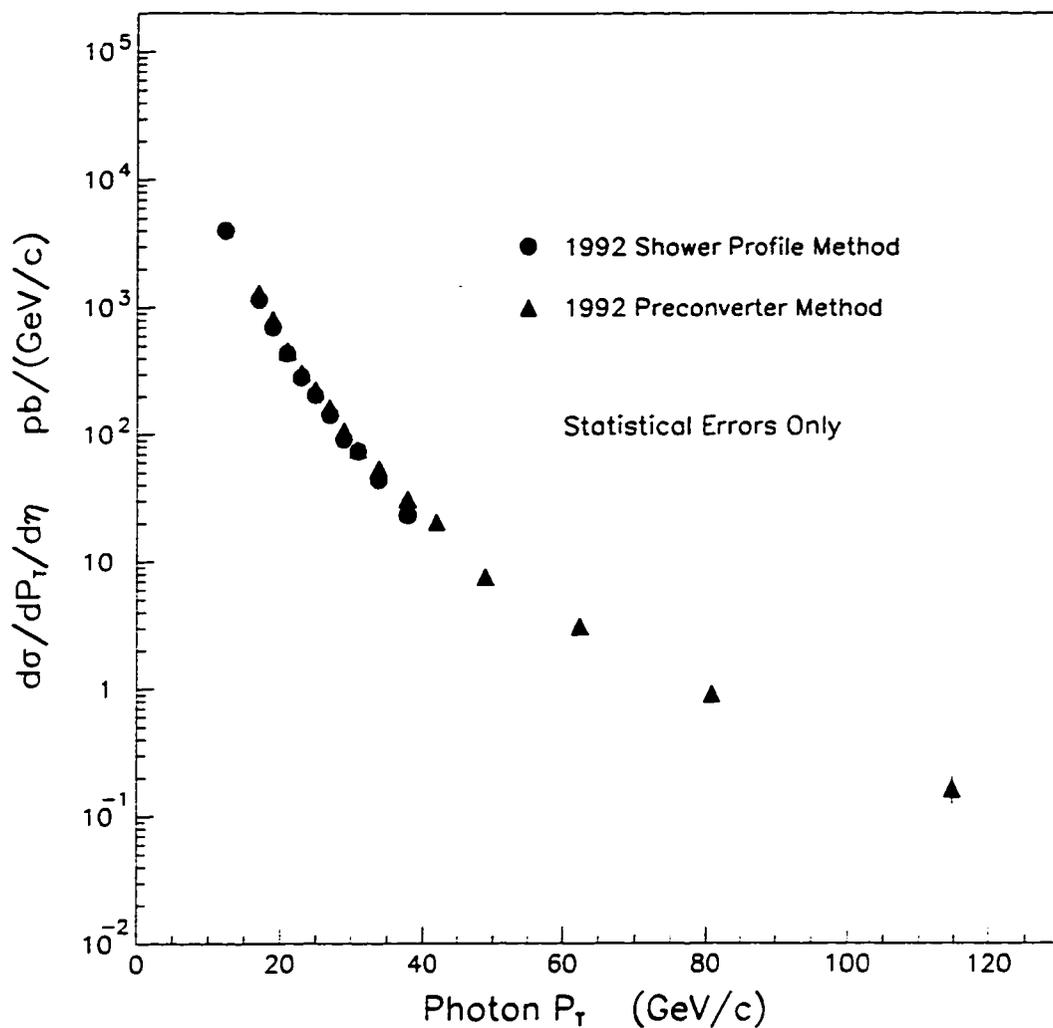
Figure 6.1: Comparison of direct photon cross sections using the profile and conversion background subtraction methods. The agreement between these cross sections is within 5%.

75

P_T Bin (GeV/c)	P_T (GeV/c)	# Events	# Photons	$d^2\sigma/dP_Td\eta$ (pb/(GeV/c))	Stat. Err. %
10-16	12.3	3982	897	4.46×10^3	9.3
16-18	17.0	30046	13943	1.30×10^3	2.9
18-20	19.0	28165	14675	8.05×10^2	2.6
20-22	21.0	17427	9064	4.58×10^2	3.3
22-24	23.0	10923	6033	3.08×10^2	3.8
24-26	25.0	7042	4362	2.26×10^2	4.3
26-28	27.0	4642	3118	1.63×10^2	4.9
28-30	29.0	3169	2012	1.06×10^2	6.1
30-32	31.0	2240	1433	7.67×10^1	7.2
32-36	33.9	2883	1974	5.37×10^1	6.0
36-40	37.9	1548	1110	3.09×10^1	7.9
40-44	41.9	942	722	2.05×10^1	9.5
44-55	48.9	1135	710	7.61×10^0	10.0
55-72	62.4	659	564	3.09×10^0	10.2
72-92	80.8	205	184	9.11×10^{-1}	17.4
92-152	114.7	95	90	1.63×10^{-1}	25.2

Table 6.1: Cross sections calculated using the profile and conversion methods are tabulated along with the statistical uncertainties.

76
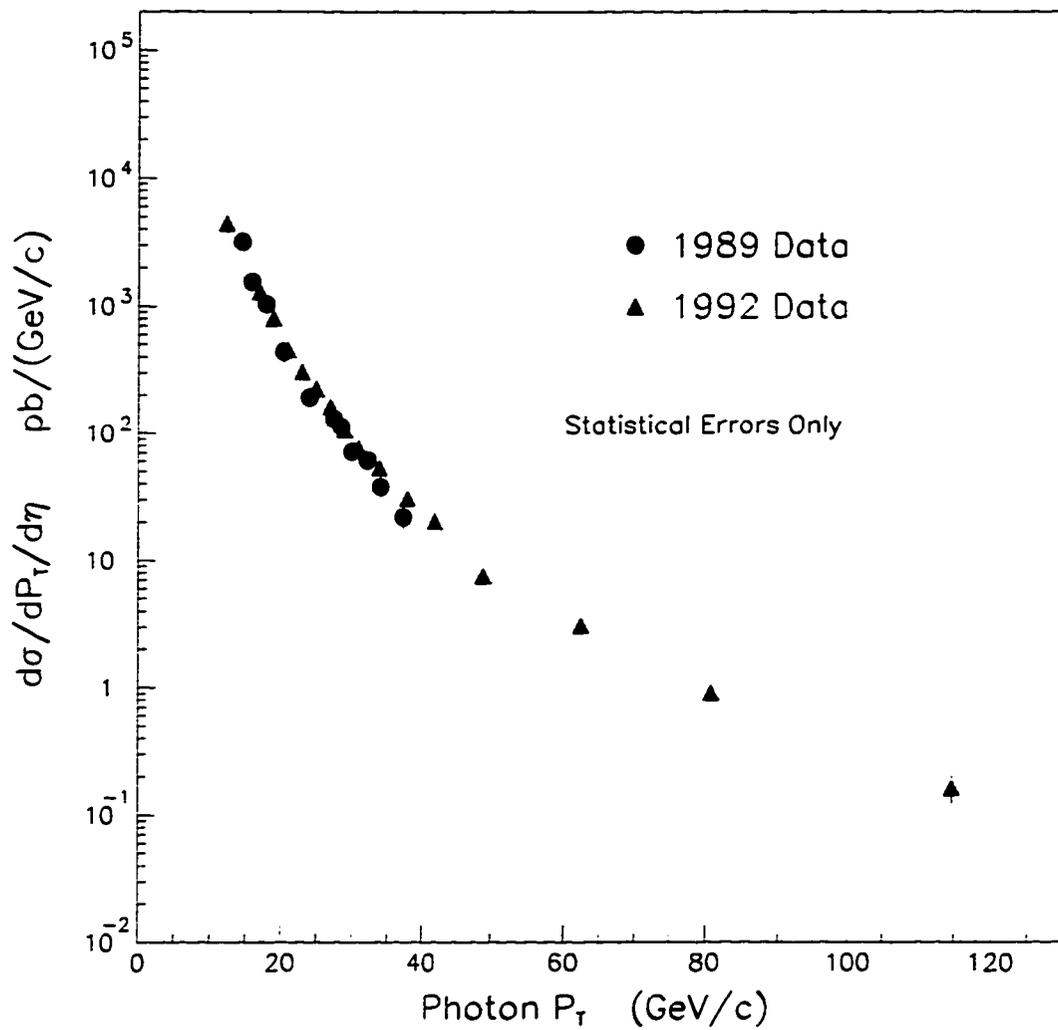
Figure 6.2: Comparison of direct photon cross sections with the 1989 results.

77
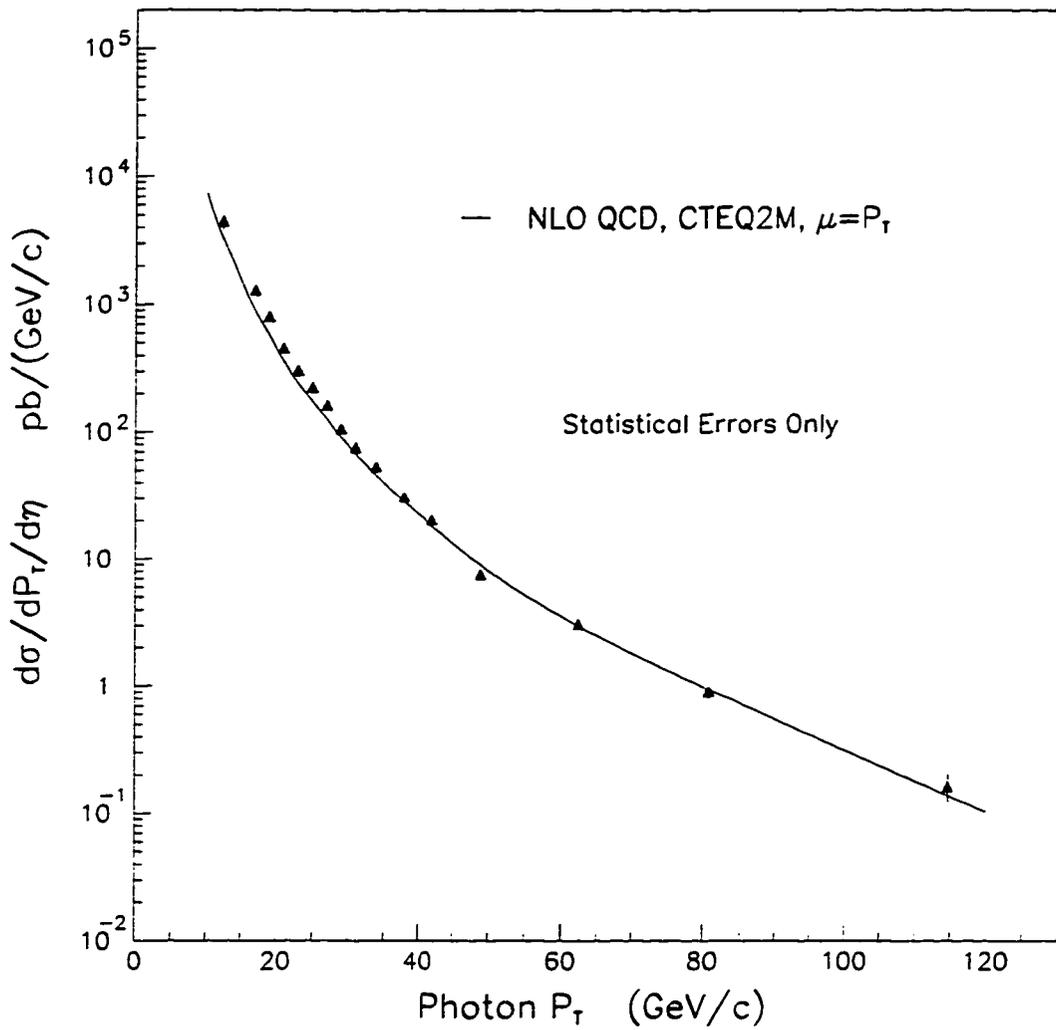
Figure 6.3: The direct photon cross section compared to the NLO QCD prediction. There is good qualitative agreement. However, the data have a steeper slope at low P_T.

78

Chapter 7

Systematic Uncertainties

7.1 Calibration of the CPR Conversion Probability

The systematic uncertainties in the prompt photon cross section measurement are dominated by the uncertainties in the background subtraction, which are due mostly to uncertainties in ϵ_γ and ϵ_b. For the conversion method, the precision of the ϵ_γ and ϵ_b is limited by the uncertainty of the amount of material in the front of the CPR. The expected amount of material along with the corresponding uncertainties is given in the Table 7.1, which shows that the amount of material is only known to within a few percent.

To estimate the conversion method uncertainty we reconstructed π^0, η and $\rho^\pm$ mesons decaying to photons and measured the CPR hit rate efficiency for these photons. We then compared the measured efficiency with that expected from a Monte Carlo simulation for the assumed amount of the material in Table 7.1. The disagreement between the measurement and simulation was used as a measure of the system-

Inner Radius (cm)	Description	Composition	Thickness (cm)	Radiation Lengths (X_0)	Uncertainty Estimate (X_0)
137.40	CTC Outer Wall	Al	0.793	0.0891	0.009
138.60	CDT	Fe	0.186	0.1057	0.011
142.90	Cryostat Wall	Al	0.700	0.0787	0.011
145.40	Inner Rad. Shield	Al	0.232	0.0261	0.003
148.10	Coil	Al	0.456	0.0512	0.005
148.56	Superconductor+Cu	NbTi+Cu	0.153	0.1071	0.005
148.71	Coil	Al	1.367	0.1536	0.002
150.08	Coil FRP	G10	0.280	0.0144	0.001
150.36	Coil	Al	1.600	0.1798	0.002
164.45	Outer Rad. Shield	Al	0.227	0.0255	0.003
164.70	Cryostat Wall	Al	2.000	0.2247	0.011
172.50	CPR Cover	G10	0.159	0.0082	0.001
172.66	G10 Cu Cladding	Cu	0.015	0.0107	0.001
			TOTAL	1.0748	0.023

Table 7.1: The amount of material available for photon conversions at 90 degree incidence.

80

atic uncertainty for ϵ_b. The systematic uncertainty for ϵ_γ can be easily calculated from the systematic uncertainty of ϵ_b, because of the complete correlation between these uncertainties.

We will start the description of this analysis with the reconstruction of the π^0, η and $\rho^\pm$ meson peaks. The reconstruction of π^0 and η mesons decaying to two photons [28] was performed using the events of the 6 GeV level 3 trigger and the invariant mass formula :

$$M^2 = 2E_1 E_2(1 - \cos\theta_{12}) \tag{7.1}$$

where E_1 and E_2 are the photon energies and θ_{12} is the angle between the two photons in the laboratory frame. The $\cos\theta_{12}$ can be expressed in terms of the CES X and Z coordinates:

$$\cos\theta_{12} = \frac{R^2 + Z_1 Z_2 + X_1 X_2}{\sqrt{(R^2 + Z_1^2 + X_1^2)(R^2 + Z_1^2 + X_2^2)}} \tag{7.2}$$

Using $|CESx| < 17.5$ cm and $|CESz| < 217$ cm fiducial cuts, the π^0 and η peaks are clearly seen (Fig. 7.1).

The main background to π^0 and η mesons are the single photon showers which have fluctuated to produce the second CES strip cluster in an adjacent tower. To reject single photon showers an energy *asymmetry cut* was used. The two photon energy asymmetry is defined as:

$$Asymmetry = \frac{|E_1 - E_2|}{E_1 + E_2} \tag{7.3}$$

where E_1 and E_2 are the energies of the two photons in the CEM. Fig. 7.1 shows the affect on the mass distribution of a cut on the asymmetry at *Asymmetry* < 0.75 and at *Asymmetry* < 0.5. We used the 0.75 cut for η mesons, which has two well separated photons and the contribution of single photon showers is not so significant,

81

Affect of 2γ Energy Asymmetry Cut
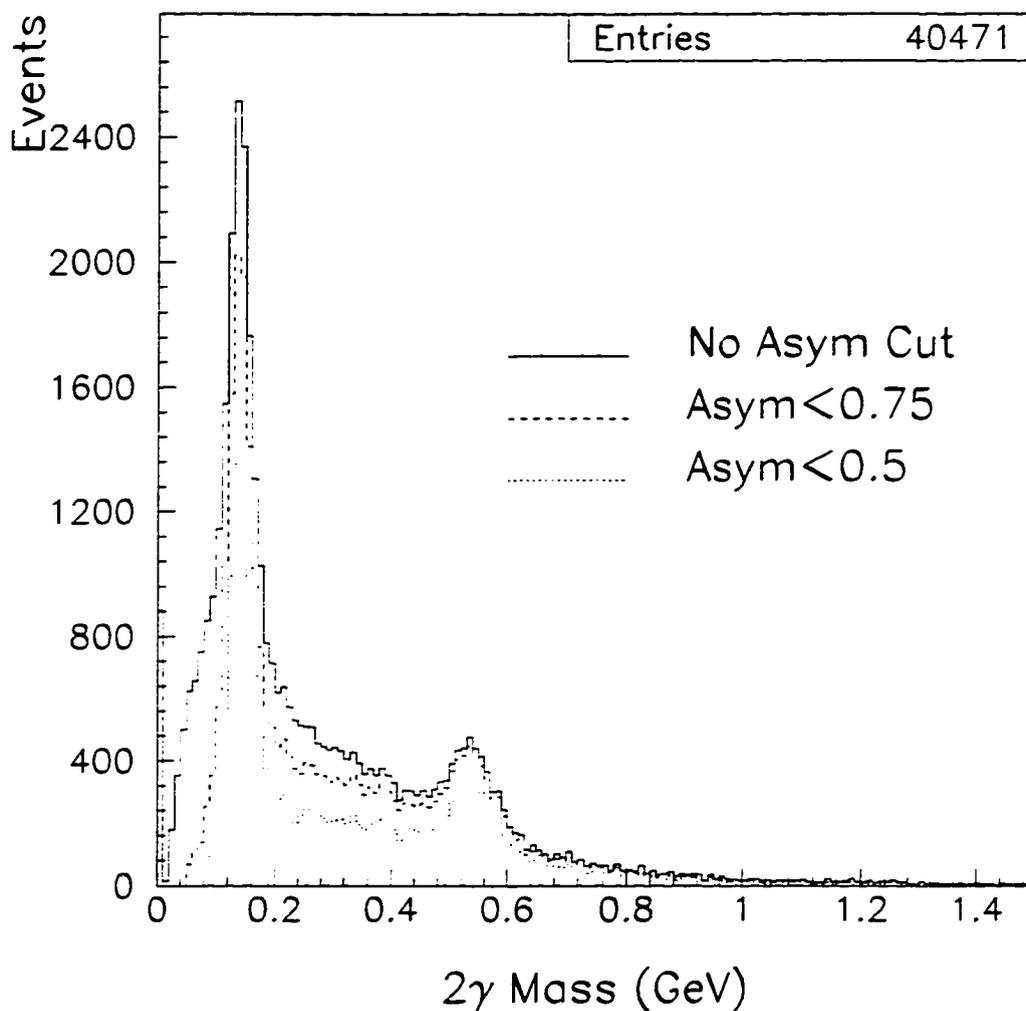
Figure 7.1: The two photon invariant mass distribution without photon asymmetry $|E_1 - E_2|/(E_1 + E_2)$ cut (solid line), requiring asymmetry < 0.75 (dashed line), and with asymmetry < 0.5 (dotted line).

82

and the 0.5 cut for π^0 mesons to eliminate the single photon background as much as possible.

To select $\rho^{\pm}$ mesons decaying to $\pi^0 \pi^{\pm}$ [29] we looked for events with a single charged track in association with an electromagnetic shower. As π^0 candidates we used electromagnetic clusters from the ELES bank (isolated 16 GeV level 3 trigger) which passed standard single photon cuts, and as $\pi^{\pm}$ candidates we used charged tracks from the TRKS bank which passed track quality cuts . The invariant mass for all such combinations was reconstructed. To separate $\rho^{\pm}$ events from a combinatorial background two additional cuts were used:

1) The charged track was required to have $P_T > 1.1$ GeV/c. After applying this cut a $\rho^{\pm}$ peak is observed (Fig. 7.2 (b)) .

To suppress the background further and make the $\rho^{\pm}$ sample cleaner we also required

2) $\cos \theta^* < -0.88$, where $\cos \theta^*$ is an angle between the $\pi^{\pm}$ direction in the $\pi^{\pm} \pi^0$ CMS frame and the $\pi^{\pm} \pi^0$ direction in the lab frame. The requirement of small $\cos \theta^*$ selects the combinations of energetic π^0's and low-energy $\pi^{\pm}$ and therefore optimizes the resolution of electromagnetic clusters in the calorimeter and of charged tracks in the tracking chambers. Fig. 7.2 (d) demonstrates this statement by comparing $\rho^{\pm}$ invariant mass distributions obtained from Monte Carlo simulation using a $\cos \theta^* < -0.88$ cut (solid line) and a $\cos \theta^* > -0.88$ cut (dashed line). The peak of simulated events which passes the $\cos \theta^* < -0.88$ cut is significantly sharper.

The final reconstructed mass distributions in the π^0, η, and $\rho^{\pm}$ regions are shown in Figs. 7.3, 7.4, and 7.5 respectively. We used a Gaussian signal and cubic background to fit the π^0 distribution, a Gaussian signal and linear background for the η meson, and a Breit-Wigner signal and quadratic background for the $\rho^{\pm}$ meson. In all the plots the solid curve shows how the signal plus background fits the data

83
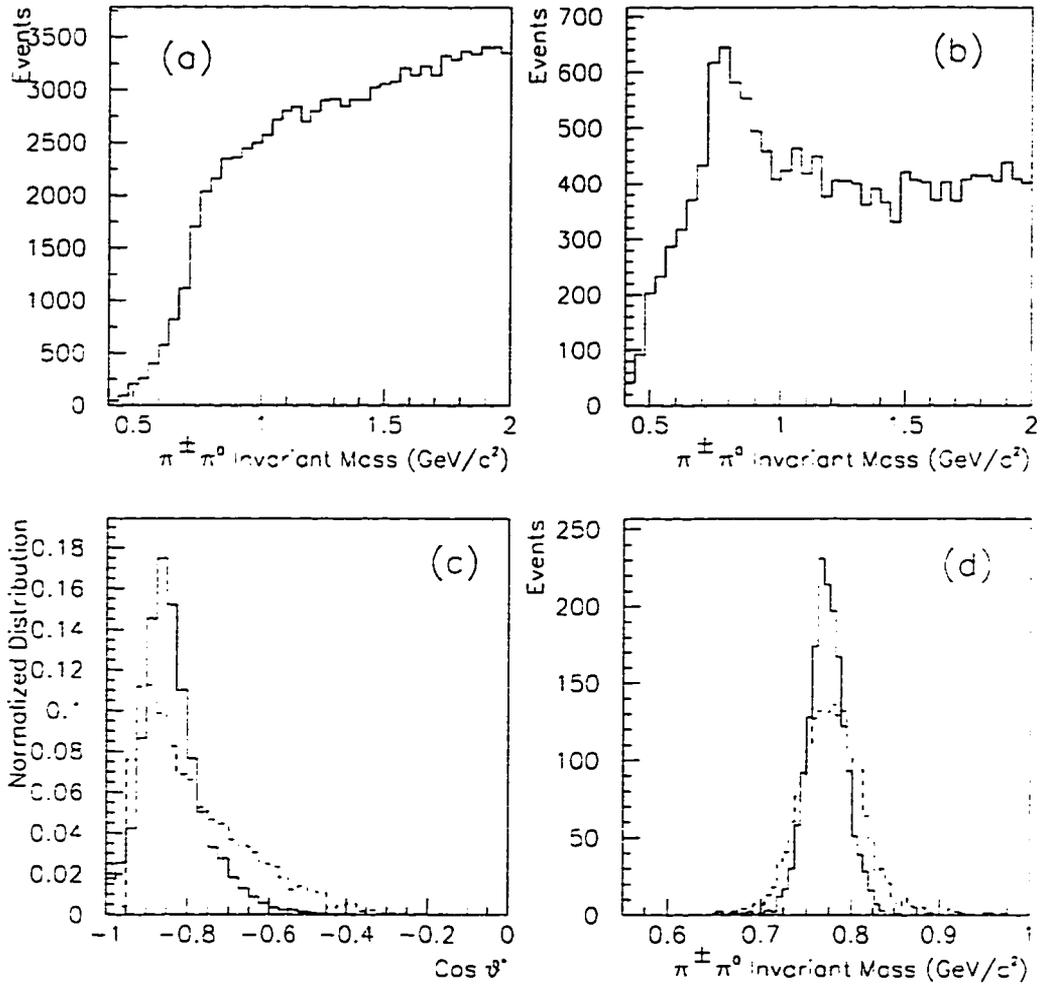
Figure 7.2: (a) $\pi^{\pm}\pi^0$ invariant mass distribution (b) Mass distribution for the events that passed the $P_T(\pi^{\pm}) > 1.2 GeV/c$ cut (c) Comparison of the measured $\cos\theta^*$ distribution (solid line) with the same distribution from a Monte Carlo simulation (dashed line) (d) Mass distribution of Monte Carlo $\rho^{\pm}$ events with $\cos\theta^* < -0.88$ (solid line) compared to the events with $\cos\theta^* > -0.88$ (dashed line).

84

Gaussian π^0 and Polynomial Background Fit

Entries	8094
χ^2	1.101
P1	892.5
P2	0.1394
P3	0.1647E−01
P4	66.63
P5	−3751.
P6	0.6009E+05
P7	−0.1820E+06
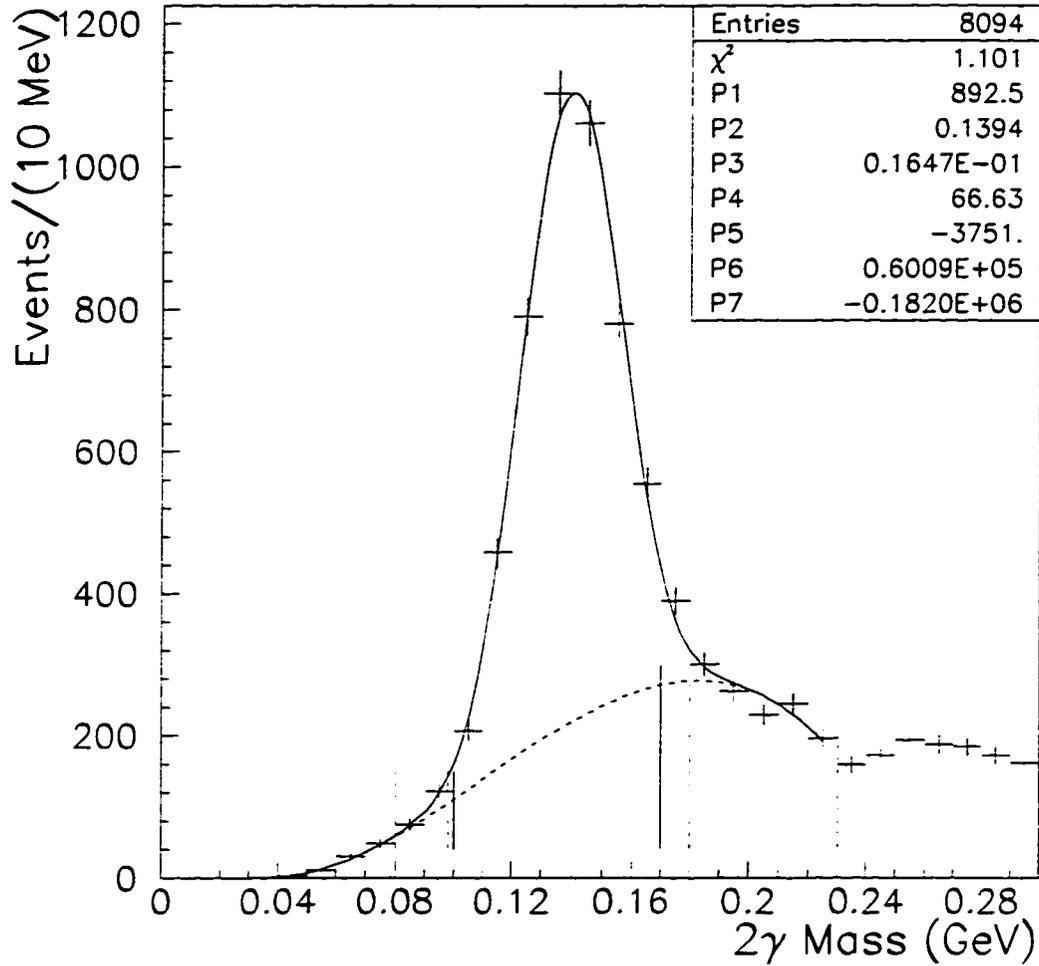
Figure 7.3: The measured two photon mass distribution in the region of the π^0 meson and a fit (solid curve) to a Gaussian peak and cubic background (dashed curve). The "peak region" is within the solid vertical lines and the "sideband regions" are within the vertical dashed lines.

85

and the dashed curve corresponds to the background. (Fig. 7.5 also shows the Breit-Wigner signal in the $\rho^\pm$ region using dotted curve). The mean measured masses are in reasonable agreement with the particle data group (PDG) [30] values: 0.139 GeV (measured) and 0.135 GeV (PDG) for π^0, 0.538 GeV (measured) and 0.547 GeV (PDG) for η, and 0.780 GeV (measured) and 0.768 GeV (PDG) for $\rho^\pm$.

After reconstructing the meson peaks we divided the invariant mass distributions into two regions: the peak region, mostly dominated by the signal, and the sideband region, dominated by background. The vertical solid lines in the plots define the signal region : 0.10 GeV < M < 0.17 GeV for π^0, 0.65 GeV < M < 0.75 GeV for η, and 0.56 GeV < M < 0.9 GeV for $\rho^\pm$. The sideband regions are defined by the vertical dashed lines: 0.08 GeV < M < 0.10 GeV and 0.18 GeV < M < 0.23 GeV for π^0, 0.35 GeV < M < 0.45 GeV and 0.65 GeV < M < 0.75 GeV for η, and 0.95 GeV < M < 1.95 GeV for $\rho^\pm$.

Now we can measure the hit rate efficiency in the CPR for events from the peak and sideband regions. The fractions of events with a CPR hit vs. invariant mass for π^0, η, and $\rho^\pm$ decays are shown in Figs. 7.6, 7.7, and 7.8 respectively. Again, the solid and dashed vertical lines separate the peak and background regions. Using the signal and background fitting functions we can calculate the number of signal N_{signal} and background N_{back} events in the peak region. After that, the neutral meson hit rate efficiency can be calculated from the sideband subtraction formula :

$$\epsilon_{neut.meson} = \epsilon_{peak} + (\epsilon_{peak} - \epsilon_{back})\frac{N_{back}}{N_{signal}} \tag{7.4}$$

where ϵ_{peak} and ϵ_{back} are the measured hit rate efficiencies in the peak and sideband regions respectively. The statistical error for the hit rate efficiency can be calculated

86

Gaussian η and linear Background Fit

Entries	11173
χ^2	1.351
P1	246.0
P2	0.5383
P3	0.3422E-01
P4	538.9
P5	-658.4
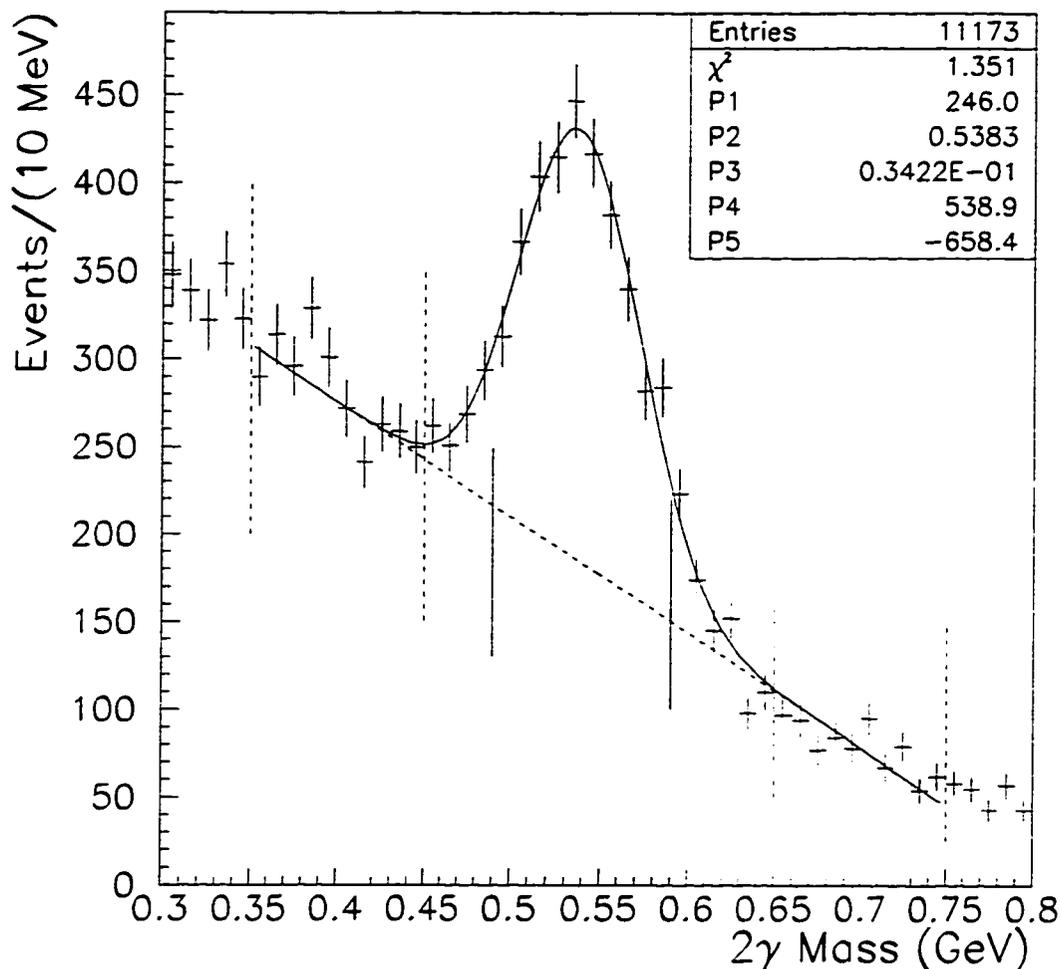
Figure 7.4: The measured two photon mass distribution in the region of the η meson and a fit (solid curve) consisting of a Gaussian peak and linear background (dashed curve). The "peak region" is within the solid vertical lines and the "sideband regions" are within the vertical dashed lines.

Entries		8238
χ^2/ndf	170.0	/ 37
P1		28.38
P2		0.7426
P3		0.3143
P4		−121.1
P5		345.5
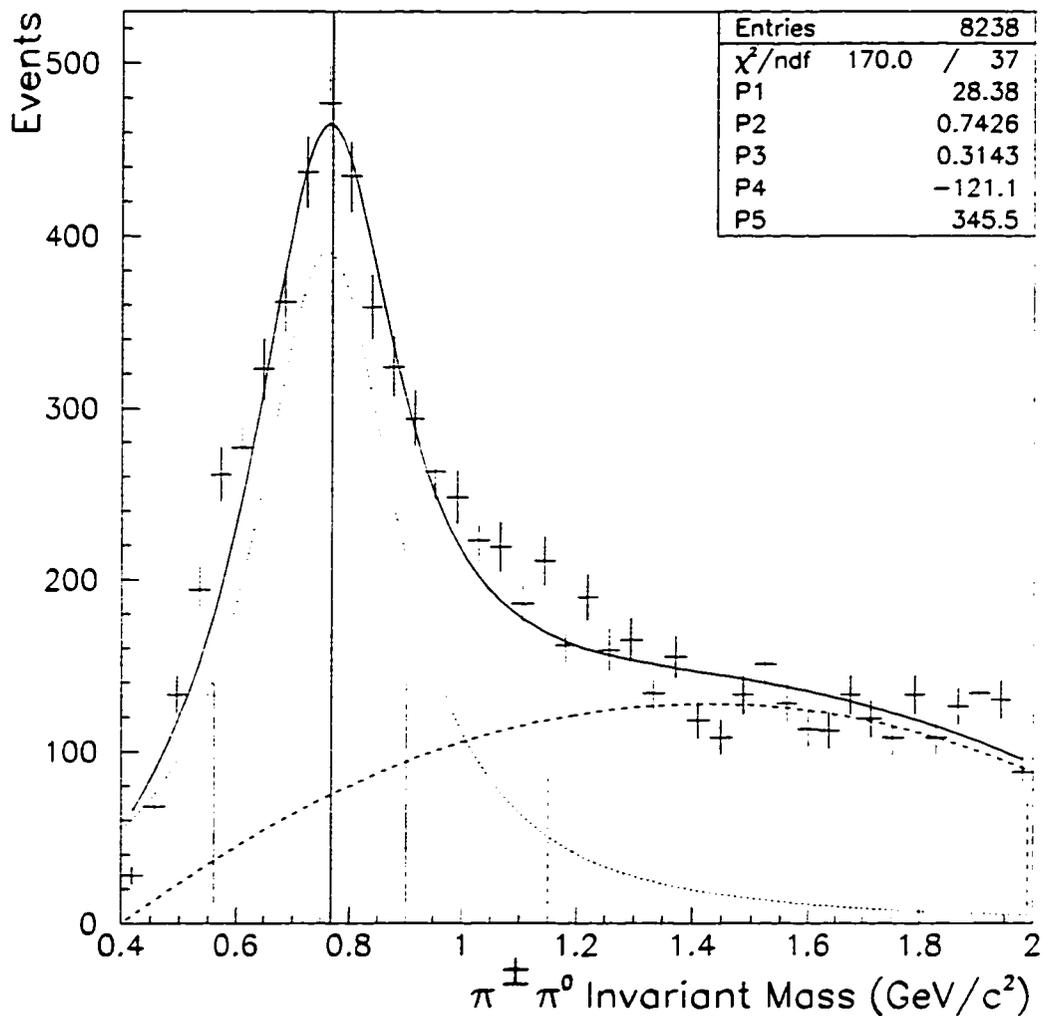
Figure 7.5: The measured $\pi^{\pm}\pi^0$ mass distribution in the region of $\rho^{\pm}$ meson and a fit (solid curve).The fit is the sum of a Breit-Wigner peak (dotted curve) and a quadratic background (dashed curve). The signal region is within the solid vertical lines and the sideband region is within the vertical dashed lines.

88

by using the following formula:

$$\sigma^2_{neut.meson} = (1 + \frac{N_{back}}{N_\rho})^2 \sigma^2_{peak} + (\frac{N_{back}}{N_\rho})^2 \sigma^2_{back} \tag{7.5}$$

To estimate the systematic error of the CPR hit rate efficiency measurement we varied the selection cuts and widths of the signal and background regions. Finally, the measured CPR hit rate efficiency for π^0's, η's, and π^0's from $\rho^\pm$ decays are: $P_\pi = 0.842 \pm 0.008$, $P_\eta = 0.831 \pm 0.012$, and $P_\rho = 0.836 \pm 0.01$.

The expected conversion rates of π^0, η, and $\rho^\pm$ can be obtained from Monte Carlo simulation using the amount of material from Table 7.1. To compare the expected hit rate efficiencies with measured ones, we need to apply additional corrections. First, we have to apply a correction for events which have a CPR hit due to the underlying event. The total probability of getting a CPR hit from the underlying event is 7% (obtained from minimum bias approximation for the underlying event). We also have to take into the account the 1.63% dead region correction for the CPR . After applying these corrections, the expected hit rate efficiencies are: $P_{EXP,\pi} = 0.847 \pm 0.006$, $P_{EXP,\eta} = 0.842 \pm 0.006$, and $P_{EXP,\rho} = 0.834 \pm 0.004$.

Table 7.2 shows how good is the agreement between the measured and predicted rates in all three cases. We also compared the measured and expected hit rate efficiencies for different angles (which translates to different amount of material) and different photon energies (by changing the effective number of photons in the CPR "window"). For all combinations the agreement was good. Therefore we use 0.006 for the uncertainty in ϵ_b. This translates into the 0.0078 uncertainty in ϵ_γ, and is completely correlated with the ϵ_b uncertainty. Finally, these uncertainties give 7% systematic error for the conversion method in the cross section measurement at 16 GeV/c P_T, and 4.5% at 100 GeV/c.

89

Figure 7.6: The measured CPR hit rate efficiency in the region of the π^0 meson. The signal region is within the solid vertical lines and the sideband regions are within the vertical dashed lines. The horizontal dashed line is the mean efficiency for background.

90

CPR Hit Efficiency vs. Mass

Fraction of Events with CPR Hit

Efficiency in η Region $\varepsilon_{PEAK} = 0.866 \pm .006$

Bgrd. Eff. (Sidebands) $\varepsilon_{BACK} = 0.901 \pm .005$

Efficiency for η $\varepsilon_{\eta} = 0.831 \pm .012$

Expected η Efficiency $\varepsilon_{EXP} = 0.842 \pm .006$

2γ Mass (GeV)
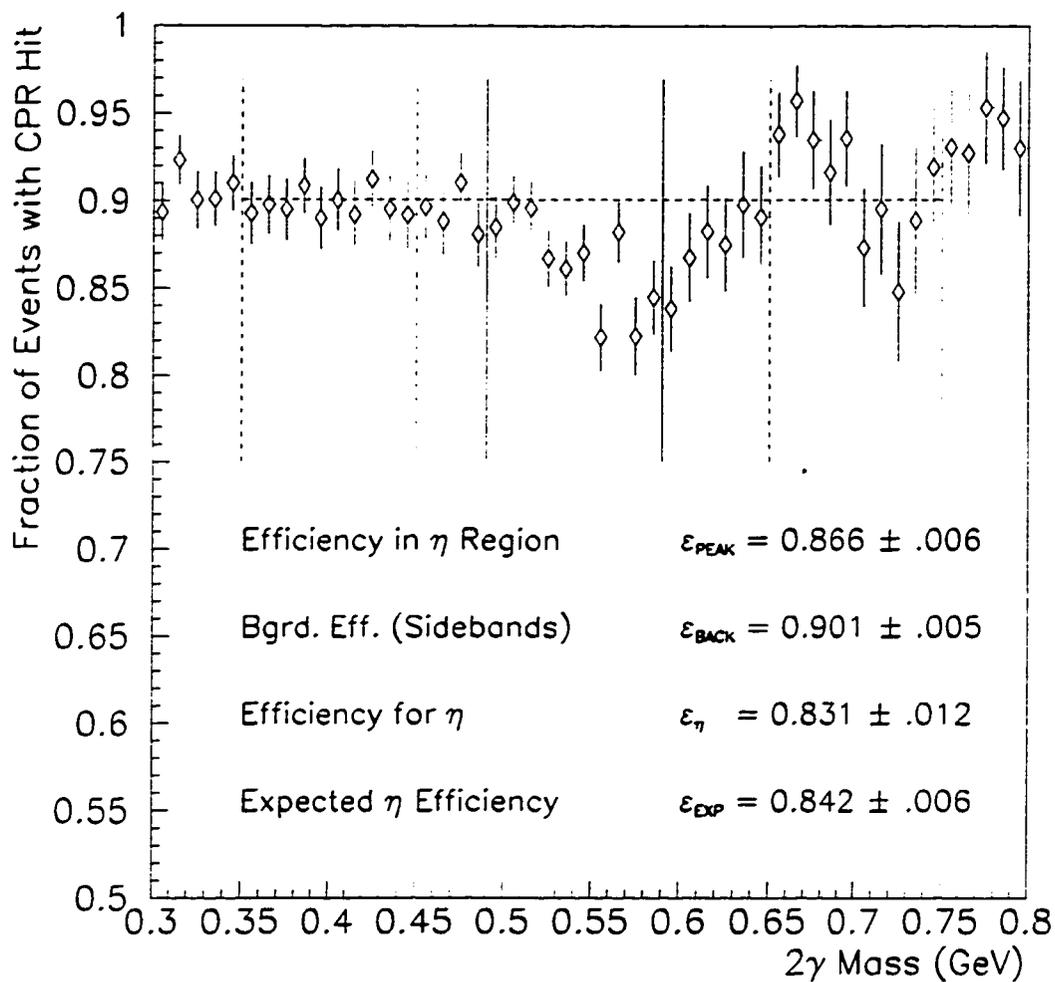
Figure 7.7: The measured CPR hit rate efficiency in the region of the η meson. The signal region is within the solid vertical lines and the sideband regions are within the vertical dashed lines. The horizontal dashed line is the mean efficiency for background.

91

Figure 7.8: The measured CPR hit rate efficiency in the region of the $\rho^{\pm}$ meson. The signal region is within the solid vertical lines and the sideband regions are within the vertical dashed lines. The horizontal dashed line is the mean efficiency for background.

92

Meson	Measured	Expected	Difference
π^0	0.842 ± 0.008	0.847 ± 0.006	-0.005
η	0.831 ± 0.012	0.842 ± 0.006	-0.011
$\rho^\pm$	0.836 ± 0.010	0.834 ± 0.004	$+0.002$

Table 7.2: Comparison of the measured and expected hit rate efficiencies for neutral mesons.

7.2 Systematic Uncertainties in the Profile Method

The systematic uncertainties in the profile method are much larger compared to those in the conversion method. In the low P_T region, photons from a π^0 are quite well separated and therefore the systematic errors are relatively small, but at high P_T, the systematic errors in the profile method rise up to 70%. This is the reason why we use the profile method only for the first bin of P_T (10-16 GeV/c), although the two methods agree with each other to within 5% in the 16-30 GeV/c range.

There are three main sources of systematic uncertainty in the profile method: *shower fluctuations*, *shower shape*, and *gas saturation in the CES* [31]. Like in the conversion method, these uncertainties in the background are completely correlated to the corresponding photon uncertainties. The systematic errors in the profile method are evaluated by varying the source of uncertainty in the QFL simulation [32] and propagating this variation to the direct photon cross section. Below we discuss each

uncertainty in succession.

The shower maximum occurs deeper in the CEM for the photon induced showers than for electron induced showers. Therefore, the number of shower electrons passing through the CES in photon induced shower is less than that for electrons. The simulation accounts for this by increasing the position of the shower maximum by $\Delta T = 0.6$ radiation lengths in the test beam electron parameterization. $\Delta T = 0.6$ is in reasonable agreement with a GEANT simulation, but the Particle Data Group [30] estimates $\Delta T = 1.0$. The difference between the photon chisquared efficiency for $\Delta T = 0.6$ and $\Delta T = 1.0$ gives the absolute change in efficiency shown in 7.9 (a), which we use as a conservative systematic bound.

The profile method is sensitive to the the shape of the profile being fit. Any difference between photon and electron profiles and uncertainties in the amount of material in front of the CES will change the efficiencies. To estimate the sensitivity to variations in the standard profile shape, test beam electron showers were measured with different amounts of material in front of the CES. It was found that, as the amount of material increases the shape changes and the fit worsens, reducing the χ^2 efficiency linearly. The same linear relation, but with opposite sign, was determined for decreasing the amount of material. The difference in the efficiencies between the two measurement points, which were 0.55 radiation lengths apart, was used as a conservative systematic bound. The absolute difference between these two efficiencies, along with statistical errors, is shown in Fig 7.9 (b).

The CES χ^2 is sensitive to the normalized profile, which changes if the central channel pulse height is reduced because of saturation of the signal at large values of gas gain. Such saturation was measured in the test beam data [23] . The test beam data used in the simulation had little or no saturation because they were acquired at

94
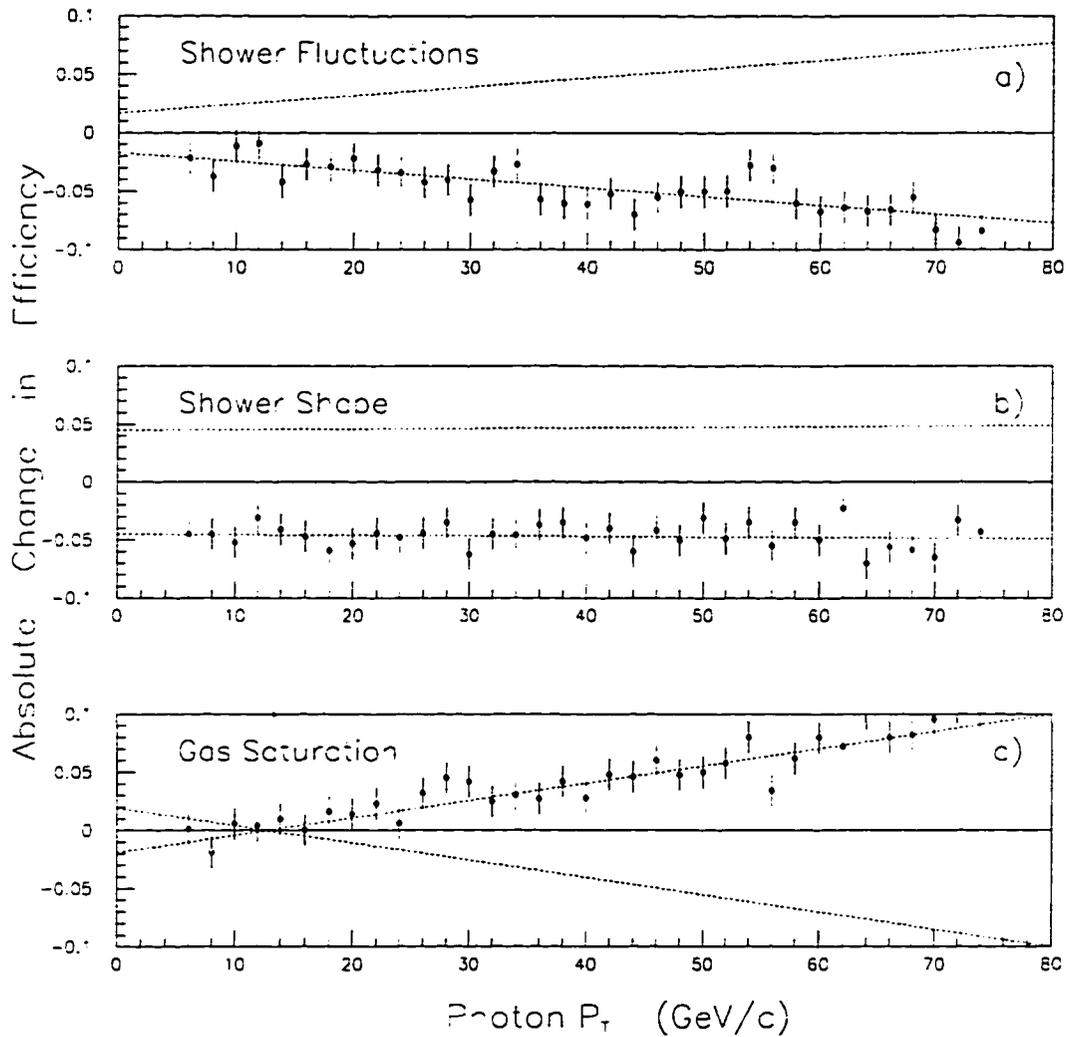
Figure 7.9: The systematic uncertainty for the profile method is shown vs. P_T for 3 sources of systematic uncertainty: a) The amount of statistical fluctuations in the photon shower, b) The transverse shape of the photon shower, c) the affect of CES gas saturation.

95

a relatively low high-voltage (1390 Volts). The effect of the saturation is installed in the QFL detector simulation as a correction, and the correction is estimated for the nominal voltage in B0 (1450 Volts). The correction K is measured by comparing the 80% efficiency cut-point of the χ^2 distribution for test beam data acquired at 1470 Volts to that at 1390 Volts, for 10 GeV and 50 GeV electrons. For 50 GeV electrons

$$K_1 = 1.12 \pm 0.03 \tag{7.6}$$

For arbitrary energy, the correction is extrapolated linearly with energy, assuming that there is no correction at 10 GeV:

$$K = 1 + (K_1 - 1)\frac{E - 10GeV}{50GeV - 10GeV} \tag{7.7}$$

The absolute difference between the photon efficiency with and without correction is shown in Fig 7.9 (c). The errors in the points are statistical. Since this procedure is rather qualitative, we take as systematic uncertainty the value of the correction.

Fig. 7.9 shows that the systematic uncertainties for shower fluctuations and gas saturation rise sharply with energy, but at low P_T they are not so large and the total systematic uncertainty in the 10-16 GeV/c bin is 16%.

7.3 Other Systematic Uncertainties

In this section we give a short overview of other systematic uncertainties in the direct photon cross section measurement.

As we mentioned in chapter 5, the background efficiency depends on the ratios of the particles it contains. The uncertainty in the knowledge of the background composition is a source of systematic error. The dominant error is the knowledge of the production ratio of η to π^0 mesons. The η/π^0 ratio was measured by selecting

96

events in which the η or π^0 decay into two photons [24] and correcting for the relative acceptance using a Monte-Carlo simulation. The uncertainty in the η/π^0 ratio was found to be 25% and leads to a cross section uncertainty of 2% at 16 GeV/c and 0.2% at 100 GeV/c.

The composition of background sources was checked in a sample of events with the same photon cuts as the data but with the isolation cut slightly relaxed. This check showed agreement with the expected value within the uncertainty in ϵ_b quoted above.

For the backscattered photon and electron we use only half of the correction (chapter 5) as systematic uncertainty. This gives a systematic error in the cross section of 2% at 16 GeV/c and 7% at 100 GeV/c.

The uncertainty in the P_T scale is less than 1%, the same as that in the W boson mass measurement [33]. When this is convoluted with the falling spectrum, it results in a cross section uncertainty of 4.5%.

Finally, there are additional uncertainties due to luminosity (3.6%) and to selection efficiencies (4.8%). The full set of systematic uncertainties for the direct photon cross section is given in the Table 7.3.

7.4 Total Systematic Uncertainty

The total systematic uncertainty as a function of P_T along with statistical errors is presented in Table 7.4.

Due to sixfold increased luminosity, detector and trigger upgrades and usage of the conversion method, the uncertainties of the present measurement are significantly smaller compared to the uncertainties of our previous measurement [4]. Ta-

Source of uncertainty	Syst. error at low P_T	Syst. error at high P_T
Conversion Method	7%	2%
Profile Method	30%	-
Backscattering	2%	7%
η/π	2%	0.2%
Luminosity	3.6%	3.6%
Energy Scale	4.5%	4.5%
Cut and Trigger Efficiency	4.8%	4.8%

Table 7.3: Uncertainties of direct photon cross section measurement vs. P_T.

P_T Bin (GeV)	10-16	16-18	18-20	20-22	22-24	24-26	26-28	28-30
Statistical Err. (%)	9.3	2.9	2.6	3.3	3.8	4.3	4.9	6.1
Systematic Err. (%)	16	10	10	10	10	10	9	9

98

P_T Bin (GeV)	30-32	32-36	36-40	40-44	44-55	55-72	72-92	92-152
Statistical Err. (%)	7.2	6.0	7.9	9.5	10.0	10.2	17.4	25.2
Systematic Err. (%)	9	9	9	9	9	10	10	11

Table 7.4: Uncertainties of direct photon cross section measurement vs. P_T.

ble 7.5 compares the statistical and systematic uncertainties of our measurement with those of other direct photon cross section measurements.

	CDF	UA2	UA1	D0 (prel.)	E706
Statistical Error	2.6 %	6%	9%	15%	16-54%
Systematic Error	10 %	21%	29%	50%	16-26%

Table 7.5: Comparison of our uncertainties with those on other experiments.

99

Chapter 8

Discussion of the Results

8.1 Comparison with the QCD Predictions

The cross section measurement can now be compared with QCD calculations to see how well the data and the underlying theory constrain parton distributions, particularly the gluon distribution. As we mentioned before (chapter 6), the results of the measurement agree qualitatively with NLO QCD predictions over many orders of magnitude, but the data have a steeper slope at low P_T (Fig. 6.3).

The visual comparison between data and theory is aided by plotting the ratio (data-theory)/theory on a linear scale. As a default theory we use NLO QCD calculations [10] with the CTEQ2M [9] set of parton distributions. The theoretical calculations also include the isolation cut as well as corrections for the *bremsstrahlung* process [34]. The first set of comparisons is displayed in Fig. 8.1 for the CTEQ2M structure function with different renormalization scales. The band at the bottom of the plot shows the systematic uncertainty of the data, which is nearly 100% point to point correlated. Fig. 8.2 compares the data with theory using different parton

100
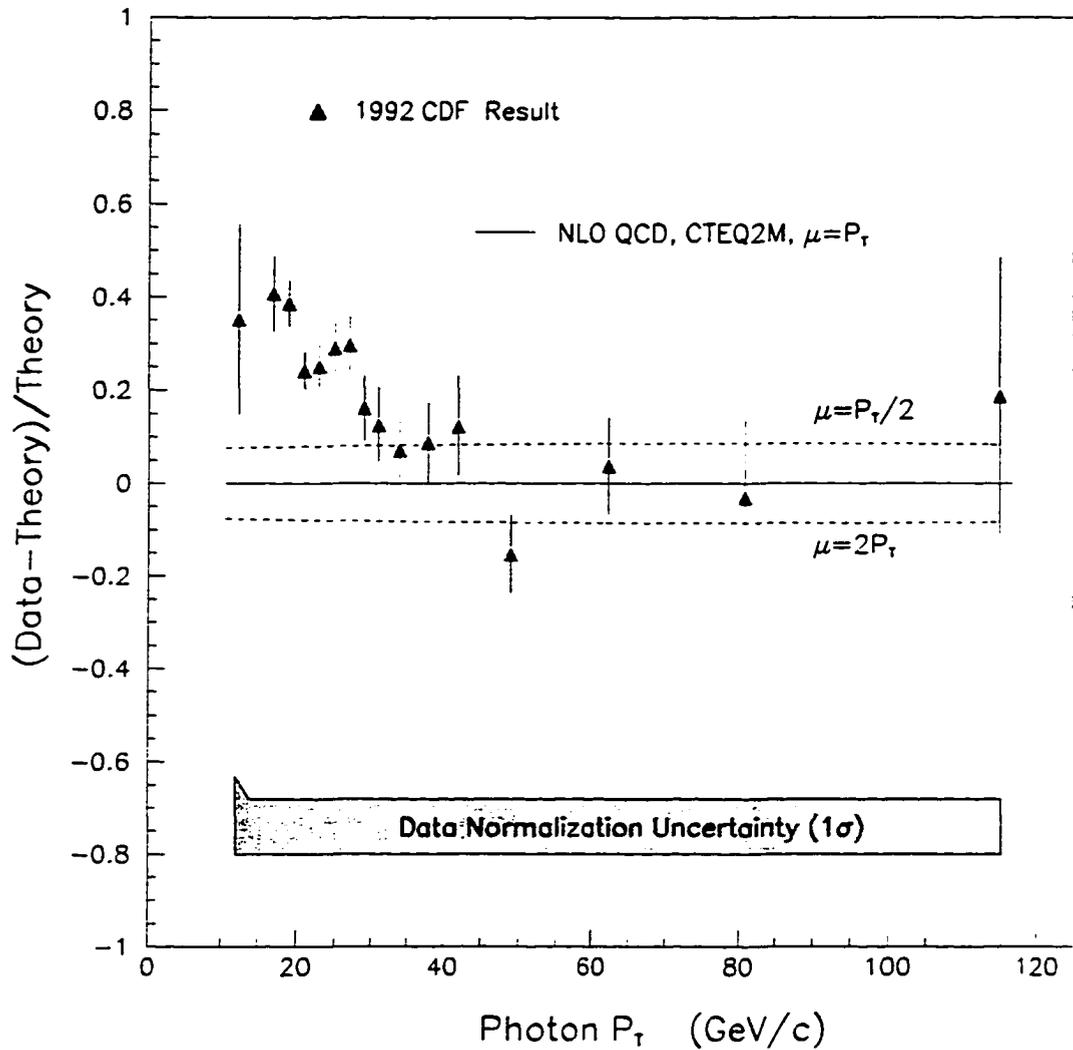
Figure 8.1: The prompt photon cross section measurement is compared with NLO QCD predictions using the CTEQ2M structure function and various renormalization scales. Shown at the bottom is the data systematic uncertainty band, which is nearly 100% correlated point-to-point and includes normalization uncertainties.

101

distributions: CTEQ2ML [9], which produces mostly a shift in normalization, and MRSD- [35], which shows little change.

Both plots display a distinct shape difference at low P_T between data and theoretical predictions regardless of what choice of theoretical parameters or parton distributions are used. Since the systematic error band is an overall scale uncertainty, the shape change allowed in the data by systematics is very small. This means that the clear deviation from the NLO QCD predictions below $P_T \approx 20$ GeV is not the result of uncertainties in the measurement.

It is interesting to note that a direct photon measurement by UA2 [36] also shows stronger rise for small x_T than the theoretical cross section. On the other hand, there seems to be good agreement between NLO QCD predictions and the preliminary Tevatron D0 results [37], which however have sizably larger errors than the CDF data. Below we discuss some possible physical interpretations of the small x_T discrepancy and analyse the uncertainties in the theoretical predictions.

8.2 Extraction of a New Gluon Structure Function

One obvious way to bring the theoretical predictions to agreement with the data is to change the gluon structure function of the proton without any additional theoretical corrections. The explanation for the disagreement would then be that for the first time we are measuring the gluon distribution inside the proton in a fractional momentum range where it has not been measured well previously. In order to check that possibility, we extracted new gluon structure functions using our data. Figure 8.3 shows how our experimental results agree with the NLO QCD predictions evaluated

102
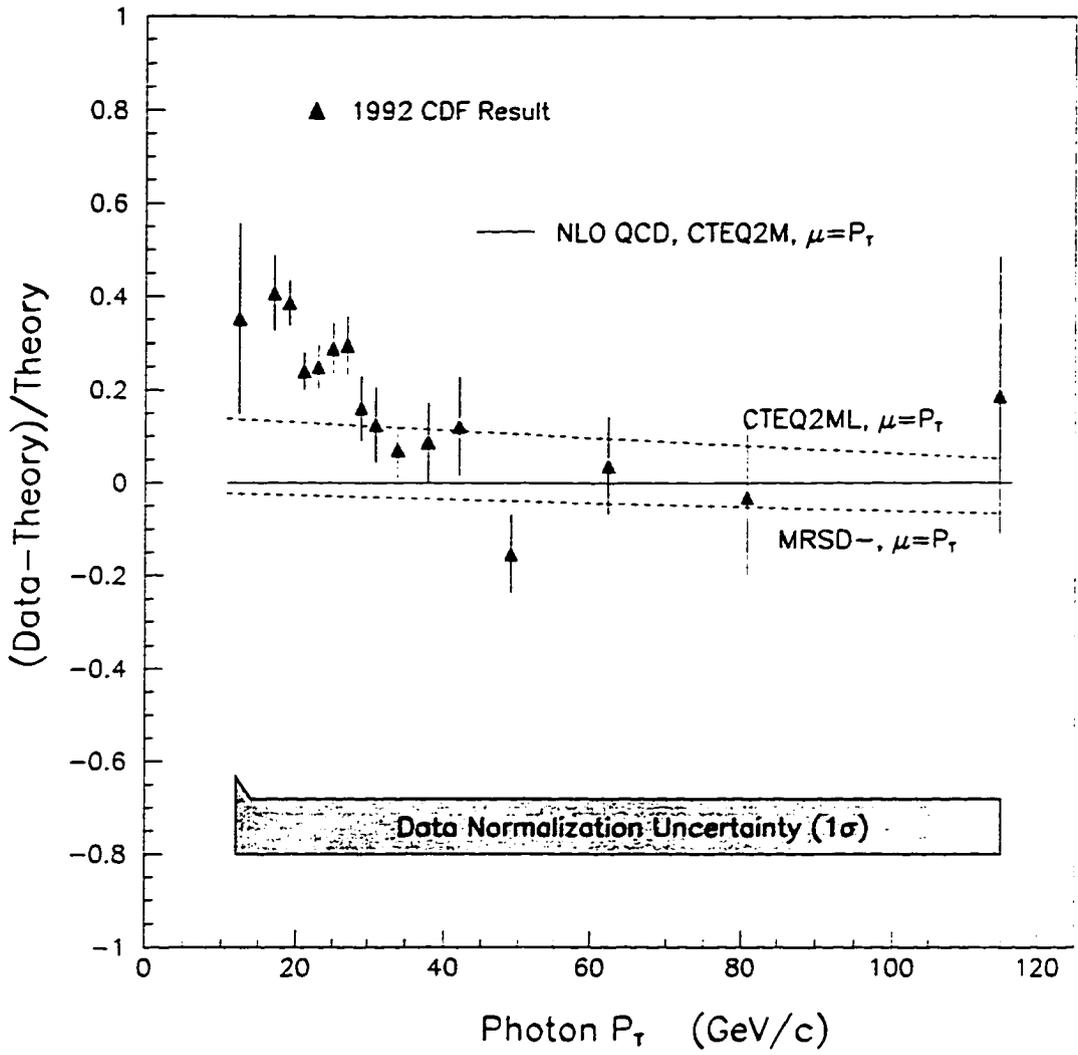
Figure 8.2: The prompt photon cross section measurement is compared with NLO QCD predictions for various parton distributions.

103

with the standard CTEQ and one of the extracted gluon structure functions, which is designated by the abbreviation "fc54". Figure 8.4 shows both structure functions vs gluon x. The new gluon structure function dominates at x below 0.1, but for $x > 0.1$, the region of fixed target experiments, CTEQ has higher gluon density.

To check how well the gluon distributions are explaining experimental results, a global fit of NLO QCD predictions evaluated with CTEQ and fc54 was made to a set of current experimental data. This data set includes various collider as well as fixed target experimental measurements of processes which involve the gluon structure function. Table 8.1 compares the results of this fit for the CTEQ and the fc54 gluon structure functions. CTEQ has smaller χ^2 due to better agreement with the data for $x > 0.1$, while fc54 fits better experimental results for $x < 0.1$ but does not perform well for fixed target data. As a result, the χ^2 of the global fit with fc54 is higher.

Gluon Structure Functions	Total χ^2	Number of Points
CTEQ	777	872
fc54	828	888

Table 8.1: Fit χ^2 of CTEQ and fc54 gluon distributions applied to a set of current experimental data.

This problem can be avoided by adding a third parameter to the gluon structure function (for comparison, quark structure functions usually have five free

104
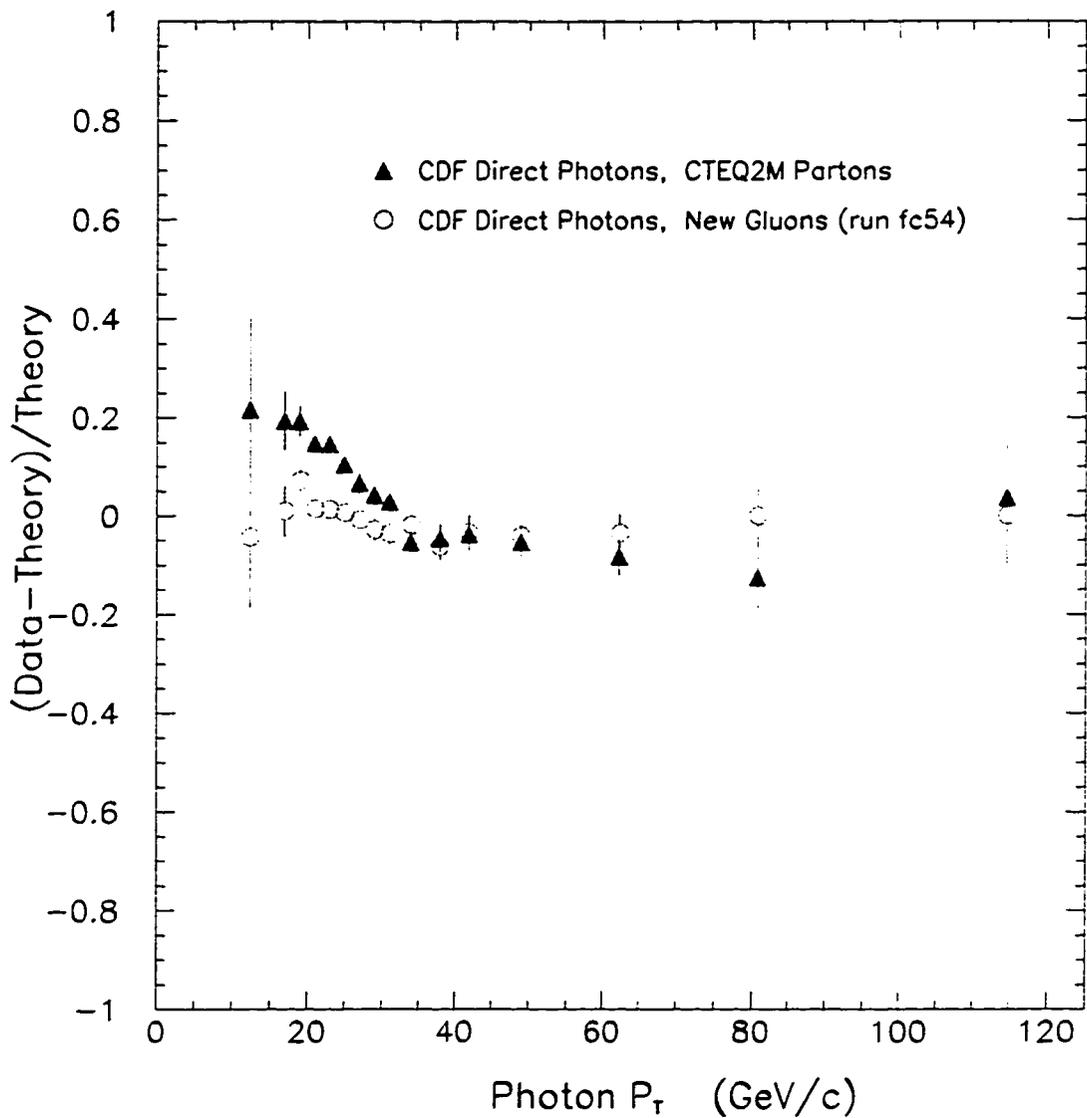
Figure 8.3: The 1992 inclusive photon cross section compared with the NLO QCD prediction using two different gluon distribution functions: the standard CTEQ2M distribution function and the new fc54.

105
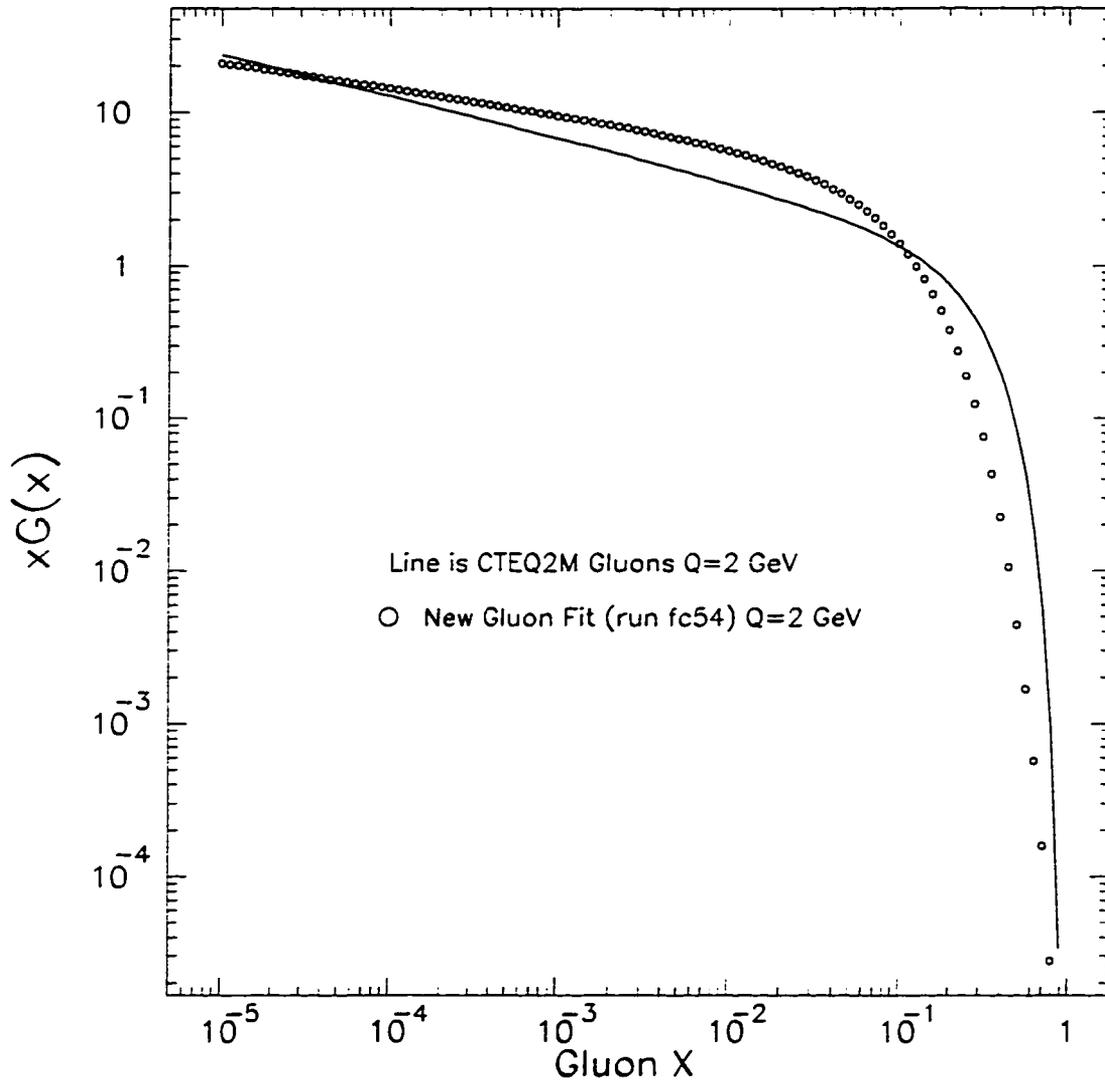
Figure 8.4: Two gluon distribution functions: standard CTEQ and the new fc54.

106

parameters). However, low - P_T inclusive jet cross section measurements at CDF [38] agree well with NLO QCD predictions with a standard gluon structure function[1]. Therefore, we conclude that the main source of the disagreement is not due to the gluon structure function.

8.3 Additional Theoretical Corrections

One possible candidate for the difference between data and the QCD calculation can be the *bremsstrahlung* process, when the photon is emitted quasi collinearly by a parton. Although such a term appears only when calculating the higher order diagrams, it becomes prevalent for low P_T. As we mentioned in chapter 2, for photons with pseudorapidity $\eta = 0$ and $P_T = 15$ GeV/c, the bremsstrahlung contributes as much as (60-70)% to the total cross section. The isolation cut reduces appreciably the bremsstrahlung contribution, but the latter may nevertheless remain significant at small x. However, the measurements of the bremsstrahlung process at LEP [39] show good agreement with NLO QCD predictions, and thus the hypothesis that the disagreement between data and theory may be caused by the bremsstrahlung process seems unlikely. Recently, new additional calculations for the bremsstrahlung process were performed for diagrams which are suppressed for e^+e^- photoproduction at LEP but might contribute to the $p\bar{p}$ photoproduction at the Tevatron [40]. Figure 8.5 compares the fit to the data with the NLO QCD predictions with (triangles) and without (circles) the new bremsstrahlung corrections. This plot shows that the contribution of these corrections is not substantial.

Another process which is necessary to take into the account in direct pho-

---

[1]It is necessary to mention, however, that NLO QCD predictions for inclusive jet production at CDF do not include k_T smearing corrections.

107
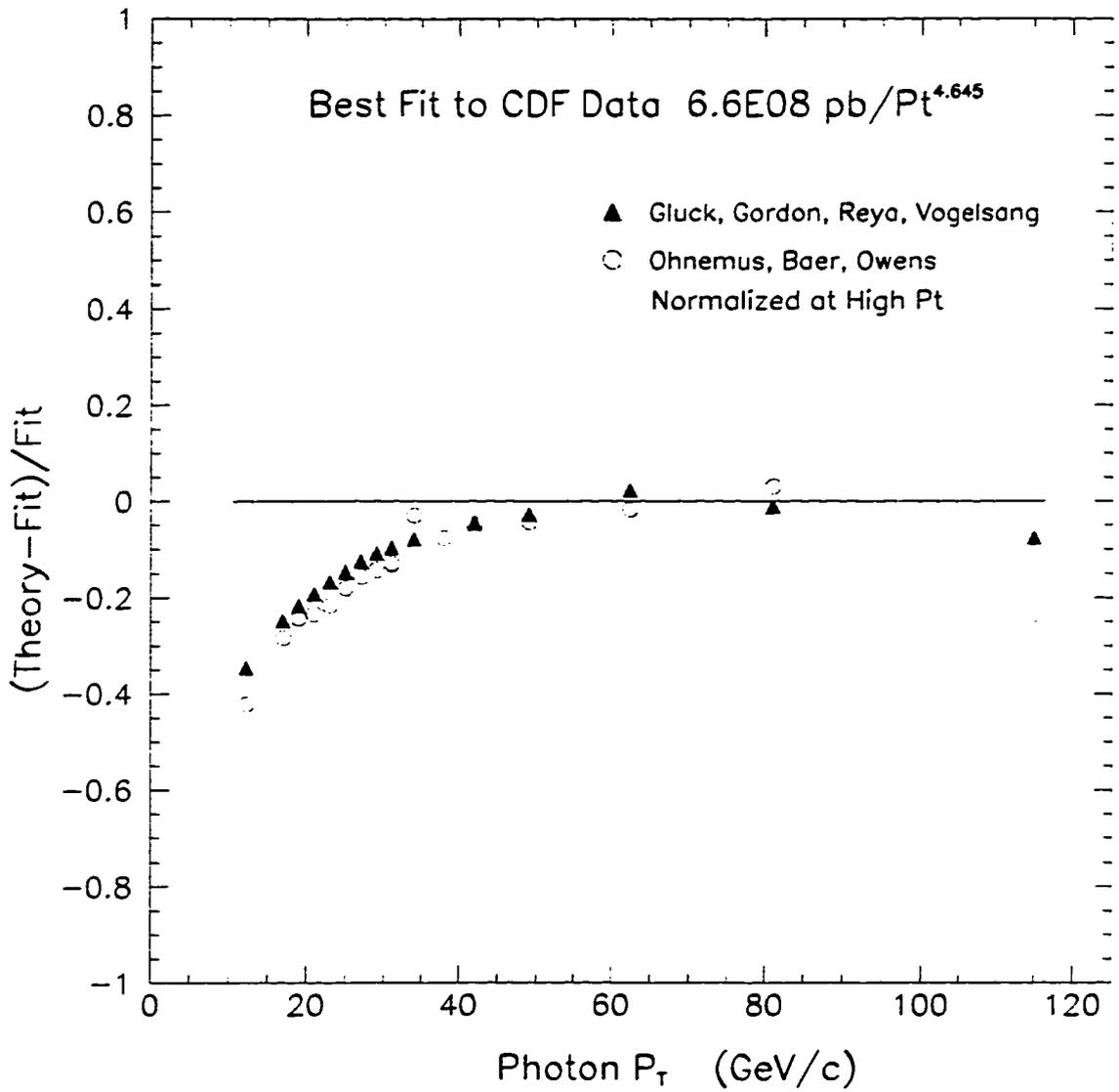
Figure 8.5: Comparison of data fit with NLO QCD predictions with (triangles) and without (circles) additional bremsstrahlung corrections.

108

toproduction is the charm induced contributions coming from $cg \rightarrow \gamma c$. This process is negligible for fixed target experiments but cannot be ignored in the case of collider photoproduction. However, neither the calculations which employ the massless charm quark distribution nor the LO heavy charm photoproduction can eliminate the disagreement.

We also performed calculations for hard diffractive photon production based on the renormalized diffractive model [41]. This process, which is not included in the NLO QCD calculations, contributes a few percent in low-P_T cross section and does not significantly alter the results.

Another source of uncertainty which exists in the theoretical calculations is the k_T *smearing*, based on the idea that the colliding partons have some initial transverse momentum k_T with respect to the incoming hadrons. Since the invariant cross section falls at the rate of an order of magnitude per few GeV of P_T in the low P_T region, it would not take a large amount of smearing to have a significant effect. The main problem in this approach is that the amount of $< k_T >$ is model-dependent and strongly affected by the amount of QCD dynamics included in the calculation. The estimated value of $< k_T >$ varies between 300 MeV from the parton model and uncertainty principle to 860 MeV from LO QCD calculations for the process $q\bar{q} \rightarrow l^+l^-$, and is reduced to 600 MeV for the same process using NLO QCD calculations. The $< k_T >$ smearing value can also be estimated by examining the P_T imbalance of diphoton states. Fixed target experiments, which are extremely sensitive to the amount of smearing due to their rapidly falling P_T spectra, find that $< k_T >$ is slightly greater than 1 GeV (E706 [42]) or slightly smaller than 1 GeV (WA70 [43]). The wide range of the $< k_T >$ values for different processes and energies shows that the smearing effect involves more dynamics than the naive Fermi motion of the

109

partons confined in the proton. More likely, the main source of the smearing is the multiple gluon emission which contains both perturbative and non-perturbative parts. Smearing due to multiple gluon emission can be simulated by the QCD Monte Carlo simulation program PYTHIA [44]. It was found [45] that the NLO QCD predictions for diphotons have to be smeared with $< k_T >= 3$ GeV to reproduce the PYTHIA results. This is the amount of $< k_T >$ which brings the QCD predictions in agreement with CDF and UA2 single photon results. Even more interesting, simulation of direct photon production by PYTHIA shows that the ratio of the cross sections with the initial state gluon radiation switch turned on/off looks very similar to the ratios of data/theory for the CDF direct photon cross section.

8.4 Conclusions

Several conclusions may be drawn from these comparisons.

- The data are in general agreement with the QCD predictions over a wide range in P_T. However, the observed slope at low P_T is not reproduced by the theory, no matter what choice of theoretical parameters or parton distributions are used.

- A new gluon structure function extracted from our data explains better the experimental results in the range $0.01 < x < 0.1$. However, there is substantial disagreement with fixed target experimental results in the region $0.1 < x < 1$, where standard gluon structure functions work better; also, the inclusive jet cross section measurement at CDF does not support higher gluon densities at small x.

110

- The recent higher order calculation of the bremsstrahlung process in $p\bar{p}$ collisions indicates a slightly steeper slope at low P_T, but cannot account for the disagreement completely.

- Additional corrections to the inclusive prompt photon cross section due to hard diffractive photoproduction and charm photoproduction are fairly small.

- The NLO QCD predictions have to be modified to include the effect of k_T smearing. Unfortunately, the amount of $< k_T >$ smearing is model dependent and varies from 300 MeV to 3 GeV, which is close to what is needed to bring our results in agreement with NLO QCD. New Monte Carlo simulations of the initial state gluon radiation show that the discrepancy between data and theory is eliminated by applying such corrections.

- We clearly need a better understanding of the soft, non-perturbative physics. Today's experiments are mature enough not only to test Quantum Chromodynamics on the hard-interaction level, but also to provide very important information about the underlying dynamics. The precise photon cross section measurement at CDF is a good example of this statement. It probes the gluon structure function of the proton and at the same time gives us the possibility to learn more about the underlying non-perturbative physics.

Bibliography

[1] D. Gross and F. Wilczek, Phys. Rev. Lett. **30**, 1343 (1973);

Phys. Rev. D **8**, 3633 (1973).

[2] J. Collins *et al.*, Annu. Rev. Nucl. Part. Sci. **37**,383 (1987).

[3] F. Abe *et al.*, Phys. Rev. Lett. **73**, 2662 (1994);

A. Maghakian *et al.*, CDF/ANAL/JET/CDFR/1963, (1993).

[4] F. Abe *et al.*, Phys. Rev. D **48**, 2998 (1993);

F. Abe *et al.*, Phys. Rev. Lett. **68**, 2734 (1992).

[5] R. Feynman, Photon-Hadron Interactions, (Benjamin, Inc., Massachusetts,1972).

[6] H. Fritzsch, M. Gell-Mann, and H. Leutwyler, Phys. Lett. B **47**, 365 (1973).

[7] H. Politzer, Phys. Rev. Lett. **30**, 1346 (1973).

[8] G. Altarelli and G. Parisi, Nucl. Phys. **B126**, 298 (1977).

[9] J. Botts *et al.*, Phys. Lett. B **304**, 159 (1993).

[10] J. Ohnemus, H. Baer, and J.F. Owens, Phys. Rev. D **42**, 61 (1990).

[11] T. Appelquist and J. Carazzone, Phys. Rev. D **11**, 2856 (1975).

[12] F. Abe *et al.*, Nucl. Instrum. Methods A **271**, 387 (1988).

[13] D. Amidei *et al.*, Nucl. Instrum. Methods A **269**, 51 (1988).

[14] G. Drake *et al.*, Nucl. Instrum. Methods A **269**, 68 (1988).

[15] E. Barsotti *et al.*, Nucl. Instrum. Methods A **269**, 82 (1988).

[16] L. Balka *et al.*, Nucl. Instrum. Methods A **267**, 272 (1988).

[17] L. Nodulman *et al.*, Nucl. Instrum. Methods A **204**, 351 (1983).

[18] F. Bedeschi *et al.*, Nucl. Instrum. Methods A **268**, 50 (1988).

[19] Sara Eno (private communication).

[20] A. Bhatti and S. Kuhlmann, CDF/ANAL/JET/CDFR/1971, (1993).

[21] H. Jensen, CDF/MEMO/CDF/CDFR/770, (1988).

[22] S. Kuhlmann and A. Maghakian, CDF/ANAL/JET/CDFR/2214, (1993).

[23] R. Harris, R. Blair, and S. Kuhlmann, CDF/ANAL/ELECTRON/CDFR/1432, (1991).

[24] R. Harris, CDF/ANAL/JET/CDFR/1472, (1991).

[25] Y. Tsai, Rev. Mod. Phys. **46**, 815 (1974).

[26] R. Brun *et al.*, GEANT3, CERN DD/EE/84-1.

[27] R. Ford *et al.*, EGS, SLAC-0210.

[28] R. Harris *et al.*, CDF/ANAL/JET/CDFR/2318, (1993).

[29] S. Kuhlmann and A. Maghakian , CDF/ANAL/JET/PUBLIC/2478, (1994).

[30] M. Aguilar-Benitez *et al.*, Phys. Rev. D **50**, 1173 (1994).

[31] R. Harris *et al.*, CDF/ANAL/JET/CDFR/1509, (1991).

[32] R. Harris *et al.*, CDF/ANAL/JET/CDFR/1222, (1991).

[33] F. Abe *et al.*, Phys. Rev. D **43**, 2070 (1991).

[34] E.L. Berger and J. Qiu, Phys. Rev. D **44**, 2002 (1991);

P. Aurenche *et al.*, Nucl. Phys. **B33**, 34 (1993).

[35] A.D. Martin, W.J. Stirling, and R.G. Robert, Phys. Lett. B **306**, 145 (1993).

[36] J. Alitti *et al.*, Phys. Lett. B **263**, 544 (1991).

[37] S. Abachi *et al.*, in *Proceedings of the XVII International Symposium on Lepton-Photon Interaction, Beijing, China, 1995.*

[38] A. Bhatti, CDF/PUB/JET/PUBLIC/3229, (1995).

[39] P.D. Acton *et al.*, Z. Phys. C **54**, 193 (1992);

O. Adriani *et al.*, Phys. Lett. B **292**, 472 (1992);

P. Abreu *et al.*, Z. Phys. C **53**, 555 (1992);

D. Decamp *et al.*, Phys. Lett. B **264**, 476 (1991).

[40] M. Gluck *et al.*, High-p_T Photon Production at pp Colliders DO-TH 94/02, (1994).

[41] K. Goulianos, Phys. Lett. B **358**, 379 (1995).

[42] G. Alverson *et al.*, Phys. Rev. D **48**, 5 (1993).

[43] M. Bonesini *et al.*, Z. Phys. C **38**, 371 (1988).

[44] T. Sjostrand *et al.*, Pythia, CERN-TH.6488/92 (1992).

[45] J. Huston *et al.*, Phys. Rev. D **51**, 6139 (1995).

2017 ProQuest Distribution Agreement

This Agreement is between the author (Author) and ProQuest LLC, through its ProQuest Dissertation Distribution business (formerly ProQuest/UMI). Under this Agreement, Author grants ProQuest certain rights to preserve, archive and distribute the dissertation or thesis (the Work), abstract, and index terms provided by Author to ProQuest.

Section I. License for Inclusion of the Work in ProQuest Publishing Program

Grant of Rights. Author hereby grants to ProQuest the **non-exclusive**, worldwide right to reproduce, distribute, display and transmit the Work (in whole or in part) in such tangible and electronic formats as may be in existence now or developed in the future. Author further grants to ProQuest the right to include the abstract, bibliography and other metadata in the ProQuest Dissertations & Theses database (PQDT) and in ProQuest Dissertation Abstracts International and any successor or related index and/or finding products or services.

ProQuest Publishing Program - Election and Elements. The rights granted above shall be exercised according to the publishing option selected by Author in Section III, Author Options, and subject to the following additional Publishing Program requirements:

- Distribution of the Work. Except as restricted by Author in the publishing option selected, the rights granted by Author automatically include (1) the right to allow sale and distribution of the Work, in whole or in part, by ProQuest and its sales agents and distributors and (2) the right to make the Abstract, bibliographic data and any meta data associated with the Work available to search engines and harvesters.

- Restrictions. ProQuest will use commercially reasonable efforts to restrict the distribution of the Work as provided under the publishing option selected by Author or *as later elected by Author* through direct contact with ProQuest. Such election is subject to Author's Degree Granting Institution Directives. With respect to restrictions requested after submission of the Work, Author acknowledges that ProQuest cannot recall or amend previously distributed versions of the Work.

- Removal of Work from the Program. ProQuest may elect not to distribute the Work if it believes that all necessary rights of third parties have not been secured. Refer to the website http://www.proquest.com/products_umi/dissertations/ for information about copyright and your dissertation or thesis. If Author's degree is rescinded, and/or the degree-granting institution so directs, ProQuest will expunge the Work from its publishing program in accordance with its then current publishing policies.

- Degree Granting Institution Directives. Author is solely responsible for any conflict between policies and directions of Author's degree-granting institution, Author's choice of publishing model, and/or any restriction Author places on the use of the Work. For the avoidance of doubt, ProQuest is not responsible for access to the Work that is provided by Author's degree-granting institution through its library or institutional repository. Author must work directly with Author's degree granting institution to ensure application of any restrictions to access relating to the Work by Author's degree granting institution.

.

Delivery of the Work. Author shall provide to ProQuest the Work and all necessary supporting documents during the online submission process, according to the Instructions accompanying this agreement.

Rights Verification. Author represents and warrants that Author is the copyright holder of the Work and has obtained all necessary rights to permit ProQuest to reproduce and distribute third party materials contained in any part of the Work, including all necessary licenses for any non-public, third party software necessary to access, display, and run or print the Work. Author is solely responsible and will indemnify ProQuest for any third party claims related to the Work as submitted for publication.

Open Access Publishing Plus

> Ξ I want the broadest possible dissemination of my work, and I want to provide free global access to the electronic copy of my work via the internet.
> Ξ I understand that I will not be eligible to receive royalties.

I want major search engines (e.g. Google, Yahoo) to discover my work. Learn more: http://www.proquest.com/en-US/products/dissertations/google.shtml

> ☐ Yes
> Ξ No

Acknowledgment: I have read, understand and agree to this ProQuest Publishing Agreement, including all rights and restrictions included within the publishing option chosen by me as indicated above.

REQUIRED Author's signature___*AMaghakian*_____Date____7.5.2017_____

(Print Name)_____Arthur Maghakian_____

Institution conferring degree _____The Rockefeller University_____

Please check type of manuscript:

___ **M (Master's Thesis)**

Dissertation/Master's Thesis Submission Form
Please print clearly in block letters

___ **D (Dissertation)**

Personal Information

Last Name _____

Middle Name or Initial _____

First Name _____

Country (ies) of Citizenship _____

Degree & Dissertation Information

Title of Dissertation/ Thesis _____

Institution conferring degree _____

Degree awarded (abbreviate; e.g., Ph.D.) _____

College, School, or Division _____

Year degree awarded _____

Department or Program _____

Year manuscript completed _____

Advisor/Committee Chair _____

Committee Member _____

Committee Member _____

| Committee Member | _____ | Committee Member | _____ |
| Committee Member | _____ | Committee Member | _____ |

Language of manuscript _____

Primary Subject Category: Enter the 4-digit code and category name from the Subject Category Guide that most closely describes the area of your research. Code_____ Category_____

You may suggest two additional subject categories that may aid in the discovery of your work in our digital database.

Code_____ Category_____ Code_____ Category_____

Provide up to 6 keywords or short phrases for citation indices, library cataloging, and database searching.

_____ _____ _____

_____ _____ _____

Current Contact Information

Current Email Address _____

Street Address _____

Please provide your postal address if you are interested in receiving royalties on sales of your thesis.

| City | _____ | Province | _____ | Daytime Phone | _____ |
| Country | _____ | Postal Code | _____ | Evening Phone | _____ |

Permanent Contact Information

Permanent Email Address _____

Street Address (line 1) _____

| City | _____ | Province | _____ | Future Phone | _____ |
| Country | _____ | Postal Code | _____ | Alternate Future Phone | _____ |

THIS PAGE MUST ACCOMPANY YOUR MANUSCRIPT AND THE REST OF YOUR SUBMISSION MATERIALS

Subject Categories

The ProQuest Dissertations & Theses (PQDT) database and the ProQuest citation indices are arranged by subject categories. Please select the one category below that best describes your field of research or creative work. You may add one or two additional categories on your submission form that will also be associated with your work as secondary subjects.

Arts, Business, Education, Humanities, and Social Sciences

AREA, ETHNIC, AND GENDER STUDIES

African American studies	0296
African studies	0293
American studies	0323
Asian American studies	0343
Asian studies	0342
Baltic studies	0361
Black studies	0325
Canadian studies	0385
Caribbean studies	0432
Classical studies	0434
East European studies	0437
Ethnic studies	0631
European studies	0440
French Canadian culture	0482
Gender studies	0733

GLBT studies	0492
Hispanic American studies	0737
Holocaust studies	0507
Islamic culture	0512
Judaic studies	0751
Latin American studies	0550
Middle Eastern studies	0555
Native American studies	0740
Near Eastern studies	0559
North African studies	0560
Pacific Rim studies	0561
Regional studies	0604
Scandinavian studies	0613
Slavic studies	0614
South African studies	0654
South Asian studies	0638
Sub Saharan Africa studies	0639
Women's studies	0453

BUSINESS

Accounting	0272
Arts management	0424
Banking	0770
Business	0310
Entrepreneurship	0429
Finance	0508
Management	0454
Marketing	0338
Sports management	0430

COMMUNICATIONS AND INFORMATION SCIENCES

Communication	0459
Information science	0723
Journalism	0391
Library science	0399

Mass communication	0708
Technical communication	0643
Web studies	0646

FINE AND PERFORMING ARTS

Art criticism	0365
Art history	0377
Cinematography	0435
Dance	0378
Design	0389
Film studies	0900
Fine arts	0357
Music	0413
Performing arts	0641
Theater	0465
Theater history	0644

EDUCATION

Adult education	0516
Art education	0273
Bilingual education	0282
Business education	0688
Community college education	0275
Continuing education	0651
Curriculum development	0727
Early childhood education	0518
Education	0515
Education finance	0277
Education policy	0458
Educational administration	0514
Educational evaluation	0443
Educational leadership	0449
Educational psychology	0525
Educational technology	0710
Educational tests & measurements	0288
Elementary education	0524
English as a second language	0441
Foreign language instruction	0444
Gifted education	0445
Health education	0680
Higher education	0745
Higher education administration	0446
History of education	0520
Home economics education	0278
Industrial arts education	0521
Instructional design	0447
Language arts	0279
Mathematics education	0280
Middle school education	0450
Multicultural education	0455
Music education	0522
Pedagogy	0456
Performing arts education	0457
Philosophy of education	0998
Physical education	0523
Reading instruction	0535
Religious education	0527
School counseling	0519
Science education	0714
Secondary education	0533
Social sciences education	0534
Sociology of education	0340
Special education	0529
Teacher education	0530
Vocational education	0747

HUMANITIES

HISTORY

African history	0331
American history	0337
Ancient history	0579
Asian history	0332
Black history	0328
Canadian history	0334
European history	0335
History	0578
History of Oceania	0504
History of science	0585
Latin American history	0336
Medieval history	0581
Middle Eastern history	0333
Military history	0772
Modern history	0582
Russian history	0724
World history	0506

LANGUAGE & LITERATURE

African literature	0316
American literature	0591
Ancient languages	0289
Asian literature	0305
British and Irish literature	0593
Canadian literature	0352
Caribbean literature	0360
Classical literature	0294
Comparative literature	0295
English literature	0593
French Canadian literature	0355
Germanic literature	0311
Icelandic & Scandinavian literature	0362
Language	0679
Latin American literature	0312
Linguistics	0290
Literature	0401
Literature of Oceania	0356
Medieval literature	0297
Middle Eastern literature	0315
Modern language	0291
Modern literature	0298
Rhetoric	0681
Romance literature	0313
Slavic literature	0314

PHILOSOPHY AND RELIGION

Aesthetics	0650
Biblical studies	0321
Canon law	0375
Clerical studies	0319
Comparative religion	0618
Divinity	0376
Epistemology	0393
Ethics	0394
Logic	0395
Metaphysics	0396
Pastoral counseling	0397
Philosophy	0422
Philosophy of Religion	0322
Philosophy of science	0402
Religion	0318
Religious history	0320
Spirituality	0647
Theology	0469

LAW AND LEGAL STUDIES

Alternative dispute resolution	0649
Intellectual property	0513
International law	0616
Law	0398
Patent law	0562

SOCIAL SCIENCES

Archaeology	0324
Area planning and development	0341
Criminology	0627
Cultural anthropology	0326
Demography	0938
Economic history	0509
Economic theory	0511
Economics	0501
Economics, Commerce-Business	0505
Economics, Labor	0510
Folklore	0358
Forensic anthropology	0339
Geography	0366
Individual & family studies	0628
International relations	0601
Labor relations	0629
Military studies	0750
Organization theory	0635
Organizational behavior	0703
Peace studies	0563
Physical anthropology	0327
Political Science	0615
Public administration	0617
Public policy	0630
Recreation and tourism	0814
Social research	0344
Social structure	0700
Social work	0452
Sociolinguistics	0636
Sociology	0626
Transportation planning	0709
Urban planning	0999

INTERDISCIPLINARY

Alternative energy	0363
Biographies	0304
Climate change	0404
Cultural resources management	0436
Energy	0791
Food science	0359
Home economics	0386
Information technology	0489
Multimedia	0558
Museum studies	0730
Sustainability	0640
Textile research	0994
Wood sciences	0746

Behavioral, Natural, and Physical Sciences

AGRICULTURE

Agriculture	0473
Agronomy	0285
Animal diseases	0476
Animal sciences	0475
Fisheries and aquatic sciences	0792
Forestry	0478
Horticulture	0471
Plant pathology	0480
Plant sciences	0479
Range management	0777
Soil sciences	0481
Urban forestry	0281
Wildlife management	0286

ARCHITECTURE

Architecture	0729
Architectural engineering	0462
Landscape architecture	0390

BEHAVIORAL SCIENCES

Animal behavior	0602
Behavioral sciences	0384
Clinical psychology	0622
Cognitive psychology	0633
Counseling psychology	0603
Developmental psychology	0620
Experimental psychology	0623
Occupational psychology	0624
Personality psychology	0625
Physiological psychology	0989
Psychobiology	0349
Psychology	0621
Quantitative psychology and psychometrics	0632
Social psychology	0451

BIOLOGICAL SCIENCES

Biochemistry	0487
Bioinformatics	0715
Biology	0306
Biomechanics	0648
Biophysics	0786
Biostatistics	0308
Cellular biology	0379
Developmental biology	0758
Endocrinology	0409
Entomology	0353
Evolution & development	0412
Genetics	0369
Histology	0414
Limnology	0793
Microbiology	0410
Molecular biology	0307
Morphology	0287
Neurosciences	0317
Parasitology	0718
Physiology	0719
Plant biology	0309
Systematic biology	0423
Virology	0720
Zoology	0472

ECOSYSTEM SCIENCES

Ecology	0329
Macroecology	0420
Paleoecology	0426

ENGINEERING

Aerospace engineering	0538
Artificial intelligence	0800
Automotive engineering	0540
Biomedical engineering	0541
Chemical engineering	0542
Civil engineering	0543
Computer engineering	0464
Computer science	0984
Electrical engineering	0544
Engineering	0537
Geological engineering	0466
Geophysical engineering	0467
Geotechnology	0428
Industrial engineering	0546
Mechanical engineering	0548
Mining engineering	0551
Naval engineering	0468
Nanotechnology	0652
Nuclear engineering	0552
Ocean engineering	0547
Operations research	0796
Packaging	0549
Petroleum engineering	0765
Plastics	0795
Robotics	0771
System science	0790

ENVIRONMENTAL SCIENCES

Conservation biology	0408
Environmental economics	0438
Environmental education	0442
Environmental engineering	0775
Environmental geology	0407
Environmental health	0470
Environmental justice	0619
Environmental law	0439
Environmental management	0474
Environmental philosophy	0392
Environmental science	0768
Environmental studies	0477
Land use planning	0536
Natural resource management	0528
Water resources management	0595
Wildlife conservation	0284

MATHEMATICAL AND PHYSICAL SCIENCES

Acoustics	0986
Analytical chemistry	0486
Applied mathematics	0364
Astronomy	0606

GEOSCIENCES

Aeronomy	0367
Atmospheric chemistry	0371
Atmospheric sciences	0725
Biogeochemistry	0425
Biological oceanography	0416
Chemical oceanography	0403
Continental dynamics	0406
Geobiology	0483
Geochemistry	0996
Geographic information science and geodesy	0370
Geology	0372
Geomorphology	0484
Geophysics	0373
Hydrologic sciences	0388
Marine geology	0556
Meteorology	0557
Mineralogy	0411
Paleoclimate science	0653
Paleontology	0418
Petroleum geology	0583
Petrology	0584
Physical geography	0368
Physical oceanography	0415
Planetology	0590
Plate tectonics	0592
Remote sensing	0799
Sedimentary geology	0594

HEALTH AND MEDICAL SCIENCES

Aging	0493
Alternative medicine	0496
Audiology	0300
Dentistry	0567
Epidemiology	0766
Gerontology	0351
Health care management	0769
Health sciences	0566
Immunology	0982
Kinesiology	0575
Medical ethics	0497
Medical imaging and radiology	0574
Medicine	0564
Mental health	0347
Nursing	0569
Nutrition	0570
Obstetrics and gynecology	0380
Occupational health	0354
Occupational therapy	0498
Oncology	0992
Ophthalmology	0381
Osteopathic medicine	0499
Pathology	0571
Pharmaceutical sciences	0572
Pharmacology	0419
Physical therapy	0382
Public health	0573
Public health occupations education	0500
Speech therapy	0460
Surgery	0576
Toxicology	0383
Veterinary medicine	0778

Astrophysics   0596
Atomic physics   0748
Chemistry   0485
Condensed matter physics   0611
Electromagnetics   0607
High temperature physics   0597
Inorganic chemistry   0488
Low temperature physics   0598
Materials science   0794
Mathematics   0405
Mechanics   0346
Molecular chemistry   0431
Molecular physics   0609
Nanoscience   0565
Nuclear chemistry   0738
Nuclear physics   0756
Optics   0752
Organic chemistry   0490
Particle physics   0798
Physical chemistry   0494
Physics   0605
Plasma physics   0759
Polymer chemistry   0495
Quantum physics   0599
Statistics   0463
Theoretical mathematics   0642
Theoretical physics   0753